Fall 2014

Crossflow Transition At Mach 6 On A Cone At Low Angles Of Attack

Ryan O. Henderson
Purdue University

Recommended Citation

Henderson, Ryan O., "Crossflow Transition At Mach 6 On A Cone At Low Angles Of Attack" (2014). *Open Access Theses*. 334.
https://docs.lib.purdue.edu/open_access_theses/334

Graduate School Form 30
(Revised 08/14)

PURDUE UNIVERSITY
GRADUATE SCHOOL
Thesis/Dissertation Acceptance

This is to certify that the thesis/dissertation prepared

By Ryan O. Henderson

Entitled
CROSSFLOW TRANSITION AT MACH 6 ON A CONE AT LOW ANGLES OF ATTACK

For the degree of Master of Science in Aeronautics and Astronautics

Is approved by the final examining committee:

Steven P. Schneider

John P. Sullivan

Patrick E. Rodi

To the best of my knowledge and as understood by the student in the Thesis/Dissertation Agreement, Publication Delay, and Certification/Disclaimer (Graduate School Form 32), this thesis/dissertation adheres to the provisions of Purdue University's "Policy on Integrity in Research" and the use of copyrighted material.

Approved by Major Professor(s): Steven P. Schneider

Approved by: Wayne Chen 09/30/2014

Head of the Department Graduate Program Date

CROSSFLOW TRANSITION AT MACH 6 ON A CONE AT LOW ANGLES OF ATTACK

A Thesis
Submitted to the Faculty
of
Purdue University
by
Ryan O. Henderson

In Partial Fulfillment of the
Requirements for the Degree
of
Master of Science in Aeronautics and Astronautics

December 2014
Purdue University
West Lafayette, Indiana

ACKNOWLEDGMENTS

First and foremost, I would like to thank my advisor, Professor Steven Schneider, for his guidance throughout this research as well as giving me the opportunity to investigate the unknown. I would also like to acknowledge Dr. John Sullivan and Dr. Patrick Rodi, for joining my advisory board. I would also like to acknowledge Lockheed Martin for funding the research.

I would like to acknowledge Robin Snodgrass, Jim Younts, and Jerry Hahn in the ASL machine shop for keeping the tunnel and the experiments operating smoothly. The machine shop humor was also appreciated. John Phillips was also very helpful with all electronic problems I came across.

Though my lab mates taught me much about fluid mechanics, they moreover provided continuous entertainment throughout my time at Purdue. Thanks to Dennis Berridge, Amanda Chou, Brandon Chynoweth, Roger Greenwood, Greg McKiernan, George Moraru, and Chris Ward for the wonderful memories around the lab. Alumni Matt Borg was very helpful with sharing his knowledge of traveling waves. Also thanks to John Schooner and his friend Sam Ball for brightening everyone's day throughout the semesters.

I would like to specially thank my family for encouragement throughout my graduate career, even though most of them don't know what I do (I work in a tube that blows air). They still believed in me and sent their love whenever I needed it. Most importantly I am indebted to Nicole Quindara for loving and supporting me while suffering through my long hours away and other tunnel nonsense.

TABLE OF CONTENTS

APPENDICES

LIST OF TABLES

LIST OF FIGURES

Figure Page

SYMBOLS

α	angle of attack
Δ	change in value
δ^*	tunnel-wall turbulent boundary-layer displacement thickness
γ	ratio of specific heats
μ	dynamic viscosity
Φ	wave angle
ϕ	azimuthal angle
τ	time delay of signal
θ	half-angle of cone
$\bar{c}$	aerodynamic-noise-transition correlation size parameter
A	disturbance amplitude
A_0	initial disturbance amplitude
C	test-section circumference
c_1	reference test-section circumference
C_r	phase speed
$C_{F_{II}}$	tunnel-wall skin-friction coefficient
C_{xy}	coherence of signals x and y
$E\#R\#$	run schedule index: Entry # Run #
f	frequency
I	intensity of light emitted from paint
k	thermal conductivity of a solid material
L	depth of paint layers
M	Mach number
N	integrate amplification factor
P	pressure

P'	RMS pressure fluctuations
PSD_{xy}	cross power spectral density of signals x and y
q''	heat flux
R	gas constant of air
Re/ft	freestream unit Reynolds number per foot
T	temperature
x	axial distance from nosetip
x'	rotated axial surface axis
y	spanwise surface axis
y'	rotated circumferential surface axis

Subscripts

b	base value
$dark$	reference image with no illumination
max	maximum value
$mean$	theoretical mean
min	minimum value
o	total
off	reference image while wind tunnel has not started
on	image while wind tunnel is started
ref	reference value
t	transition location measured from nosetip
$tanc$	theoretical mean using tangent-cone method
w	condition at the wall

ABBREVIATIONS

AC	Alternating Current
AoA	Angle of Attack
BAM6QT	Boeing/AFOSR Mach-6 Quiet Tunnel
CCD	Charged-Couple Device
DC	Direct Current
FFT	Fast-Fourier Transform
ISSI	Innovative Scientific Solutions Inc.
LED	Light Emitting Diode
LPSE	Linear Parabolized Stability Equations
PSD	Power Spectral Density
RMS	Root-mean-square
SB	Schmidt-Boelter
TSP	Temperature Sensitive Paint

ABSTRACT

Henderson, Ryan O. MSAA, Purdue University, December 2014. Crossflow Transition at Mach 6 on a Cone at Low Angles of Attack. Major Professor: Steven P. Schneider.

Experiments on a sharp 7° cone at low angles of attack were conducted at Mach 6 to understand the stationary and traveling modes of crossflow disturbances, the interaction between them, and the development of other instabilities that can lead to transition. Using the Boeing/AFOSR Mach-6 Quiet Tunnel (BAM6QT), pressure and temperature measurements were collected to better describe crossflow characteristics. Noisy and quiet flow conditions were compared to understand crossflow development.

Temperature Sensitive Paint (TSP) was used to measure the global surface temperatures on the model. Schmidt-Boelter (SB) gauges were used to convert the surface temperatures to heat transfer. The global heat transfer then allowed the stationary crossflow to be visualized and quantified in terms of heat flux. Integrating heat fluxes azimuthally, the amplitudes of the stationary crossflow vortices were compared against the amplitudes of the traveling waves.

PCB 132A31 and Kulite XCQ-062-15A transducers were used to measure pressure fluctuations over a broad range of frequencies. The traveling crossflow instability, the second-mode instability, and possibly the secondary-instability of the stationary crossflow mode were found at certain tunnel conditions. A grouping of Kulites was used to determine traveling wave speed and direction.

Roughness elements were added to the model to excite discrete stationary vortices. The roughness elements provided a method to alter the strength of the stationary vortices. This technique allowed traveling-mode amplitudes to be compared to varying stationary-mode amplitudes.

1. INTRODUCTION

Vehicles designed to operate at hypersonic speeds must consider aerodynamic drag, control authority, heat transfer, and engine performance as major components in aircraft development [1]. Laminar-turbulent boundary-layer transition can greatly affect each of these factors and further stress an already constrained design. As an example, flight data from the reentry-F tests show that boundary-layer transition to a turbulent boundary layer increased the heat transfer by 3 to 8 times above that of the laminar case [2]. Therefore it is imperative to study transition and understand the processes that dominate it.

A hypersonic boundary layer can transition due to a variety of flow instabilities. Disturbances can enter the boundary layer from the freestream through receptivity processes [3]. The disturbances grow downstream via linear instabilities, transient growth, or through bypass mechanisms, depending on the initial amplitudes of the disturbance. Figure 1.1, from Reshotko et al. [4] shows the paths an instability can grow which ultimately leads to turbulence.

Understanding the mechanisms through which disturbances linearly amplify (Path A in Figure 1.1) is a large branch of hypersonic transition research, but a field that still needs much improvement. A hypersonic boundary layer can experience a variety of these disturbances depending on tunnel conditions and body geometry. A simple semi-empirical method for predicting transition from these disturbances is the e^N method. Equation 1.1 shows the formula for the e^N method as

$$e^N = A/A_0 \tag{1.1}$$

where A_0 is the initial amplitude of where an instability begins to amplify, A is the amplitude of an instability at a given location, and N is the natural logarithm of the

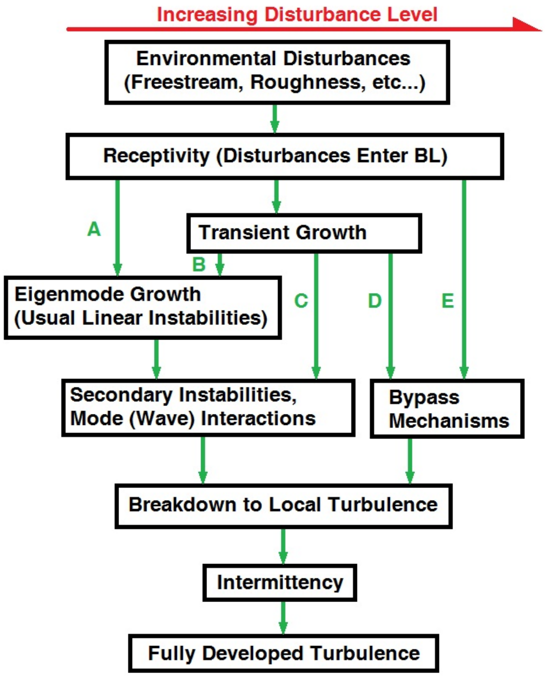

Figure 1.1. Mechanisms of boundary-layer transition. Redrawn from Fig. 1 of Reference [4].

amplitude ratio. This calculated value, N, can then be correlated to when transition occurs [5].

These instabilities include the first and second Mack modes; the Görtler instability; disturbances that develop from attachment lines, entropy layers, roughness, ablation; and crossflow [3]. The crossflow instability was of particular interest for its strong relevance to conical geometries at angle of attack.

To study crossflow and streamwise instabilities, high-speed wind tunnels are used. Most of these wind tunnels develop a turbulent boundary layer along the test-section walls that radiate acoustic waves. These acoustic disturbances, also referred to as tunnel noise, are difficult to remove. The magnitude of tunnel noise increases with the fourth power of the Mach number [6], so facilities that operate in the supersonic and hypersonic regime are sensitive to the noise effect.

Purdue's Boeing/AFOSR Mach-6 Quiet Tunnel (BAM6QT) is a facility built to maintain a laminar boundary layer to reduce noise levels in the test section. The noise levels measured in the BAM6QT are comparable to those seen in flight [7]. For this reason the BAM6QT has a unique ability to study flow instabilities. An example of noise effects can be seen in the shadowgraph image of Shot 6728 from the Naval Ordnance Lab ballistics range in Figure 1.2 [8]. A 5° half-angle cone near zero angle of attack is moving through still air at Mach 4.31 from left to right. Flow on the top surface of the cone has laminar and turbulent regions, as noted. Striations can be seen radiating from the turbulent spots, whereas the laminar sections are free of these disturbances. These striations are radiated from turbulent eddies that cause acoustic noise.

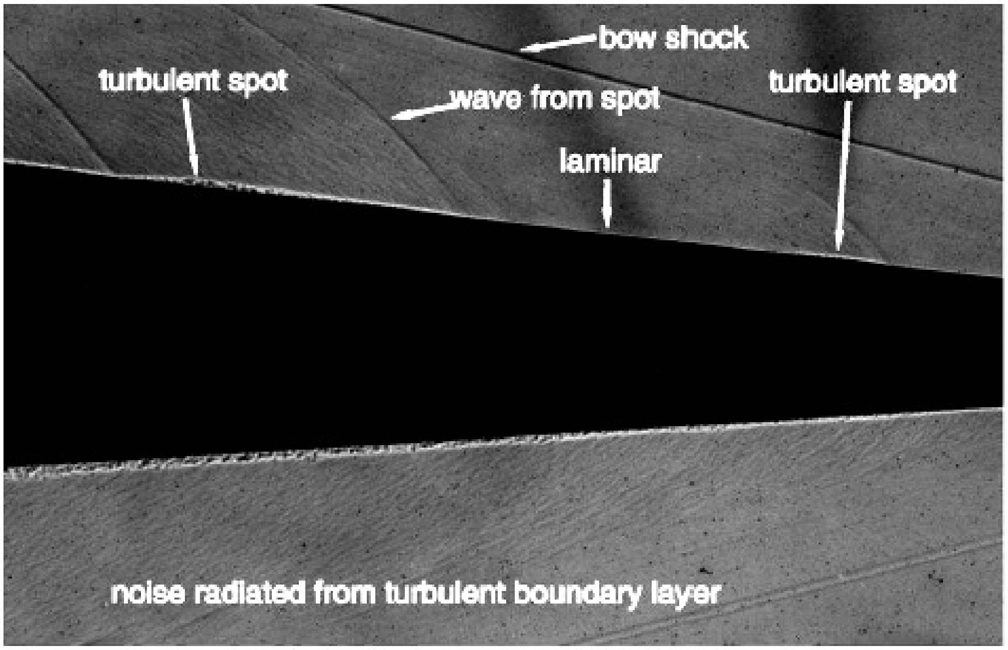

Figure 1.2. Shawdowgraph of noise effects of turbulent spots on a sharp cone at Mach 4.31. Image courtesy of Dan Reda.

This phenomenon occurs on the walls of supersonic and hypersonic wind tunnels. If a turbulent boundary layer develops or turbulent spots appear, unwanted noise and flow disturbances can propagate downstream into the test section and alter the physics of an experiment.

1.1 Objectives

Many experiments study the crossflow instability on a 7° half-angle cone at 6° angle of attack as a standard for comparison among research institutions. The lack of range in angle of attack makes insights from these experiments to a practical design difficult. Therefore the main goal of the research project was to observe flow instabilities over a range of low angles of attack on a 7° half-angle cone at Mach 6. The research was carried out in three phases.

The first was to observe and quantify traveling crossflow instabilities. Various azimuthal rays were measured over a range of Reynolds numbers. Quiet and noisy conditions were also compared. The traveling-wave amplitudes, speeds, and propagation directions were calculated from these tests.

Once the traveling wave characteristics and properties were determined, the second phase of the research was to understand the interaction between the stationary and traveling crossflow instabilities. Roughness elements were introduced to help vary the strength of the stationary crossflow waves. Reynolds effects were then investigated.

The final phase of the project was added during the course of the experiments when high-frequency disturbances were found. A possible secondary instability of the stationary crossflow waves was thought to exist. An investigation was conducted to determine what conditions cause these disturbances.

2. BACKGROUND

2.1 Crossflow Instability

The crossflow instability is characterized by a three-dimensional inflected boundary-layer velocity profile caused by geometry sweep and pressure gradients [9]. At hypersonic speeds, a cone creates a conical shock around the body. At angle of attack, the windward side of the shock will be stronger than the lee side. The difference in shock strength creates a circumferential pressure gradient from the windward to leeward side of the cone. Due to a pressure gradient perpendicular to the flow, low-momentum fluid within the boundary layer is deflected in the transverse direction. The crossflow component and basic boundary-layer profile combination results in an inflected three-dimensional velocity profile. The schematic of a typical crossflow velocity profile is shown in Figure 2.1.

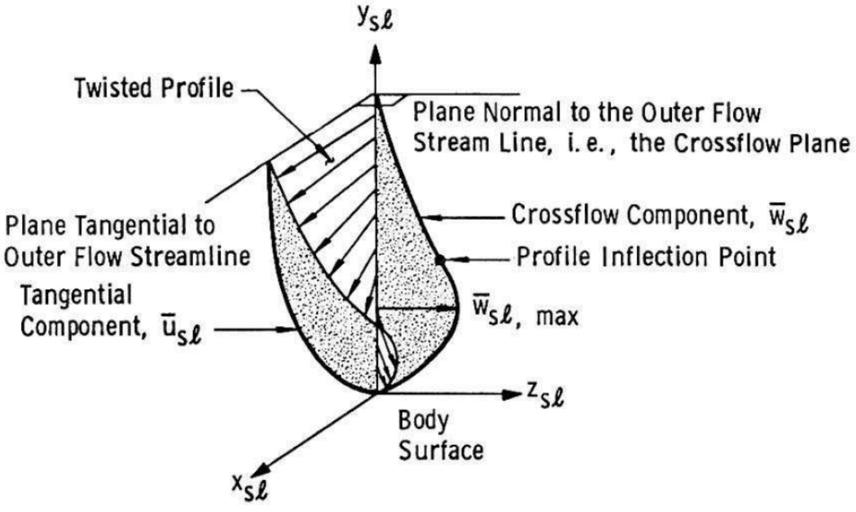

Figure 2.1. Boundary layer, crossflow, and resultant velocity profiles. Image from Adams [10].

The resultant velocity profile is inviscidly unstable and develops into co-rotating vortices around the resultant inflection point. The trajectories of these vortices then follow the inflection point [11]. The vortical path can be illustrated by computations made by Gronvall et al. [12] on a 7° half-angle cone at 6° angle of attack, depicted in Figure 2.2.

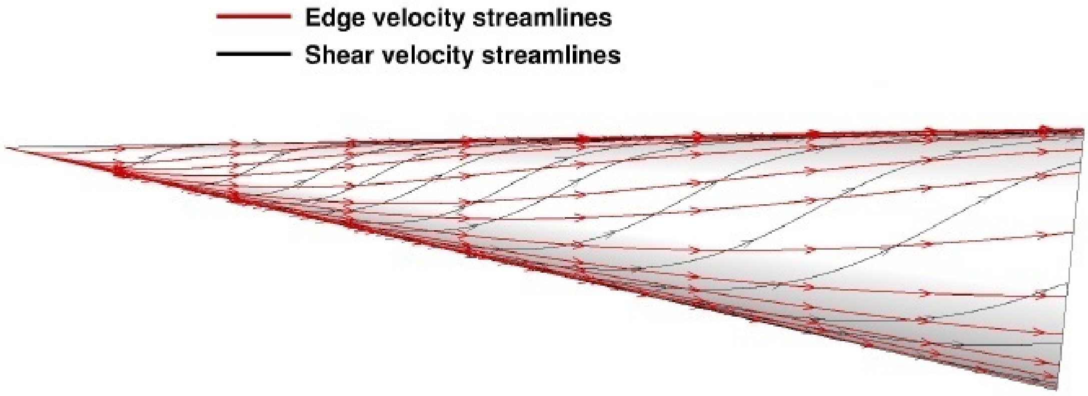

Figure 2.2. Boundary layer streamlines on a 7° half-angle cone at 6° angle of attack. With permission from author [12].

The red contours indicate the edge velocity of the boundary layer and the black contours mark the velocity very near the cone surface. Both streamlines are deflected towards the leeward side as a result of the pressure gradient, but the black streamlines are more responsive due to the lower momentum near the surface.

The primary crossflow instability takes the form of either stationary or traveling waves with respect to the surface. These modes are discussed in the subsequent sections.

2.1.1 Stationary Mode

The stationary mode is fixed relative to the surface and follows the edge velocity streamlines depicted in Figure 2.2. The velocity disturbances from the transverse and normal directions distort the mean flow and stabilize the stationary mode. At low speed on a swept wing, the primary instability then saturates at an amplitude of 10% to 30% of the mean flow [9]. According to Saric and Reed [13], stationary modes are more practical to study at low speeds because they tend to dominate low-disturbance environments, such as flight conditions. At high speeds the crossflow mode that dominates is uncertain.

When stationary crossflow waves are present, the co-rotating vortices are observed through various imaging techniques. At low speeds, the structure of the vortices can be visualized using smoke and oil flow techniques. At high speeds, the high temperature mean flow is imparted onto the surface via the crossflow vortices. The additional heat to the surface is localized where the vortices are present and therefore can be observed by temperature measurement techniques. Infrared thermography and temperature sensitive paints are the primary techniques used to expose the stationary mode. Oil flow visualization is also used at high speeds to complement temperature techniques.

2.1.2 Traveling Mode

The traveling crossflow instability is composed of unsteady vortices oriented at a steeper angle than the stationary counterpart, as computed by Malik et al. [14] on a swept wing at low speeds and experimentally found by Borg et al. [15] on an elliptic cone at Mach 6. At low speeds, linear stability theory suggests the traveling mode has higher growth rates than the stationary mode and if the initial amplitudes are sufficiently large, the traveling waves will become the dominant instability toward transition [9]. Again, the traveling-mode physics at high speeds are not clear, but low-speed knowledge helps guide the understanding of these disturbances.

Due to the transient nature of traveling crossflow, TSP, infrared thermography, and other similar low-frequency measurement techniques cannot be used. Instead, high-frequency pressure sensors were found useful in detecting the traveling crossflow pressure fluctuations, as discussed in References [15, 16].

2.2 Secondary Instability of Crossflow Vortices

As stationary vortices grow along a surface and reach high amplitudes, they become unstable to high-frequency disturbances. These disturbances are labeled as the secondary instability of the stationary mode. Though the secondary instability is not the primary cause of transition, the appearance of the disturbance is followed by rapid destabilization of the boundary layer and then breakdown [9].

Low-speed work classifies the secondary instability into two modes depending on which type of inflectional instability is present. Type-I modes arise from shear layers in the spanwise direction ($\delta U/\delta z$). This gradient rolls the flow up into secondary vortices on the back side of the primary vortex. Type-II modes are driven by a wall-normal gradient ($\delta U/\delta y$). Theory suggests type-II modes are the most unstable, but multiple experiments [17–19] have determined that the highest-amplitude mode is predominantly type-I. Experiments by Swearingen and Blackwater [20] have observed the type-I mode behavior in Görtler vortices as well.

2.3 High-Speed Second-mode Instability

According to inviscid linear stability calculations outlined by Mack [21], unstable acoustic modes develop as disturbances in a flow for a defined spectrum of wavenumber bands and their related phase speeds. These acoustic modes become important to boundary-layer transition above Mach 3 to 4 [22]. The acoustic modes or "Mack modes" are acoustic waves confined between the wall and the relative sonic line in the boundary layer. The acoustic waves reflect between the two boundaries at a supersonic phase velocity relative to the boundary-layer flow. The thickness of the boundary layer determines the frequency at which these waves travel [23]. Figure 2.3 shows the profile of a reflection and the effect that the waves have on the pressure distribution inside the boundary layer.

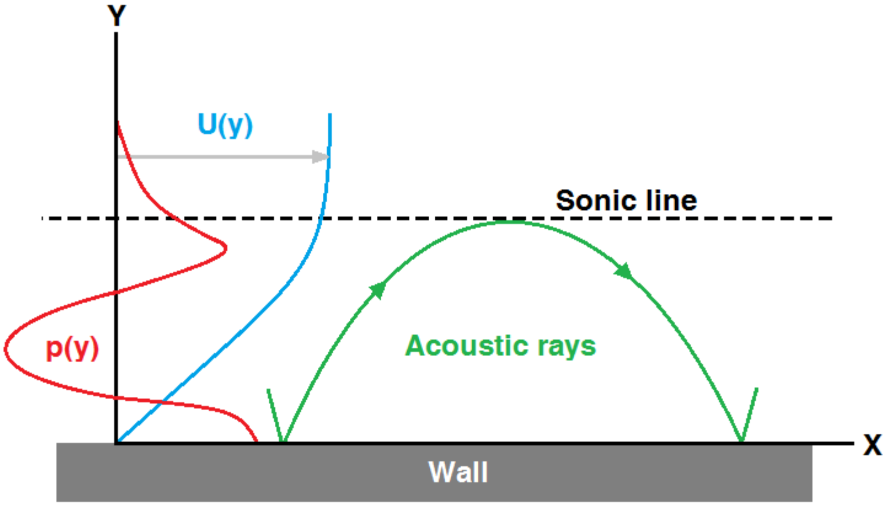

Figure 2.3. Path of acoustic mode and property profiles in the boundary layer, where U(y) is the velocity profile, and p(y) is the pressure disturbance profile. Redrawn from Fig. 2 in reference [24].

2.4 Low-Speed Experiments

In 1935, Adolf Busemann presented the concept of wings with sweep at the fifth Volta conference. Experiments began during World War II and continued to gain importance when jet engines pushed airplanes to higher speeds [25]. As swept wings were tested, researchers noticed earlier transition compared to unswept wings. The first studies conducted to understand this problem began with Gray in 1952 [26]. Gray used sublimation techniques to observe the location of transition. The evaporation methods revealed streaks in the general direction of the flow. Later, the streaks were confirmed as the stationary mode of the crossflow instability from theoretical work by Owen and Randall [27].

In 1985, Poll [28] made the first measurements of the traveling mode. Using hot wires approximately 10 mil from the surface of a yawed cylinder, high-frequency disturbances at 1.1 kHz and 17.5 kHz were detected within the boundary layer. Poll stated these disturbances can exceed 20% of the local mean-flow velocity. The higher frequency disturbances at 17.5 kHz developed from what he thought to be the intermittent turbulence.

Kohama continued Poll's investigation of the traveling mode in 1987. Using smoke visualization and hot-wire anemometry on a swept cylinder, he found evidence of a high-frequency secondary instability [29]. Kohama was able to visualize ring-like vortices spiraling on the edge of the stationary vortices. From his hot-wire data he concluded that the higher frequency fluctuations in Poll's experiment were the secondary instabilities of the stationary crossflow and not a product of intermittent turbulence.

Müller and Bippes [30] investigated the receptivity of crossflow as a continuation of the Nitschke-Kowsky and Bippes [31] experiments. By translating a swept-wing model relative to the flow direction, the streaks were observed to be fixed relative to the model. This led them to conclude that stationary vortices were related to surface roughness and not to features of the freestream flow. Following these experiments, Radeztsky et al. [32] used micrometer-sized roughness elements to influence crossflow-dominated transition. The results showed stationary crossflow amplitudes increase with roughness-element diameter as well as spacing. Transition onset was sensitive to both of these parameters.

An investigation of the interaction between the stationary and traveling crossflow was conducted by Bippes and Lerche [33] in 1997 on a swept flat plate. The stationary mode was excited by roughness similar to Reibert's [34] experiments. The traveling mode was excited by varying the tunnel's turbulence levels between 0.08% and 0.57%. The results of the experiment showed that each crossflow mode altered the mean flow of the boundary layer in a similar way. That is, the shape of the boundary-layer profile has the same inflected profile, but the distortion of the inflections depend on the amplitudes of each type of crossflow. The authors also found that if the initial amplitudes of the traveling modes are increased with respect to the stationary modes, a decrease in the amplitude at which the stationary modes saturate can be seen, and vice versa. Thus the nonlinear development and subsequent breakdown to transition has a strong dependence on the initial amplitude of each crossflow mode.

Computational simulations were incorporated into understanding the secondary instability. Computations on a swept Hiemenz model by Malik et al. [14] helped corroborate the high-frequency instabilities that Poll and Kohama found. They found that the most amplified mode of the secondary instability was the mode-I, or type-I, mechanisms. A later computation by Koch et al. [35] on a swept plate found the same mode to be the most amplified.

More extensive reviews of low-speed crossflow and the experiments pertaining to the phenomenon can be found in Bippes's review [36] and Saric et al. review [37].

2.5 High-Speed Experiments

Though high-speed experiments investigating crossflow-dominated transition are sparse, the last 10-15 years has seen an increase in research interested in understanding the crossflow phenomena in supersonic and hypersonic regimes.

Saric and Reed [13] used discrete roughnesses on a 73° swept wing at Mach 2.4 to investigate passive control of the crossflow instability. The wing was designed to have subsonic flow at the leading edge by sweeping the wing past the Mach angle. This experiment used roughness elements to delay transition over a range of roughness spacing. The authors note that the wavelengths induced by the roughness spacing will work equally well at delaying transition in low-speed flows.

Choudhari et al. [38] used Saric and Reed's experiment as a case study to develop computations for a higher fidelity transition prediction approach. This work was extended by Li and Choudhari [39] to develop computations for understanding the secondary instability. The results of Li and Choudhari's study showed the onset of the secondary instability moved forward as the initial amplitude of the stationary mode was increased. Contrary to subsonic experiments, the results found the type-II mode to have the highest amplitudes and growth rates.

Many of the high-speed experiments performed in recent years have used a 7° half-angle cone at 6° angle of attack to study the crossflow instability. Swanson [40] investigated boundary-layer transition over a 7° half-angle cone at 6° angle of attack using TSP and oil-flow visualization in the BAM6QT. Using the TSP, Swanson quantitatively measured the stationary mode of crossflow in both noisy and quiet conditions. Distributed roughness effects were also investigated. Five roughness elements, 0.5 to 0.7 mil in height and 9° apart, were applied in a spanwise line two inches from the nominally sharp nosetip. New crossflow vortices were observed near a ray 130° from windward.

Li et al. [41] used the parabolized stability equations (PSE) for computations on a 7° half-angle cone at 3° and 6° angle of attack at Mach 6 to complement Swanson's work in the BAM6QT [40]. Figure 2.4 depicts the flood contours of the N-factor location and disturbance frequency of the traveling crossflow. At 3° angle of attack, the traveling crossflow instability was found to have the largest N factors at the aft end of the cone around 120-135° from windward. The disturbance frequencies were between 20-60 kHz. Li et al. concluded that larger angles of attack increase the N factors of the stationary and traveling modes. The first- and second-mode instabilities were shown to have a minor effect from 3° to 6° angle of attack.

Muñoz et al. [16] measured the stability of a 7° half-angle cone at 6° angle of attack at Mach 6. The experiments were conducted at the Hypersonic Ludwieg tube Braunschweig, where noise levels were between 1 to 1.6% and the unit Reynolds numbers were between 1.94×10^{6}/ft to 3.87×10^{6}/ft. PCB pressure sensors were used to detect instability peaks near 20-50 kHz and 260-350 kHz at the 90° ray (from windward). The lower frequency waves were thought to be first-mode waves by the authors, but Perez et al. [42] used the linear PSE to suggest that the low-frequency waves were related to the traveling mode of crossflow. Chris Ward's experiments also

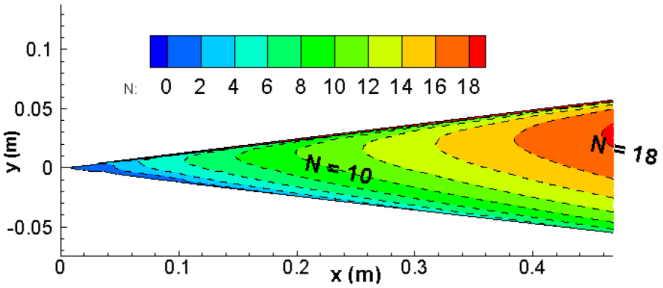

(a) N-factor values

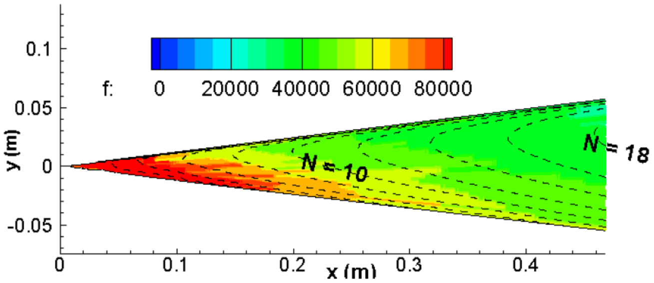

(b) disturbance frequency

Figure 2.4. Traveling crossflow contour plots at 3° angle of attack. Fig. 14c from reference [41].

shows these lower frequencies to be traveling waves [43]. The higher frequency waves at 260-350 kHz were deduced to be second-mode waves by Muñoz et al. which agree well with LST and LPSE results from Perez et al.

Swanson's preliminary measurements led Ward [44] to continue studying discrete roughness effects on hypersonic boundary layers. Ward compared no roughness elements to 50-dot and 72-dot roughness elements on a 7° half-angle cone at 6° angle of attack at a unit Reynolds number of approximately 3.20×10^6/ft. Ward showed that the location of the paint edge of the TSP could alter the spacing of the vortices. When the roughness elements were applied to the model, the vortices observed were thought to be generated primarily from the elements. Ward later suggested that the distributed roughness of the paint could be a more important parameter than the paint edge, but the roughness elements dominate vortex spacing [45]. Further experiments of roughness effects were conducted by Ward to be published December 2014 [46]. The models used in Swanson's and Ward's experiments were used in the author's own experiments.

Elliptic cone models have also been used to observe the crossflow instability. Traveling crossflow waves in hypersonic flow were first detected in 2000 by Poggie and Kimmel [47] on an elliptic cone at Mach 8. Low-frequency waves between 10-20 kHz were discovered near the yaw side of the elliptical cone. To characterize the traveling waves, a signal analysis was performed to determine the phase velocity and angle of the waves.

Borg et al. [15] used the BAM6QT to study the crossflow instability on an elliptical cone. Designed as a scaled model of the HIFiRE-5 vehicle, a 2:1 elliptic cone was fitted with Kulite XCQ-062-15A and XCE-082-15A pressure transducers between the vertex and co-vertex of the model. Juliano [48] found that this region develops strong stationary vortices as compared to the rest of the model. The results from Borg et al. show the traveling mode was detected with a peak in the power spectral density at 45 kHz for quiet flow at a unit Reynolds numbers between 2.40×10^6/ft to 3.57×10^6/ft. The experiments also revealed a destabilization effect of the traveling waves with increasing model surface temperature. Over 6 tunnel runs, the surface temperature was estimated to have risen 9°F. The amplitude of the traveling waves increased with each consecutive run. This lead to the authors hypothesizing that increased surface temperature destabilizes traveling waves.

3. FACILITY

3.1 Boeing/AFOSR Mach-6 Quiet Tunnel

The Boeing/AFOSR Mach-6 Quiet Tunnel (BAM6QT) is the largest of three hypersonic quiet tunnels in the world. The BAM6QT was designed as a Ludwieg tube to provide high Reynolds numbers at a reduced operating cost. More importantly, the tunnel was designed to operate with noise levels comparable to flight. In 2010, Steen [49] measured the BAM6QT noise level, calculated as the ratio of fluctuating pressure to the mean total pressure (P'/P_o), to be on the order of 0.01%, confirming the tunnel environment is comparable to flight conditions.

The Ludwieg tube design includes a driver tube, converging-diverging nozzle, diffuser, double-burst diaphragms, and vacuum tank. The schematic of Purdue's BAM6QT is illustrated in Figure 3.1.

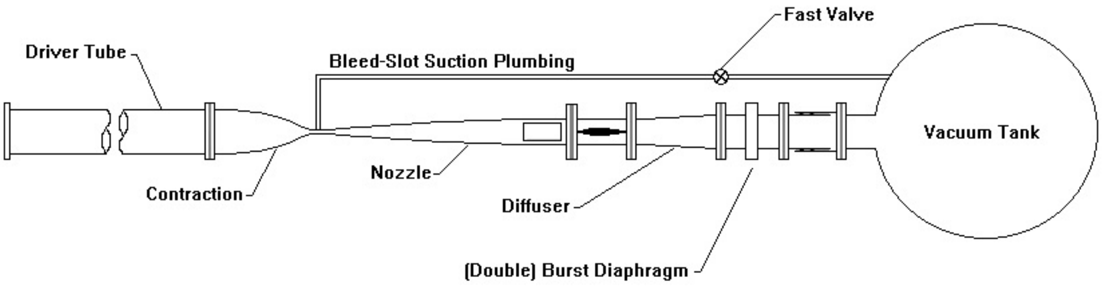

Figure 3.1. Schematic of the Boeing/AFOSR Mach-6 Quiet Tunnel.

To sustain a laminar nozzle-wall boundary layer and quiet flow, four features are required of the nozzle. First, the diverging section of the nozzle is polished to reduce any roughness and waviness that could trip the boundary layer. Second, the nozzle is elongated to limit Görtler instability growth on the concave surfaces. The third feature is a bleed-slot located 1 inch upstream of the throat of the nozzle. The bleed-slot is connected to the vacuum tank and flow is regulated by a fast valve. The suction from the slot bleeds off the boundary layer that develops along the contraction, allowing a new laminar boundary layer to grow along the nozzle. The final feature is the air filters. Before the air is pumped into the driver tube, the air is filtered to prevent particulates from scratching the mirror finish of the nozzle. Together, the features yield quiet flow conditions for total pressures up to 170 psia. Quiet flow conditions can be obtained for unit Reynolds numbers up to 4.04×10^6/ft.

Figure 3.2 shows a schematic of noise onset in the nozzle. A model is placed where the ideal quiet flow conditions exist, before the onset of noise and aft of where uniform flow develops. A window insert can be installed into the nozzle for optical access. Two inserts were created, a porthole window that features two 5-in diameter portholes, shown in Figure 3.3, and a 14×7-in rectangular window. The rectangular window is rated to 138 psig. Most testing was done above this pressure so the porthole window was exclusively used. A crack was found in the plexiglass of the rectangular window in August 2013. Since the discovery, the rectangular window has not been used. It will be replaced in the near future.

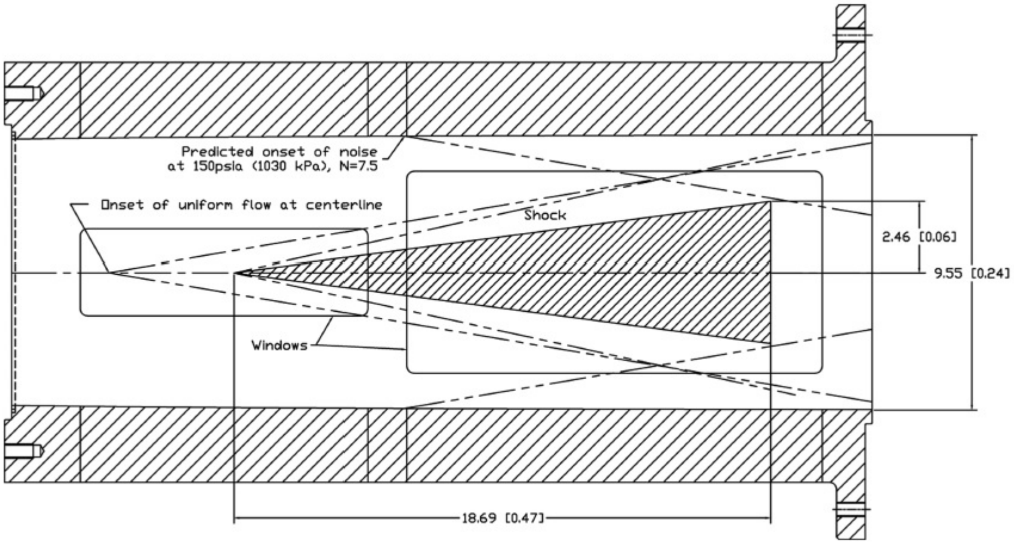

Figure 3.2. Schematic of BAM6QT with 7.5° cone model. Dimensions are in inches [meters].

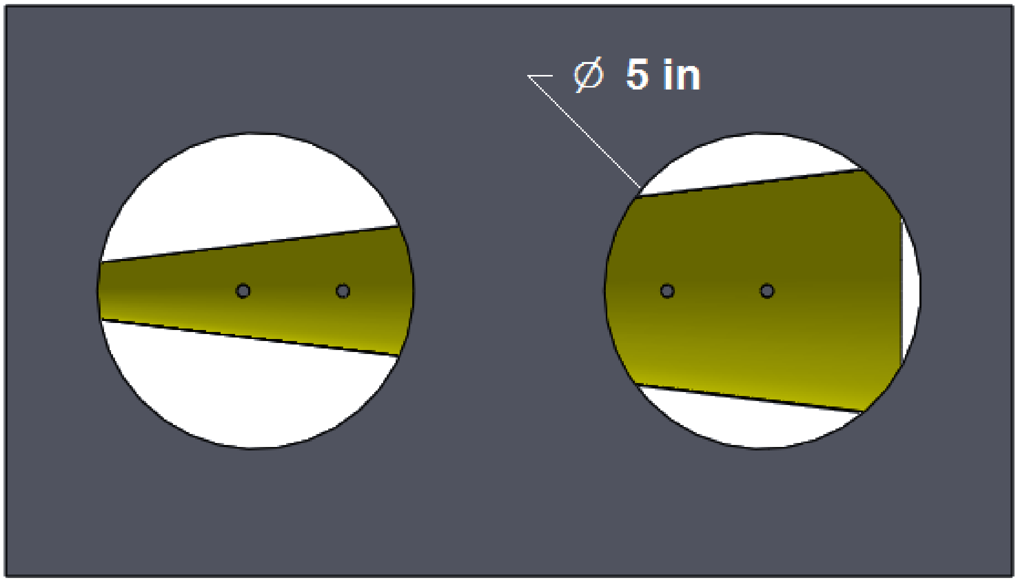

Figure 3.3. Porthole optical access with typical cone model.

The BAM6QT is operated by slowly charging the driver tube and nozzle to a desired stagnation pressure. Before the incoming air enters the driver tube, it is passed through a dryer system to remove water vapor. The dew point was recorded once a month between October to February. The dew point was between -4°F and 5°F during these months. The air was then filtered to remove large particulate. Two diaphragms separate the driver tube and nozzle from the downstream end that is connected to the vacuum tank. The gap between the diaphragms is maintained at half the pressure of the upstream end and vacuum. To start the flow, the air between the diaphragms is evacuated causing a larger pressure load on the upstream diaphragm. The upstream diaphragm breaks and then the downstream diaphragm breaks.

After the diaphragms are ruptured, a shock wave travels downstream into the vacuum tank and an expansion wave travels upstream. After the expansion wave passes the throat of the nozzle, Mach 6 flow begins. The expansion continues to traverse the length of the driver tube, reflects at the end of the tube, and then traverses back down. This process cycles many times, with the wave reflecting at the throat and the upstream end of the driver tube. The stagnation pressure drops in a stair-step manner after each reflection returns to the throat. During the run, the Reynolds number remains quasi-static between each reflection [50]. The total time of Mach 6 flow for each run is approximately 5 to 10 seconds. An increase in noise is observed after 2 seconds of run time [49].

3.2 Reynolds Number Calculation

The unit Reynolds number per foot can be calculated at any time during a run using the following equation:

$$Re/ft = \frac{PM}{\mu}\sqrt{\frac{\gamma}{RT}} \tag{3.1}$$

where P is the static pressure, M is the Mach number, μ is the dynamic viscosity, γ is the ratio of specific heats, R is the gas constant of dry air, and T is the static temperature. All variables are freestream values. Under quiet flow conditions, the Mach number is assumed to be 6. This assumption is within ±5% of the mean Mach number calculated from pitot measurements [49]. Under noisy flow conditions, the nozzle wall develops a thicker boundary layer effectively reducing the area ratio between the test section and throat. The Mach number for noisy flow is assumed to be 5.8, again within ±5%. The stagnation pressure is obtained from a Kulite pressure transducer in the contraction section of the tunnel. The static pressure can be obtained by using the isentropic relation,

$$P = \frac{P_o}{\left(1 + \frac{\gamma-1}{2} M^2\right)^{\frac{\gamma}{\gamma-1}}} \tag{3.2}$$

The initial stagnation temperature is obtained from a thermocouple at the upstream end of the driver tube. To calculate the static temperature of the flow during a run, the stagnation temperature at any time during the run must be calculated. Equation 3.3 is an isentropic relation that uses the initial readings of the stagnation pressure and temperature to determine the stagnation temperature at a given time during the run.

$$T_o(t) = T_{o,i} \left(\frac{P_o(t)}{P_{o,i}} \right)^{\frac{\gamma-1}{\gamma}} \tag{3.3}$$

The static temperature can then be determined using an isentropic relation similar to Equation 3.2,

$$T = \frac{T_o}{1 + \frac{\gamma-1}{2} M^2} \tag{3.4}$$

The dynamic viscosity is calculated using Sutherland's Law based on the static temperature of the flow in Equation 3.5. Note the calculation is in metric units.

$$\mu = 1.716 \times 10^5 \left(\frac{T}{273} \right)^{3/2} \left(\frac{384}{T + 111} \right) \tag{3.5}$$

4. MODELS

4.1 Cone Models

Two 7° sharp-tip cone models were built to study crossflow. Both models have a base diameter of 4 inches and a length of 16 inches. The models each have a 6061-T6 aluminum frustum and 17-4PH-Cond-H1100 stainless steel removable nosetips. The first cone, named the Crossflow Cone by designer Chris Ward [51], was used for the first two tunnel entries, to study the crossflow instability on a 7° half-angle cone at low angles of attack. The cone has six locations along one ray for sensors to be installed. Four PCB 132A31 fast pressure transducers and two Schmidt-Boelter (SB) gauges were flush-mounted to the surface of the cone along with a temperature sensitive paint (TSP) coating for those entries. The Crossflow Cone is pictured in Figure 4.1 with sensor positions labeled. The locations of each sensor are given in Table 4.1.

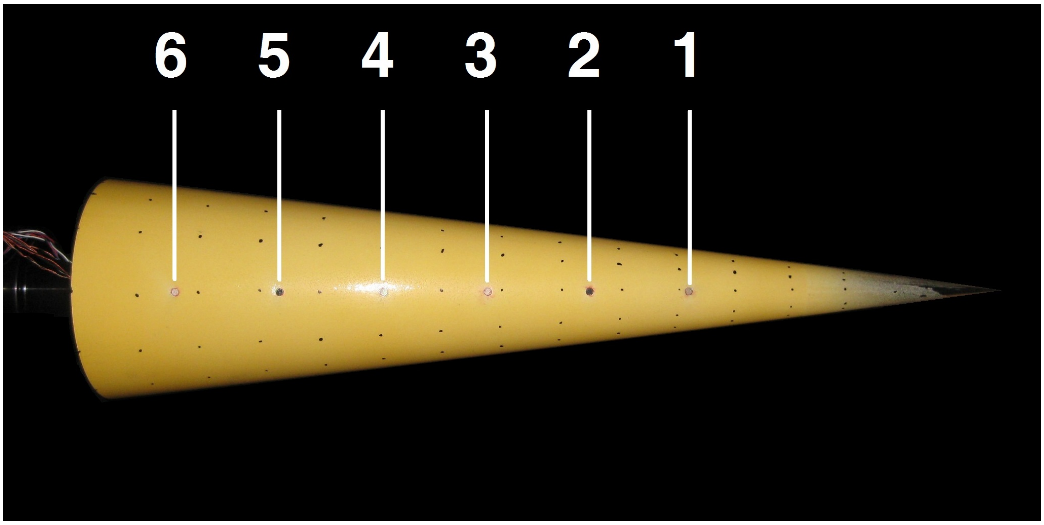

Figure 4.1. Crossflow Cone with TSP coating.

Table 4.1 Crossflow Cone sensor locations.

Position	Distance from Nosetip [in]	Sensor
1	5.80	PCB1
2	7.50	SB1
3	9.20	PCB2
4	10.90	PCB3
5	12.60	SB2
6	14.30	PCB4

The lack of spanwise pressure data that could be obtained per run led to the use of a second cone model. This model will be referred to as the Ward Cone as it was also used in Ward's experiments that will be published at a later date [46]. A schematic of the Ward Cone is shown in Figure 4.2, the sensor locations are found in Table 4.2 and Table 4.3. The Ward Cone features a spanwise set of sensor ports located 30°, 60°, and 90° away from Kulite Array 2 on either side of the sensor ray. Along with spanwise sensor ports, a line of sensor ports is located on one ray. This is similar to the Crossflow Cone, but with two Kulite arrays (smaller sensor ports that exclusively fit Kulite pressure transducers) replacing the PCB or SB ports. In order to determine traveling-wave properties, the Kulite ports were placed 0.10-in apart. This is less than the wavelength of a traveling wave. At 14 inches downstream of the nosetip, near the 120° ray from windward, the traveling mode has the most amplified wavenumber of approximately 80 which translates to a wavelength of 0.13-in [52]. The pattern of the array is not a concern when calculating traveling-wave properties, so long as three Kulites are within proximity of each other. These Kulite sensor locations were labeled k1 through k4 within each array. Sensors were not installed at positions 1 and 2 as well as Kulite Array 1. Dowel rods were fitted into the ports as flush as possible.

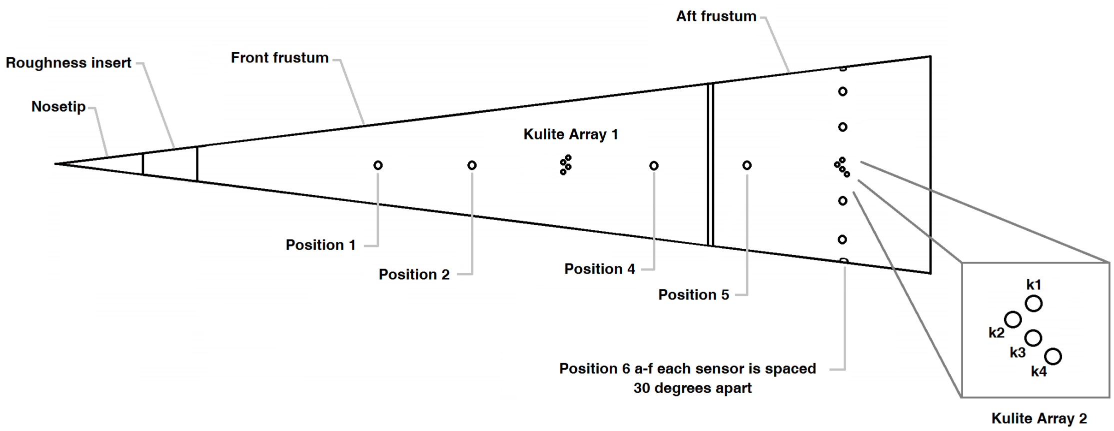

Figure 4.2. Ward Cone schematic.

Table 4.2 Ward Cone sensor locations. Positive degrees from sensor ray are towards the upward direction in reference to Figure 4.2.

Position	Sensor	Distance from Nosetip [in]	Degrees from Sensor Ray
1	-	5.80	0
2	-	7.50	0
4	SB1	10.90	0
5	PCB1	12.60	0
6a	PCB2	14.30	-90
6b	PCB3	14.30	-60
6c	PCB4	14.30	-30
6d	PCB5	14.30	30
6e	PCB6	14.30	60
6f	PCB7	14.30	90

Table 4.3 Ward Cone Kulite Array sensor locations. Positive degrees from sensor ray are towards the upward direction in reference to Figure 4.2.

Array	Sensor	Distance from Nosetip [in]	Degrees from Sensor Ray
1	-	9.25	2.55
1	-	9.21	0
1	-	9.25	-2.25
1	-	9.21	-4.50
2	k1	14.29	2.25
2	k2	14.21	0
2	k3	14.29	-2.25
2	k4	14.37	-4.50

4.2 Nosetip Radii

The nosetips of the Crossflow and Ward cone were measured with a Motic digital camera attached to a microscope. The radii of the Crossflow and Ward nosetips were measured to be 2.66 mil and 8.70 mil, respectively. Images of each nosetip are shown in Figure 4.3 and 4.4.

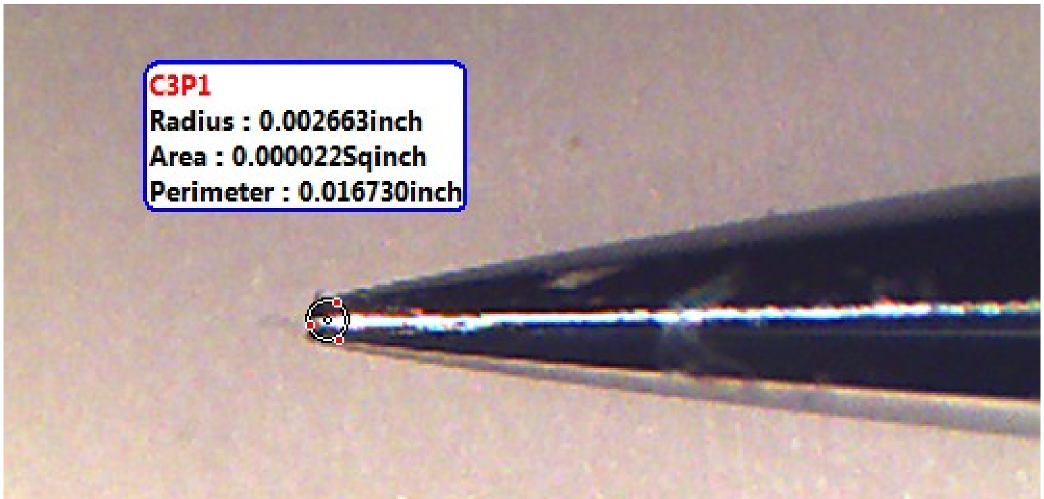

Figure 4.3. Crossflow Cone nosetip.

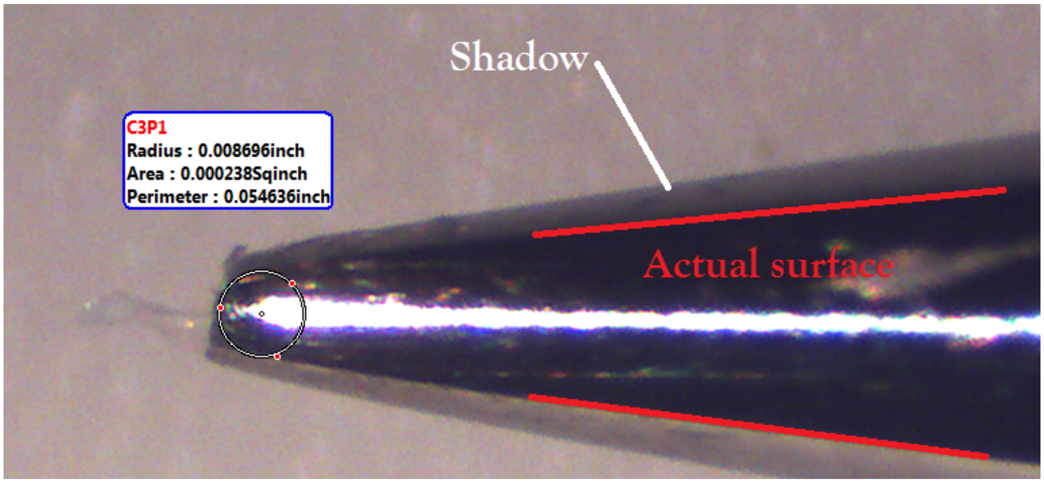

Figure 4.4. Ward Cone nosetip.

4.3 Model Positioning

Models are mounted on a sting on the centerline of the tunnel. It is beneficial to rotate models with respect to the camera to view different azimuthal rays. To achieve this, models are screwed into an angle of attack adapter, which is attached to the sting. By adding or removing shims between the adapter and the model, the position of the model is changed with respect to the adapter. Sensors fixed in the model then can be rotated to different azimuthal angles. Reference marks are drawn onto the adapter to determine azimuthal angle. The adapter is place in a rotary stage and rotated in ten degree increments. The shimming method is accurate to ±2.5 azimuthal degrees of difference.

4.4 Roughness Elements

Roughness elements were added to the Ward Cone by two methods. The first used nail polish to test if roughness has observable effects on stationary vortices at low angles of attack. Nail polish was chosen as a quick and non-destructive way of introducing roughness on the cone.

Torlon roughness inserts were designed by Chris Ward for an evenly distributed roughness pattern. The inserts were comprised of dimples spaced around the circumference of the insert at a distance of 2 inches from the nosetip. The dimples are formed when a pin is pressed into the Torlon. The displaced material rises above the surface around the pin. Once the pin is removed, a crater-like roughness is left, which is used to disturb the flow. His sixth Torlon insert consisted of 50 crater-like indentions, equally spaced circumferentially. In Ward's experiments, Torlon insert #6 showed large induced vortices at 6° AoA [46]. Insert #6 was used here for this reason.

5. INSTRUMENTATION AND ANALYSIS METHODS

5.1 Oscilloscopes

Three oscilloscopes were used to digitize voltage signals from the pressure transducers, temperature sensors, camera controls, and hot films. The Tektronix DPO7054, DPO7104, and TDS7104 Digital Phosphor Oscilloscope each have four channels that can be AC or DC coupled. The DPO7054 and DPO7104 model can record up to 50MB per channel and the TDS7104 model up to 4MB per channel. Both types of oscilloscopes were operated in Hi-Res mode, which records at the maximum sampling frequency and reduces the signal to the desired sampling frequency by averaging the collected data in real-time. This mode helps decrease the noise as well as providing a low-pass filter to the data [53]. Hi-Res mode also increases the vertical resolution from 8 to 12 bits by collecting data at a higher frequency than the desired sampling frequency and averaging in real time.

5.2 Hot Films

A Senflex hot-film array is positioned on the nozzle wall to detect if the boundary layer on the wall becomes turbulent. The array contains 35 sensors along a line parallel with the direction of the flow. One to two of these sensors, approximately 75 to 80 inches from the throat, are typically used per run. A Bruhn-6 Constant Temperature Anemometer controls the amount of current running through the hot film so that the resistance across the hot film is constant. In the DC Fluctuation mode, the output of the signal can be offset to ensure the signal can be read on the oscilloscope. The hot films are not calibrated so they are only used qualitatively to assess if the boundary layer has become turbulent.

5.3 Pressure Measurements

5.3.1 Kulite Pressure Transducers

Kulite pressure transducers can measure the mean pressure of a flow or the unsteady signal used for instability measurements. The transducers output a voltage linearly proportional to the pressure exerted onto the sensing face. The face is a small silicon diaphragm with a Wheatstone bridge of strain gauges embedded onto it. As pressure is applied, the diaphragm deforms, and a change in resistance of the strain gauges changes the voltage output.

A Kulite model XTEL-190-200A pressure transducer was used to measure the stagnation pressure during the run. This transducer is located near the contraction entrance where the Mach number is low and the pressure can be approximated as the stagnation pressure. Kulite model XCQ-062-15A pressure transducers have a higher resolution than the XTEL-190-200A, so they were installed on the Ward Cone to detect traveling crossflow waves and other lower frequency phenomena. XCQ-062 transducers have a resonant frequency near 300 kHz and have a flat frequency response up to about 60 kHz [54].

According to the manufacturer, the resolution of the transducers is infinitesimal. It is not known what the pressure resolution truly is so the resolution is assumed to be limited by the data acquisition. For typical Kulite XCQ-062 signals the oscilloscopes are set to 2 V/div, 10 divisions, and operate in Hi-Res mode for 12 bits. The sensitivities of the transducers are nominally 6 mV/psia. Custom in-house electronics were built to operate Kulites as well as amplify the signal with a gain of 10,000. The signals are also high-pass filtered at 800 Hz from this hardware. The resolution of the Kulite XCQ-062 is then on the order of 0.000008 psia.

The Kulite transducers were calibrated once per week of testing. The Kulite transducers were kept in situ and the tunnel was pumped down to 0.030-0.210 psia for calibration. This is near the expected static pressure at the surface of a 7° half-angle cone with a freestream Mach number of 6 for stagnation pressures between 30 and 170 psia. A Paroscientific Digiquartz 740-30A was used to measure pressures for the calibration, with an accuracy of 0.01% of the full-scale reading of 30 psia.

5.3.2 PCB Pressure Transducers

A PCB-132A31 pressure transducer is a piezoelectric crystal epoxied within a metal cylindrical housing. The PCB-132A31 sensor is able to measure high-frequency fluctuations. The sensors can measure above 1 MHz before reaching the sensor's resonant frequency, though the frequency response outside the flat 20 to 300 kHz range is not known, as discussed by Beresh et al. [55]. According to the manufacturer, the sensors are high-pass filtered at 11 kHz and the resolution of the sensors is 0.001 psia. The factory static calibrations were used for voltage-to-pressure conversion. The sensors are amplified and filtered using the PCB-482A22 constant-current signal conditioner.

PCB-132 sensors were recently discovered to detect second-mode waves by Fujii [56]. Numerous experiments have since used these sensors for detecting the second mode, a few are found in Refs. [57, 58]. The sensors were then chosen to be installed in both cone models for their small size, 0.3 inch length and 0.125 inch diameter, and effectiveness to detect second-mode waves. Seven sensors were used on the Ward Cone to compare the instabilities circumferentially on the cone.

5.3.3 Power Spectra

A power spectrum was computed for each Kulite and PCB transducer for each run. These data are normalized by the mean pressure. The local mean pressure of the flow is calculated from the theoretical static pressure behind an oblique shock for a 7° half-angle cone at zero angle of attack. This calculation comes from the Taylor-Maccoll equations. This is because the Kulites cannot measure this low pressure accurately.

When the cone is inclined relative to the freestream, the incident angle of the flow to the cone depends on the angle of attack and the azimuthal position. The tangent-cone method was used to calculate the local surface pressure at a given angle of attack and azimuthal ray, to normalize the pressure fluctuations. This is done by using the Taylor-Maccoll equations from the effective half-angle of the cone. Equation 5.1 shows the effective angle of attack used as a function of angle of attack and azimuthal ray.

$$\theta_{tanc} = \theta + \alpha * \cos\phi \tag{5.1}$$

where θ is the half-angle of the cone, α is the angle of attack, and ϕ is the azimuthal angle. Note that the windward ray is at $\phi = 0$.

The subscript *tanc* was used to denote the new effective half-angle, and in the subsequent pressure calculations the subscript *mean* was replaced when the tangent-cone calculation was used.

Both Kulite and PCB transducer signals were AC coupled and acquired at 2 MHz, well above expected instability frequencies. Kulite sensors were digitized with a vertical resolution of 2 V/div while the PCB transducers were obtained at 10 mV/div. The power spectral density (PSD) can reveal instabilities which can appear as discrete peaks within the spectra. Both types of transducers were processed using a Blackmann window of 200 windows, 1000 samples per window, and a 50% overlap. The frequency resolution for the PSDs as calculated to be 2.0 kHz. The total time processed was 100 ms. This is half the amount of time it takes for the expansion wave to travel along the driver tube and reflect back to the converging section of the nozzle. An approximately constant stagnation pressure is observed between expansion wave reflections so the data is processed between the reflections. The Reynolds number is assumed to be constant over the time processed.

5.4 Temperature Measurements

5.4.1 Thermocouples

Thermocouples were used to determine the temperatures on the model. There are many types of thermocouples, but only two types were chosen for this research. Type K thermocouples are composed of chromel (90% nickel and 10% chromium) and alumel (95% nickel, 2% manganese, 2% aluminium, and 1% silcon). Type T thermocouples are composed of copper and constantan (55% copper and 45% nickel). Voltage is created when the sensing junction of the device experiences a temperature that is dissimilar to the reference junction within the device. The voltage is then referenced to the National Institute of Standards and Technology (NIST) ITS-90 database or to an appropriate curve, in order to find the temperature.

Paste-On Thermocouples

Due to the added heat that is transfered to the model after each run, a thermocouple was needed to monitor the temperature of the cone's body. An Omega SA1-K-72 self-adhesive thermocouple was used for quick install without the need for epoxy, cement, or other permanent fixtures. The Type-K sensor thermocouple was temporarily pasted onto the base of the cone. The Type-K sensor accuracy is ± 4.0°F or ± 0.75% with a response time of 0.3 seconds. The thermocouple was wired to an Omega MCJ Type-K cold junction compensator and then connected to an oscilloscope. The signal was sampled at 500 S/s.

Schmidt-Boelter Gauge

The Medtherm Schmidt-Boelter (SB) gauge is a 0.125-in diameter sensor that contains a thermopile, which is an array of thermocouples. The array forms a differential thermoelectric circuit. Model 8-1-0.25-48-20835TBS was used throughout the experiments. This model consists of a T-type thermocouple that gives a range of 0 - 1.1 $\frac{BTU}{ft^2-s}$. The factory calibration for this SB gauge was 6.95 $mV/\frac{BTU}{ft^2-s}$.

Three signals can be obtained from the SB gauge. Two of the three signals are the surface and body thermocouple signals and the third is the heat flux signal from the thermopile. Along with the paste-on thermocouple, the body thermocouple was used to confirm the model-body temperature. The body thermocouple was a Type T with an accuracy of ± 1.8°F or ± 0.75%, with a response time of 0.3 seconds. It was sampled at the same rate as the paste-on thermocouple. The SB gauge signal was connected to a Stanford Research Systems SR560 amplifier with the gain set to 100. The amplifier output was connected to an oscilloscope, where the signal was sampled in Hi-Res mode at 50 kS/s with a vertical resolution of 100 mV/div. The SB gauge was mounted flush to the surface of the temperature sensitive paint and was primarily used to calibrate the temperature sensitive paint.

5.4.2 Temperature Sensitive Paint

Temperature sensitive paint is a luminescent mixture that is applied to a surface to observe global temperature gradients and heat transfer. Compared to discrete sensors, TSP is a non-intrusive technique that offers high spatial resolution [59]. TSP is excited with the appropriate wavelength of light which causes the paint to fluoresce. The fluorescence from the TSP is then recorded with a charged-coupled device (CCD) camera.

TSP Photophysics

Luminescent molecules are excited by absorbing a photon of radiation. This absorption elevates the luminescent molecules to the first singlet electronic state. The path in which the electrons return to a ground-energy state is dependent on a combination of radiationless and radiative processes [60]. From the singlet state, electrons can radiatively return to a ground state, known as fluorescence, or vibrationally relax to a lower-energy triplet state and then return to a ground state by radiation transition, known as phosphorescence. The molecules that fluoresce emit longer wavelength photons as they return to the ground state. Higher temperatures result in increased radiationless transition and decrease the intensity of the fluorescence. The intensity of the fluorescence can be correlated to the inverse of the temperature.

Painting Method

To reduce heat flux into the model, a layer of insulation was sprayed on the model. Ward [51] showed that Top Flite LustreKote model airplane spray paint is currently the best choice for insulation spray. The LustreKote brand gave a smoother finish than the other paints and also was sprayed from a can that did not have to be thinned. Four coats of LustreKote primer were used with four additional coats of the jet-white color. After the final coat, the model is left to dry for 24 hours and subsequently sanded with 200, 500, and 3000 grit sandpaper. The insulation layer reduces heat conduction into the model and increases the TSP signal.

After the insulation layer has been sanded, the TSP is created and applied. The mixture is made of luminescent molecules and a polymer binder that are dissolved in a solvent. The luminophore, 99.95% Tris(2,22-bipyridine) dichlororuthenium(II) Hexahydrate(Ru(bpy)), commonly called Ru(bpy), was chosen for the TSP mixture. The Ru(bpy) particles are dissolved in ethanol. AmTech AM-500-4 Urethane Clearcoat and AmTech AM-570-12 activator are automotive clearcoat refinishers that were chosen as the polymer binder. The final mixture is then sprayed onto a model with a pressurized spray gun. The paint is applied to the aft end of the cone and feathered towards the upstream end. This smooths a possible step from the bare surface to the final paint thickness. The Crossflow Cone was feathered near the nosetip while the Ward Cone was feathered near 8-10 inches from the nosetip. The model is kept in a ventilated room to dry for 24 hours. The model is then sanded to reduce roughness-induced instabilities. The insulating layer and TSP were applied by following the directions described in Ref. [61].

TSP Apparatus

Figure 5.1 is a sketch of a typical TSP apparatus and the equipment needed. The absorption spectra of Ru(bpy) has peaks between 250-300 nm and 450 nm. The longer wavelength peak was chosen since light wavelengths below 400 nm would require a specially made window. Instead, two blue light emitting diode (LED) arrays were used to excite the Ru(bpy) peak at 464 nm. The blue LED arrays were the Innovative Scientific Solutions Inc. (ISSI) LMA LM4 array and the ISSI LM2xLZ-465 LED array. The latter is more powerful and requires water channels within the device to cool it. Building water is connected to a ISSI LM2xLZ-DM pulsed driver where a HP E2620A power supply triggers the water to be pumped into the LM2xLZ-465 LED array. The trigger is connected to a switch that also controls the power to the other LED array, for convenience. As the LED array excites the TSP, longer wavelength photons are emitted through fluorescence and subsequently recorded by a CCD camera.

The Cooke Corporation PCO.1600 14-bit CCD camera was used and controlled from a computer using CamWare software. The camera was fitted with a 50 mm focal length lens to image the model through one porthole window. An orange filter with a 556 nm wavelength high-pass covered the lens to decrease the amount of incident light that enters the camera, while allowing the TSP-emitted wavelengths to pass through. The CCD camera can use 1600x1200 pixels, but was reduced to 800x600 with a 2x2 binning to reduce image noise. The camera is set to an exposure time between 8-11 ms with the camera imaging on a 30-35 Hz cycle. The exposure time and imaging frequency are adjusted to get the maximum light intensity without saturation. The camera was triggered from a Agilent 33220A function generator, which was triggered from the TDS7104 oscilloscope when the diaphragms burst.

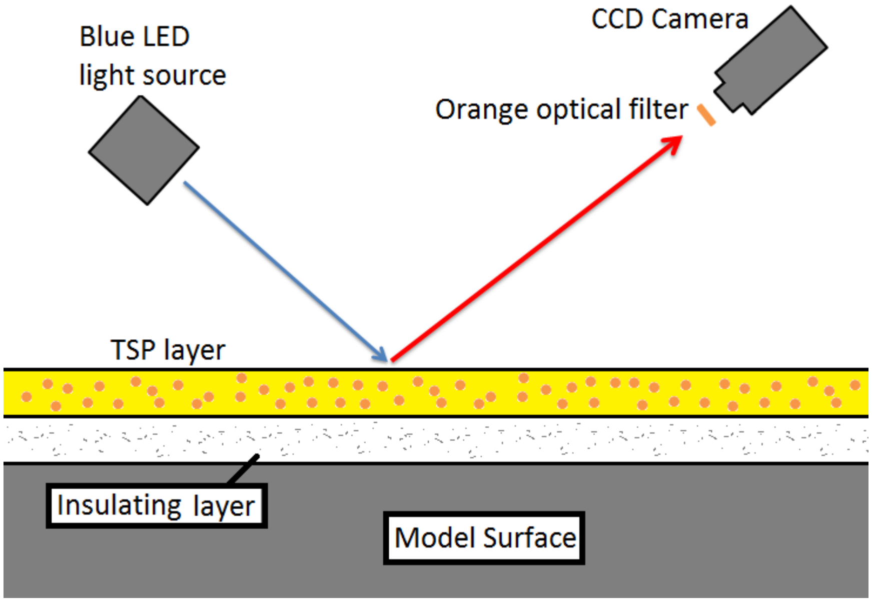

Figure 5.1. Sketch of TSP apparatus.

With the CCD camera centered on a porthole window, the LED arrays were arranged on either side of the camera to reduce shadowing from the rim of the porthole windows. Due to sediment buildup in the water-cooled LED later entries only used the LMA LM4 LED array. The camera was positioned away from the window to image the aft part of the cone that could be imaged in one porthole. Figure 5.2 shows the typical placement of the camera and LMA LM4 LED array.

TSP Image Post-Processing

The luminescent intensity from the TSP varies with paint thickness and the luminophore distribution in the paint. To correct for these variables, three images were required. Two reference images were needed as well as the images from the experimental run. A dark image was taken with all lights off. A wind-off image was then taken with the blue LED lights on, but with no flow inside the tunnel. Both of these images were collected within a minute before starting the tunnel so the model temperature (and the TSP) would be as close to initial stagnation conditions as possible. For the

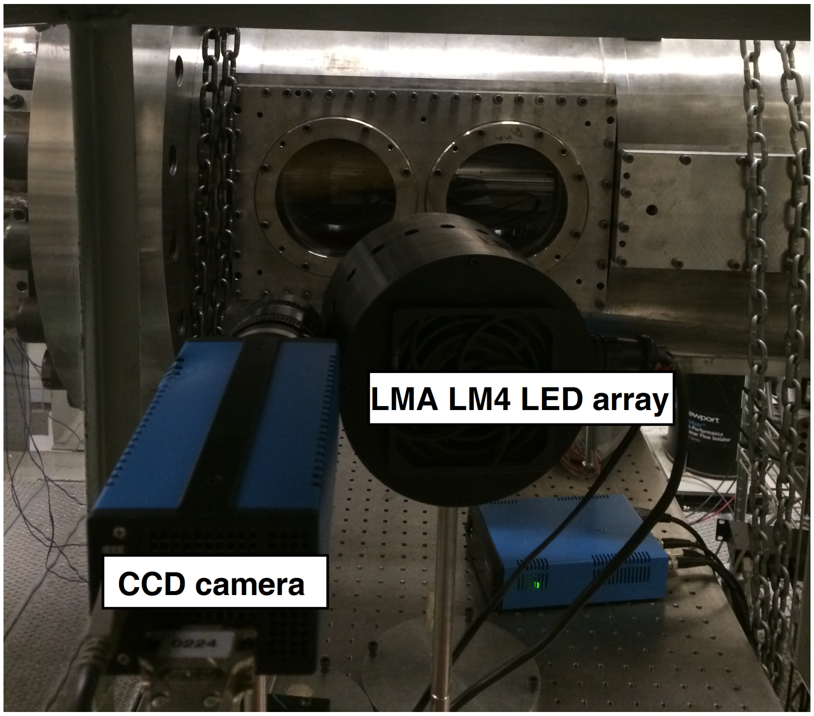

Figure 5.2. Typical CCD camera and LED array placement.

dark and wind-off images, 20 to 30 sequential images were collected and averaged. The wind-on images were taken while the LED lights were on and were recorded for 7-8 seconds starting when the diaphragms burst.

The dark images were subtracted from both the wind-on and wind-off images to reduce noise. A ratio of the light intensities was then calculated to normalize the TSP variations. Equation 5.2 is the basic formula for converting the TSP intensity to temperature:

$$\Delta T = f\left(\frac{I_{on} - I_{dark}}{I_{off} - I_{dark}}\right) \tag{5.2}$$

The exact conversion depends on the type of TSP applied and the type of calibration used. Figure 3.13 in Reference [59] depicts experimental temperature dependencies for various TSP formulations. The calibration of Ru(bpy) was linearly fit between the ambient temperatures of 59°F and 140°F. After shifting the reference temperature from -238°F to the pre-run model temperature (T_{ref} with units of °F), Equation 5.2 becomes the following:

$$\Delta T = (192 - T_{ref}) \left(1 - \frac{I_{on} - I_{dark}}{I_{off} - I_{dark}}\right) \tag{5.3}$$

Calculating Heat Transfer from the TSP Images

The heat transfer imparted onto the model surface can be calculated from Fourier's law of heat conduction. This equation is simplified through a few assumptions. One-dimensional conduction in the radial direction was assumed. Work by Ward [51] found that the base temperature (temperature of material underneath the insulation layer) can be assumed constant spatially and temporally at near maximum quiet stagnation pressure in the BAM6QT. His tests showed the spatial uniformity of the base temperature was accurate to within 4% and temporally constant over the first 10 seconds of a run with minimal temperature change. His tests, however, were limited to runs at the maximum pressure of 140 psia due to strength limitations of the rectangular window. With these assumptions, Fourier's law can be modified to Equation 5.4:

$$q'' = \frac{k}{L} \left(\Delta T + T_{ref} - T_b\right) \tag{5.4}$$

$$\Delta T = T - T_{ref} \tag{5.5}$$

where k is the thermal conductivity of both TSP and insulating layers, L is the depth of both layers, and T_b is the base temperature of the model.

Over each run, a calibration method was used to obtain global heat transfer from TSP data using SB gauges. Once the diaphragms burst, an expansion fan travels upstream and passes over the model. This causes the model to experience a sudden decrease in heat flux. A subsequent sharp increase in heating is caused by hot gas, upstream of the model, passing over the model just before Mach-6 flow begins. After the tunnel is started the heat flux tapers to an approximate steady state. The intensity of the TSP is collected for 7-8 seconds starting when the diaphragms burst. A typical plot of the calibration is shown in Figure 5.3.

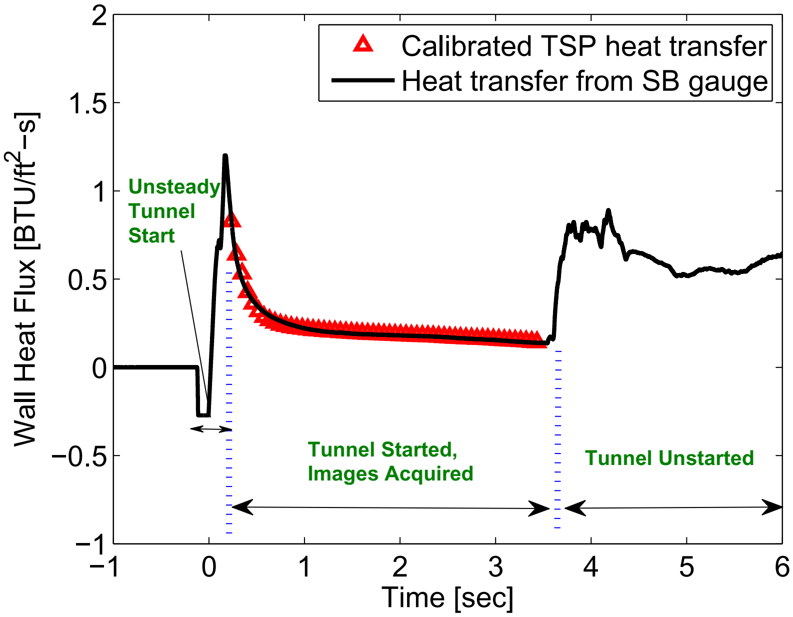

Figure 5.3. Typical TSP calibration using a SB gauge. E6R6, 4° AoA, quiet flow, Torlon insert, SB gauge at $x = 10.9$-in. on the 120° ray. $Re = 3.68\times10^6$/ft, $P_o = 156.8$ psia, $T_o = 299.2$°F, $T_w = 93.4$°F.

To calibrate the TSP, a square patch of TSP is chosen near the SB gauge in an area of equal heat transfer. Knowing the heat transfer from the SB gauge, the base temperature of the model, and the temperature gradient from the intensity of the TSP (from Equation 5.3), a least-squares fit is used to calibrate the TSP to infer the global heat transfer on the model. From the calibration, the $\frac{k}{L}$ and T_b values can be inferred. From these, the TSP image can be converted to heat transfer.

Uncertainties in Comparison-Patch Location

The square patch of TSP that is used for calibration is not always taken at the same position, due to turbulence or stationary crossflow in the vicinity of the SB gauge. The TSP of Entry 3 Run 2 (E3R2) was used to compare different patch locations to the theoretical laminar heat transfer for an axisymmetric cone. Figure 5.4 shows the heat transfer contour with the five patches chosen on the cone. The first three patches were chosen around the SB gauge while the fourth and fifth patches were well away from the sensor. After the patches were used to convert the TSP to heat transfer, an axial profile was taken near the center of the image. Ten profiles, each a pixel in width, were averaged and compared to theory on Figure 5.5. Patches 1-4 showed similar heat transfer across the distance of the cone and compared well to theory. The most-aft patch showed a higher heat transfer than the rest.

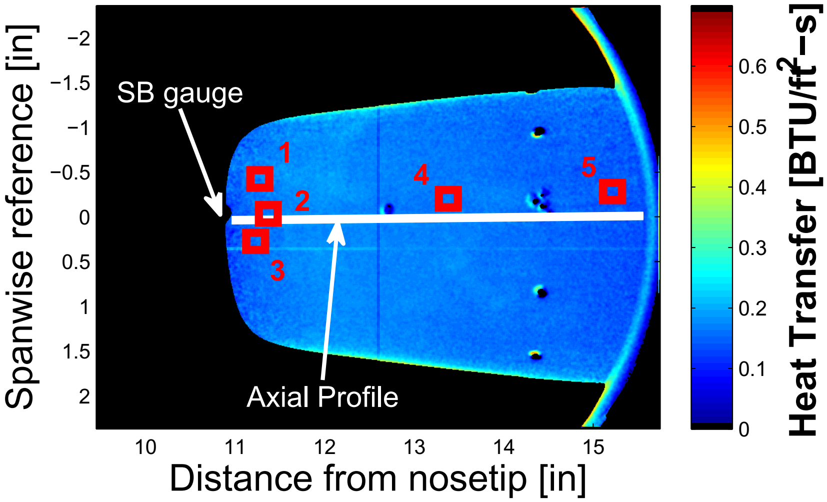

Figure 5.4. Heat transfer contour of E3R2. 0° AoA, quiet flow, smooth surface. $Re = 3.25 \times 10^6$/ft, $P_o = 137.6$ psia, $T_o = 295.5$°F, $T_w = 79.5$°F.

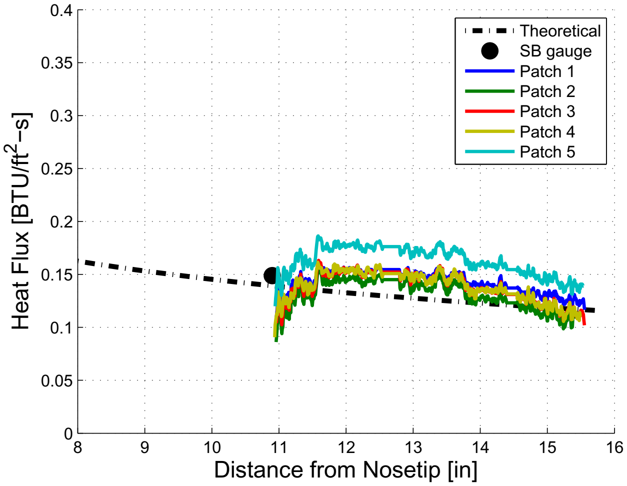

Figure 5.5. Axial heat flux profiles of E3R2 for calibrations from each patch. Theoretical heat transfer and SB gauge readout at time of process are also shown.

Another patch comparison was analyzed for a 4° AoA case. Figure 5.6 shows the heat transfer contour of E4R1 with the five patches similar to the last comparison. The fourth patch was chosen near the windward side where an increase in heat transfer was observed. An axial profile at the 80° ray was created for each patch, shown on Figure 5.7. Similar to the axisymmetric case, the patches nearest the SB gauge show similar heat transfer profiles and agree well at the SB gauge location. The fourth and fifth patches, however, did not have the same heat transfer levels near the SB gauge. Patch 4 was found to have heat transfer levels 16% lower than what the SB gauge recorded and Patch 5 was 79% higher. Since the calibration uses the patch to convert the full TSP image to heat transfer, the difference in heat transfer is offset over the entire profile. Therefore the comparison patch must be placed near the SB gauge to obtain the closest match to actual conditions. Problems can occur when transition or vortices cross over SB gauges. Temperature-difference plots are then used instead of heat transfer contours because of inaccurate calibrations.

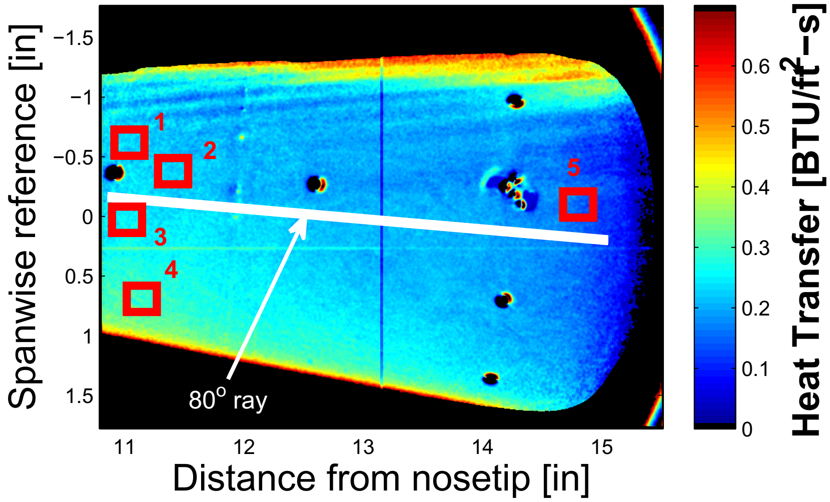

Figure 5.6. Heat transfer contour of E4R1. 4° AoA, quiet flow, smooth surface. $Re = 3.65\times10^6/\text{ft}$, $P_o = 156.8$ psia, $T_o = 301.7$°F, $T_w = 74.6$°F.

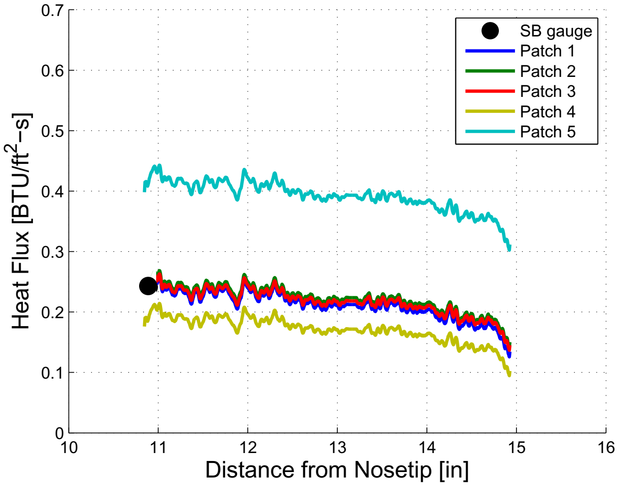

Figure 5.7. Axial heat flux profiles of E4R1 for calibrations from each patch, SB gauge readout at time of process.

5.5 Roughness Measurements

Two devices were used to measure the height of the roughnesses on the cone. The Mitutoyo SJ-301 profilometer is a surface roughness tester with a hand-held stylus that can be raked over a surface to measure roughness heights over discrete 0.3-in strips. The roughness height along each strip is recorded by the profilometer and the average and RMS profiles can be determined. The radius of the stylus is specified by the manufacturer at 0.2 mil. The vertical resolution of the profilometer was 0.004 mil.

The second device used was a Keyence VR-3050 digital microscope. The VR-3050 is a non-contact measurement device that uses incident light to determine surface heights. The microscope evaluates surfaces in a top-down orientation to measure two-dimensional features with a depth component. The resolution of the VR-3050 is 0.02 mil for a field of view of 240 × 240 × 180 mil. This device was used for demonstration purposes and only one Torlon insert was measured. The BAM6QT group is currently exploring the purchase of a 3D digital microscope with similar features.

To preserve roughness samples, a negative-mold technique was used. Struers RepliSet-T3 is a fast curing two-part silicon rubber that forms a negative outline on the surface it covers. Once hardened, the mold can be removed from the surface and stored. By removing the mold from the surface of a model, the mold can be placed on a flat surface to measure roughness without curvature effects from the geometry of the cone. According to Struers, the resolution of the mold is specified to 0.004 mil.

Each newly painted cone was evaluated by the profilometer to approximate the average roughness of the paint coat. The profilometer and digital microscope quantified the Torlon and nail-polish roughnesses. The results of the roughness heights are presented in the subsequent sections.

6. RESULTS AT ZERO ANGLE OF ATTACK

The cone was first tested to observe the state of the boundary layer without crossflow effects. Three unit Reynolds numbers were tested for both quiet and noisy conditions.

6.1 Tunnel Noise Effects

Using the Crossflow Cone, PCB sensors along one ray of the cone were able to detect fluctuations near 300 kHz under quiet and noisy conditions. Figure 6.1 shows the power spectral density (PSD) of two runs at quiet and noisy conditions near the same Reynolds number. For axisymmetric cases, the pressure fluctuations were divided by the mean pressure at the surface of the cone to normalize the differences in stagnation pressure. The dotted lines show three traces of PCB sensors under noisy flow and the solid lines show the same PCB sensors under quiet flow.

Under quiet flow conditions, no clear disturbances are observed probably because the Reynolds number was too low. Under noisy flow conditions, a large peak was detected around 300 kHz by the PCB sensor 9.2-in from the nosetip (x = 9.2-in). The amplitude of the peak grows an order of magnitude by x = 10.9-in. At x = 14.3-in an elevated broadband spectrum can be seen. This increase in noise over all frequencies usually represents turbulence. The peak at 300 kHz has been found to be the second-mode instability for this particular geometry, see Ref [62]. The peak also shifts slightly to a lower frequency further downstream, as expected. As the boundary layer thickens downstream, the second-mode frequency decreases.

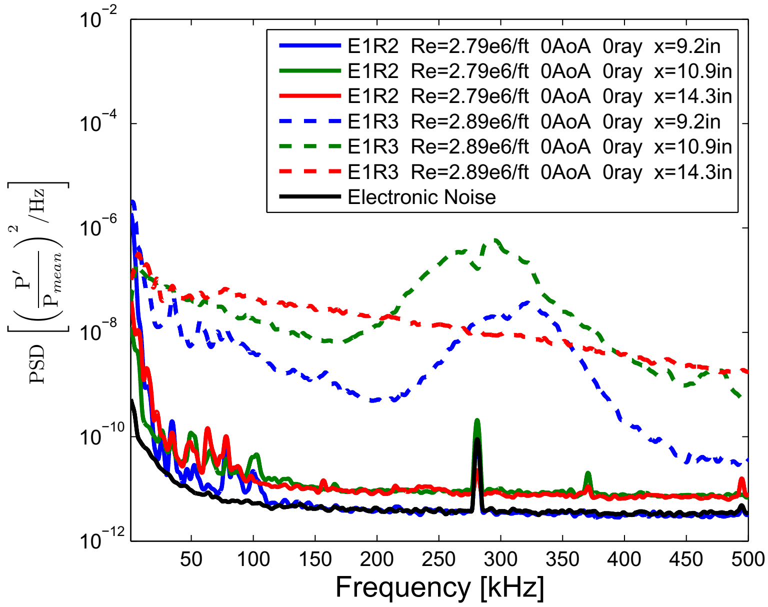

Figure 6.1. PSD of quiet results (solid) for E1R2 $Re = 2.79{\times}10^6$/ft, Noisy results (dotted) E1R3 $Re = 2.89{\times}10^6$/ft, all traces from PCB sensors.

TSP was applied for the axisymmetric cases. The first entry had flaws in the painting and lighting of the TSP, but the data still show trends that can be compared to the PSD. Figure 6.2 shows the quiet flow case for $Re = 2.89{\times}10^6$/ft. A constant radius arc can be seen towards the aft end of the cone. This is a lighting effect caused by the blue LED reflection from the porthole window. A streak of reduced heat flux can be seen at the last sensor location and spreading towards the upper right-hand corner of the image. This area was a flaw in the painting method used for this entry. The area had much less TSP applied and therefore did not give consistent heat transfer values. Figure 6.3 shows the noisy run at a similar Reynolds number. Both flaws can be seen in this image as well. More importantly, transition can be seen in the image. A rise in heat transfer shows the onset of transition to a turbulent boundary layer. The turbulent region on the cone can be compared to where the furthest PCB sensor downstream detected increased noise across all frequencies in Figure 6.1.

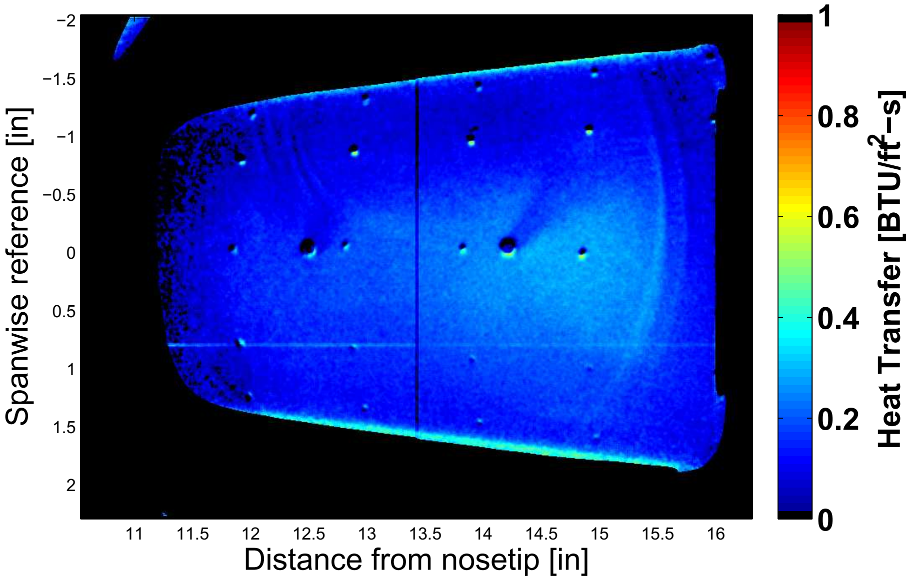

Figure 6.2. Heat transfer contour of E1R2 0°AoA, quiet flow, smooth surface. $Re = 2.79 \times 10^6$/ft, $P_o = 114.9$ psia, $T_o = 283.5$°F, $T_w = 77.3$°F.

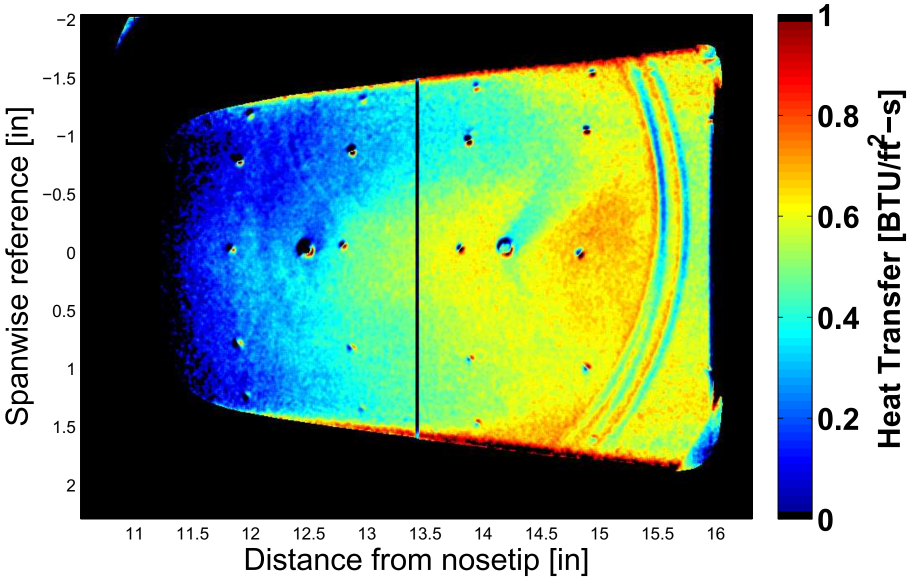

Figure 6.3. Heat transfer contour of E1R3 0°AoA, noisy flow, smooth surface. $Re = 2.89 \times 10^6$/ft, $P_o = 113.4$ psia, $T_o = 293.9$°F, $T_w = 83.3$°F.

Similar trends were found at higher stagnation pressures. Figure 6.4 shows quiet flow spectra much like the lower Reynolds number case without visible peaks. There are peaks near 300 kHz in the noisy flow spectra. Increasing the quiet Reynolds number to 3.67×10^6/ft, Figure 6.5 begins to show second-mode peaks around 275 kHz for quiet conditions. At $x = 9.2$-in a second-mode peak can still be seen under noisy flow, but further downstream at $x = 10.9$-in the boundary layer is transitioning and finally at $x = 14.3$-in the spectra is broad and flat.

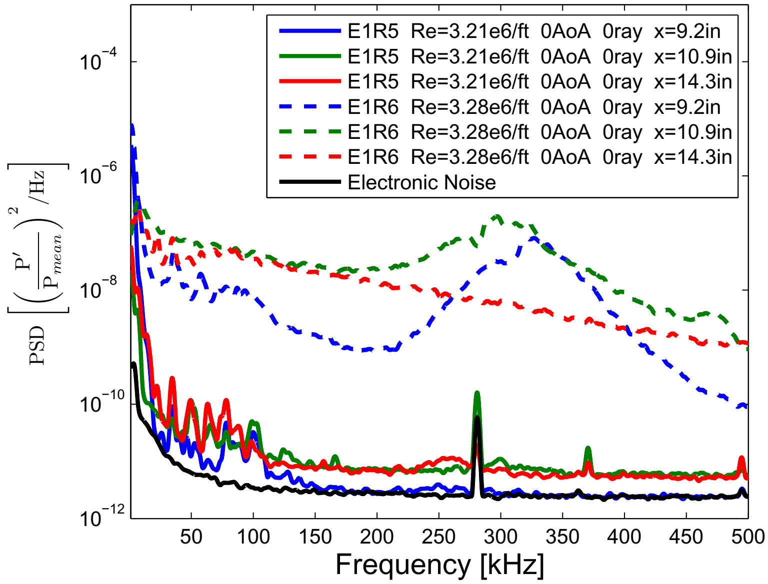

Figure 6.4. PSD of quiet results (solid) for E1R5 $Re = 3.21 \times 10^6$/ft, Noisy results (dotted) E1R6 $Re = 3.28 \times 10^6$/ft, all traces from PCB sensors.

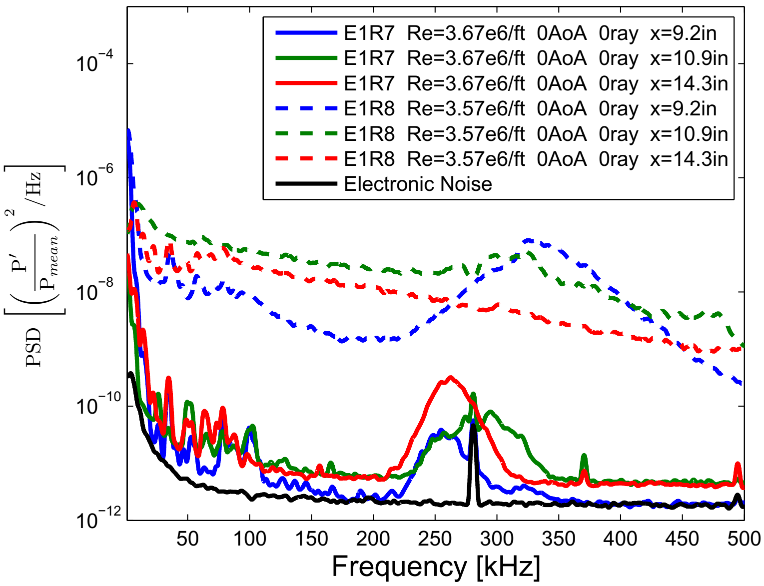

Figure 6.5. PSD of quiet results (solid) for E1R7 $Re = 3.67{\times}10^6$/ft, Noisy results (dotted) E1R8 $Re = 3.57{\times}10^6$/ft, all traces from PCB sensors.

6.2 Reynolds Number Comparison

The three Reynolds number cases were plotted together in Figure 6.6 for the PCB sensor located 9.2-in downstream of the nosetip. Frequency was scaled by the square root of the Reynolds number, with the characteristic length based on distance from the nosetip, to remove boundary-layer thickness effects. The peak remains at the same scaled frequency, as expected. The second-mode peak near 175 scaled-Hz slightly increases in amplitude from $Re = 2.89{\times}10^6$/ft to $Re = 3.57{\times}10^6$/ft, but saturates at the highest Reynolds number case. Figure 6.7 is plotted with the same runs for the PCB sensor that is 1.7-in further downstream. The spectra shows that an increase in Reynolds number gradually leads to breakdown of the second mode, where the second-mode peak appears to flatten. This result has also been observed by Berridge [63] for a 7° half-angle cone at zero angle of attack using the Langley Mach-6 tunnel. A small frequency band of reduced power is seen on all three cases where the second mode is shown. From the electronic noise spectra, this frequency band might be caused by an fault in the PCB sensor at that particular frequency.

Figure 6.8 compares the three Reynolds number cases under quiet flow at $x = 14.3$-in. A peak near 250 kHz is detected at $Re = 3.21{\times}10^6$/ft and then with a larger amplitude near 265 kHz at $Re = 3.67{\times}10^6$/ft.

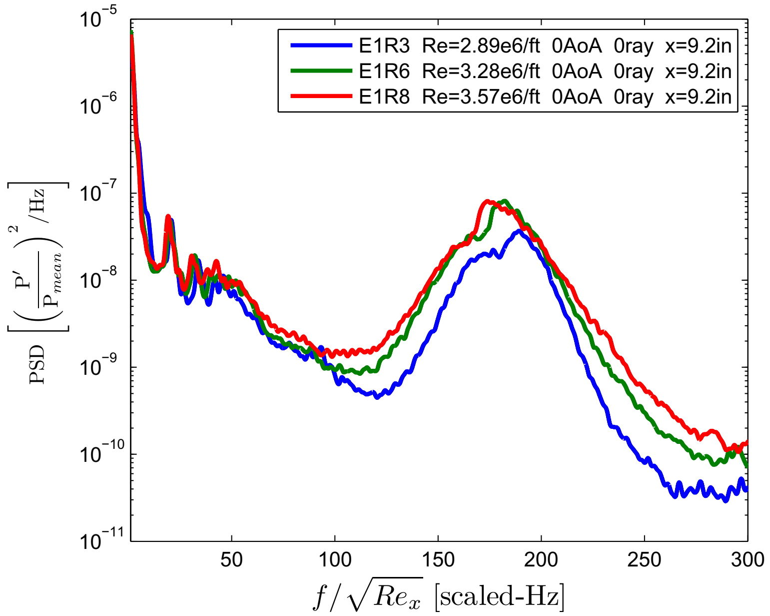

Figure 6.6. PSD of noisy spectra for runs E1R3 (blue), E1R6 (green), and E1R8 (red), all traces from PCB sensor at $x = 9.2$-in.

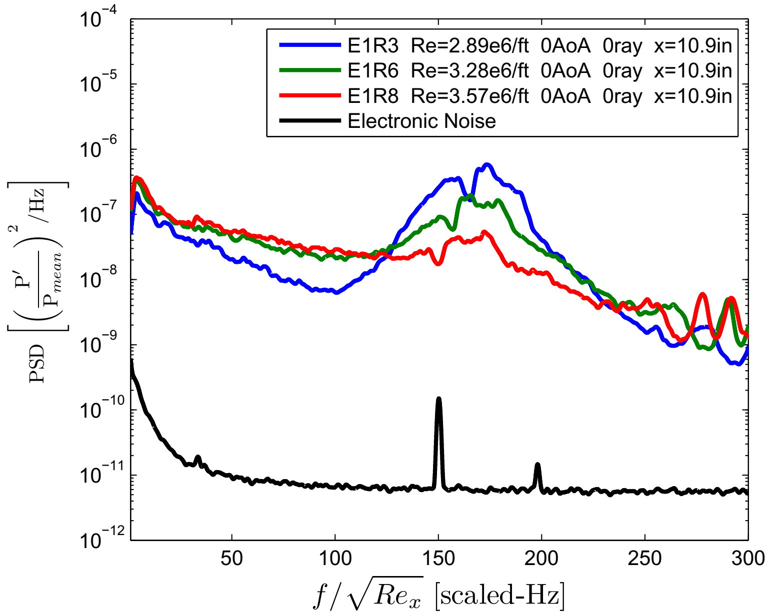

Figure 6.7. PSD of noisy spectra for runs E1R3 (blue), E1R6 (green), and E1R8 (red), all traces from PCB sensor at $x = 10.9$-in.

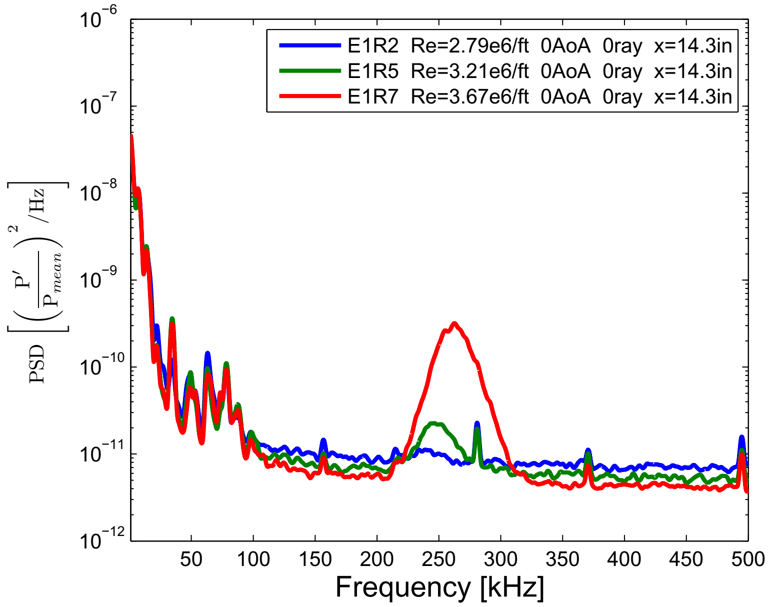

Figure 6.8. PSD of quiet spectra for runs E1R2 (blue), E1R5 (green), and E1R7 (red), all traces from PCB sensor at $x = 14.3$-in.

6.3 0° AoA Symmetry

To determine how symmetric the cone was relative to the flow, a run was conducted with PCB sensors spaced 30 degrees apart azimuthally over the cone at x=14.3-in. The sensors were expected to detect the second mode with similar magnitudes and frequencies. Figure 6.9 shows each PCB sensor referenced from the Kulite Array 2 position, where positive and negative azimuthal rays denote either side of the Kulite Array. The positive 90° position is approximately the top side of the tunnel. From the PSD, the second-mode instability is detected between 200 and 350 kHz by all of the sensors. Most sensors were observed to have similar magnitudes. The PCB sensor at the -30° ray from the Kulite Array detected the second mode with an amplitude nearly an order of magnitude higher than the rest of the sensors. It is unclear why this position experiences larger disturbances, but the random roughness of TSP could be a possible explanation. A bad factory calibration could also skew the magnitude of the instability. An in-house PCB calibration technique is currently being investigated by Berridge [64]. RMS values were computed for the other sensors that were similar in power. Integrating over 200-350 kHz, the highest percent difference of these values to the average was 43%. Table A.1 shows the percent difference of each sensor for this test.

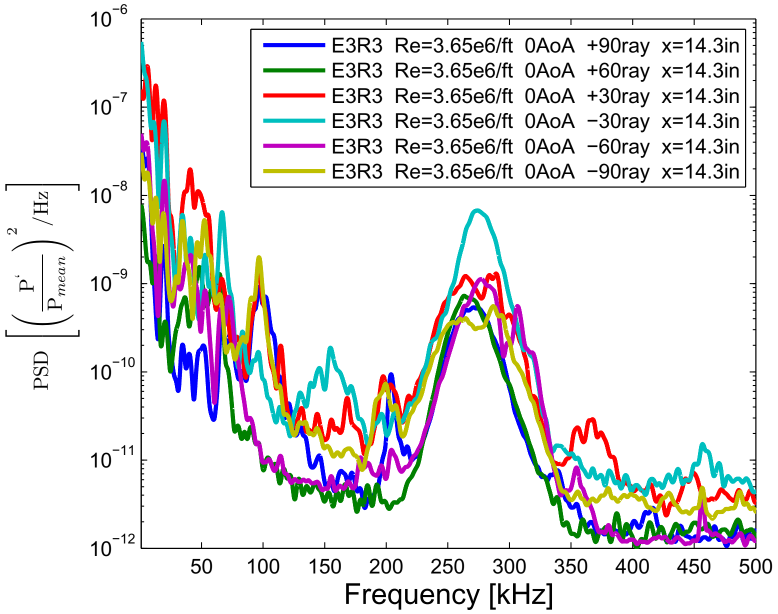

Figure 6.9. PSD of quiet spectra for run E3R3, all traces from PCB sensors at $x = 14.3$-in. using the Ward Cone.

6.4 Second-mode Amplitudes

The second-mode disturbances detected in the 0° AoA tests were integrated under each peak to approximate the magnitude of the fluctuations. The frequencies of integration were chosen based on where the spectra showed a power content above the noise levels. Figure 6.10 shows all runs that detected the second-mode instability. All noisy runs showed turbulent spectra at the furthest aft PCB sensor. The second-mode amplitudes under quiet flow were at least an order of magnitude lower than under noisy flow. Figure 6.11 shows the same second-mode amplitudes as a function of Re_x. Under noisy flow, the spectra of the second mode appears to become broad around $Re_x = 3.00 \times 10^6$. Turbulent spectra is observed after this Reynolds number.

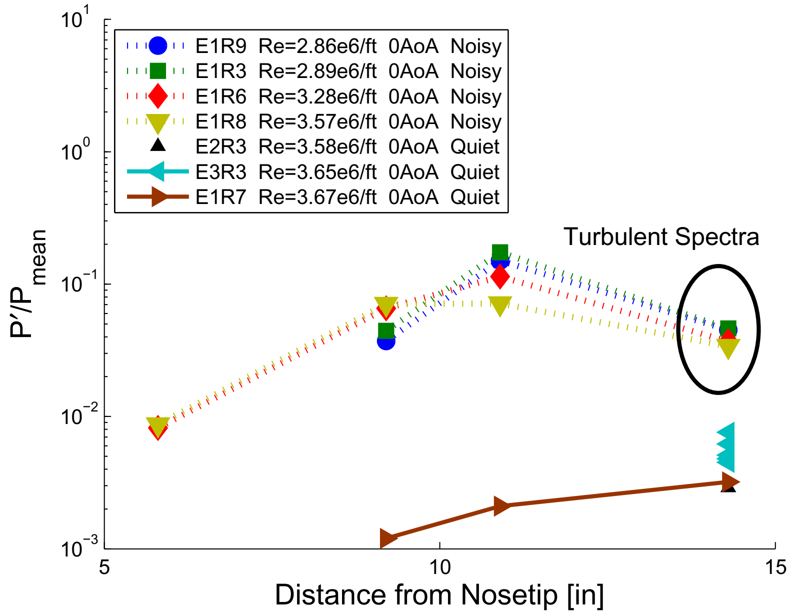

Figure 6.10. Second-mode amplitudes as a function of distance from nosetip.

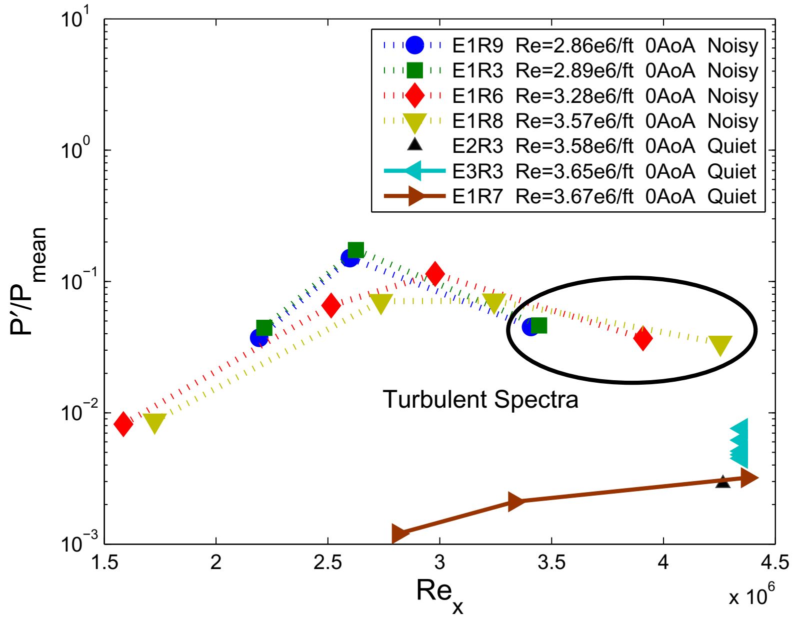

Figure 6.11. Second-mode amplitudes as a function of Reynolds number with characteristic length x.

6.5 Pate's Correlation

The transition location was estimated for the noisy runs (E1R3, E1R6, and E1R8) at zero angle of attack and compared to Pate's Correlation for predicting transition on a sharp slender cone. Pate developed an algorithm to determine the end of transition on sharp slender cones at zero angle of attack [65]. The correlation is based on tunnel characteristics such as: tunnel-wall skin-friction coefficient ($C_{F_{II}}$), tunnel-wall turbulent boundary-layer displacement thickness (δ^*), test-section circumference (C), and aerodynamic-noise-transition correlation size parameter ($\bar{c}$). The size parameter considers a reference test-section circumference of a 12 × 12-in tunnel, denoted as c_1. The transition Reynolds number is calculated as:

$$(Re_t)_{cone} = \frac{48.5\ (C_{F_{II}})^{-1.40}\ (\bar{c})}{\sqrt{\delta^*/C}} \tag{6.1}$$

$$\bar{c} = 0.8 + 0.2\left(\frac{c_1}{C}\right) \quad when \quad \frac{c_1}{C} < 1.0$$

$$\bar{c} = 1.0 \quad when \quad \frac{c_1}{C} > 1.0$$

The skin-friction coefficent was calculated using the method of Van Driest II with a wall temperature of 540 °R. The circumference of the Boeing/AFOSR Mach-6 Quiet Tunnel is 9.5 inches in diameter. The displacement thickness was computed from Maxwell's correlation based on the model positioned 85 inches from the throat of the nozzle. The transition location is then found by dividing Re_t by the unit Reynolds number at the surface of an inviscid cone.

For the three tests, the location of transition was estimated to be between the PCB sensors at $x = 10.9$-in and $x = 14.3$-in. The further upstream PCB sensor showed low noise, where the second mode was still observed. For this reason the boundary layer is assumed to still be laminar. The PCB sensor further downstream showed broadband noise and is assumed to be turbulent.

Pate's correlation was compared to the approximate transition locations of the experimental results in Figure 6.12. The uncertainty bars mark the PCB sensor locations. The aft PCB sensor determined that transition has occurred while the upstream PCB sensor showed laminar spectra. The transition location is assumed to be between these two sensors, but a definitive location cannot be determined.

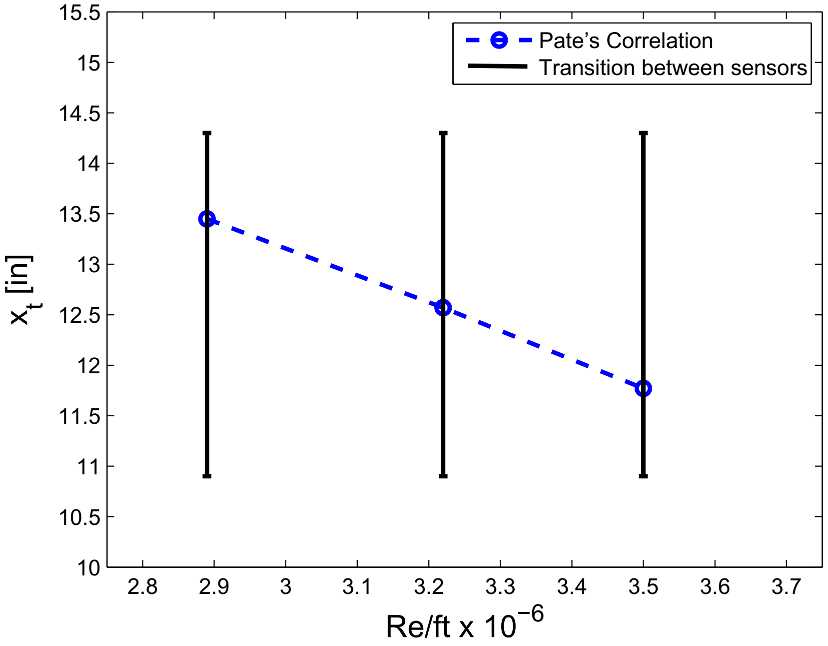

Figure 6.12. Comparison of Pate's Correlation with experimental results from E1R3, E1R6, and E1R8. Uncertainty bar edges at pressure sensor positions.

7. STATIONARY CROSSFLOW INSTABILITY

TSP was used to detect stationary crossflow waves on each cone model. The images presented in this section are ‘smooth surface’ models where the cone was sprayed with a TSP layer, but no roughness elements were added. A measurement of the TSP layer’s smoothness for each entry was compiled in Table B.1. The stationary crossflow waves were compared by varying Reynolds numbers, angles of attack, and azimuthal rays. Repeatability was also compared across entries.

7.1 Defining Stationary Crossflow Vortices

Most TSP images were found to have streaks of high heat transfer crossing over the cone. Vortices cause localized mixing that promote additional heat transfer to the surface. The streaks are believed to be vortices from the stationary crossflow mode. As mentioned previously, stationary waves are introduced from localized roughness. To determine if the vortices are stationary waves, the windward ray is rotated and the positions of the streaks roll with the cone. This determines if the streaks are body fixed from roughness on the cone and not from freestream disturbances. The author did not have data at small rotations to show a conclusive result, but Ward [46] was able to show the vortices are, in fact, body fixed through his experiments.

7.2 Reynolds Number Comparison

7.2.1 90° Ray Results

Three Reynolds numbers were tested for a smooth cone at 4° AoA. Figures 7.1, 7.2, and 7.3 show TSP images where the Kulite array was near the 90° ray from windward. Streaks were observed toward the leeside of the cone for all Reynolds numbers in the upper side of the images. The red line near the center of the image denotes the ray with multiple sensors, referred to as the sensor ray.

An azimuthal profile of the TSP images was taken at $x = 12.1$-in to compare the heat flux for each Reynolds number, shown on Figure 7.4. The heat flux was divided by the theoretical laminar values for a 7° half-angle cone at zero angle of attack at the same Reynolds numbers. Similar heat transfer was found from the wind to the 110° ray. To the lee of this ray, however, heat-flux peaks are observed and as the Reynolds number is increased the heat flux from these streaks increase. At $x = 12.1$-in heat-flux peaks spaced 4° to 6° apart are seen in the azimuthal profile from the 110° to 135° ray. These peaks are the heat transfer streaks from the stationary crossflow vortices. Figure 7.5 shows azimuthal profiles taken at $x = 13.0$-in where these peaks in heat transfer have moved closer to the lee ray. The magnitude of the heat flux at the highest Reynolds number increased by a factor of 2.

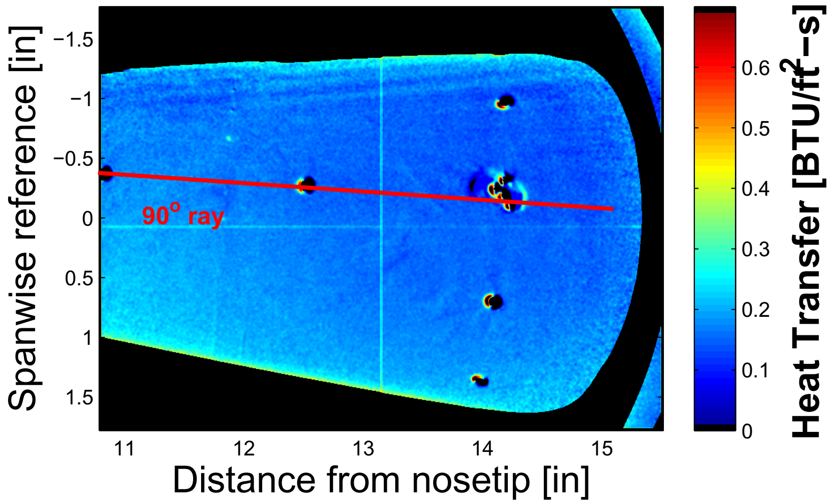

Figure 7.1. Heat transfer contour of E4R3. 4°AoA, quiet flow, smooth surface, Kulites near the 90° ray. $Re = 2.81{\times}10^6$/ft, $P_o = 118.8$ psia, $T_o = 295.7$°F, $T_w = 86.8$°F.

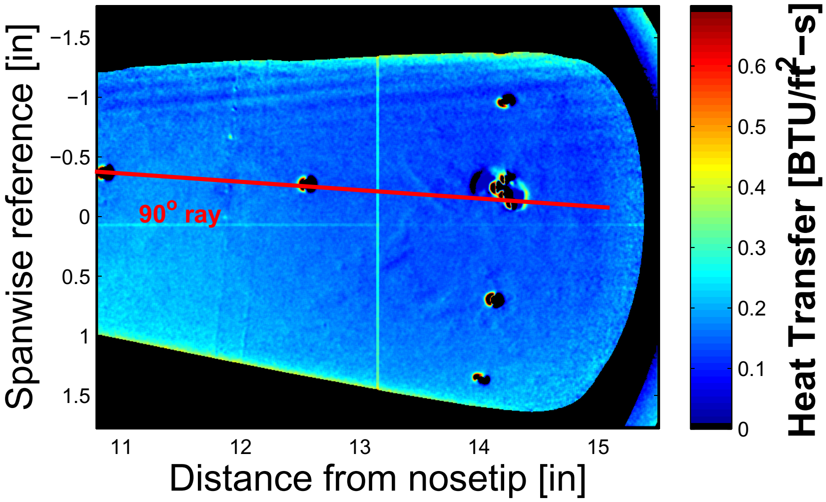

Figure 7.2. Heat transfer contour of E4R2. 4°AoA, quiet flow, smooth surface, Kulites near the 90° ray. $Re = 3.29{\times}10^6$/ft, $P_o = 139.9$ psia, $T_o = 297.7$°F, $T_w = 82.3$°F.

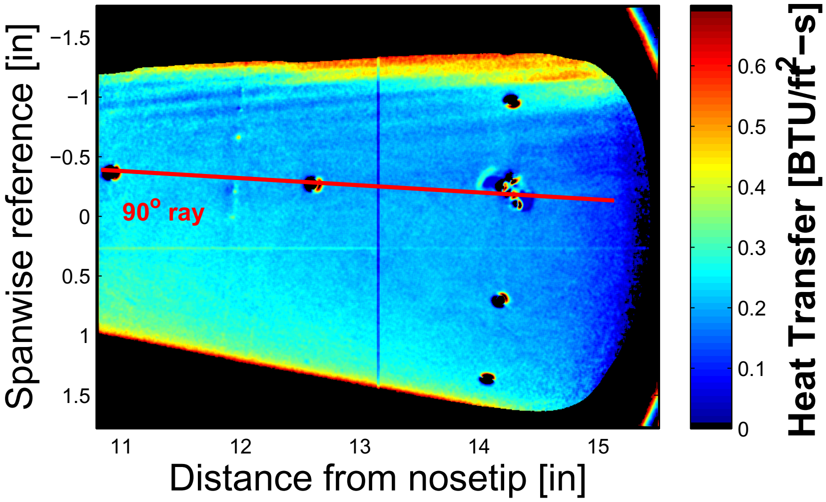

Figure 7.3. Heat transfer contour of E4R1. 4°AoA, quiet flow, smooth surface, Kulites near the 90° ray. $Re = 3.66{\times}10^6$/ft, $P_o = 156.8$ psia, $T_o = 301.7$°F, $T_w = 74.6$°F.

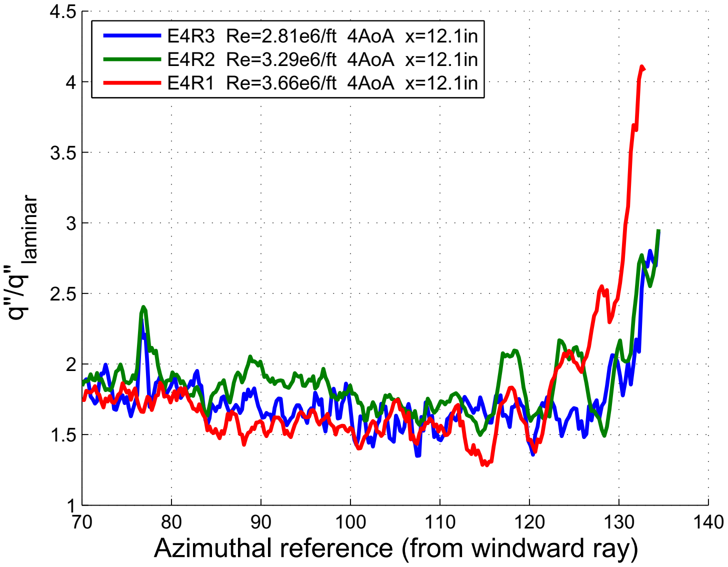

Figure 7.4. Spanwise heat transfer profile of E4R3, E4R2, and E4R1 at $x = 12.1$-in, 4°AoA, quiet flow, smooth surface.

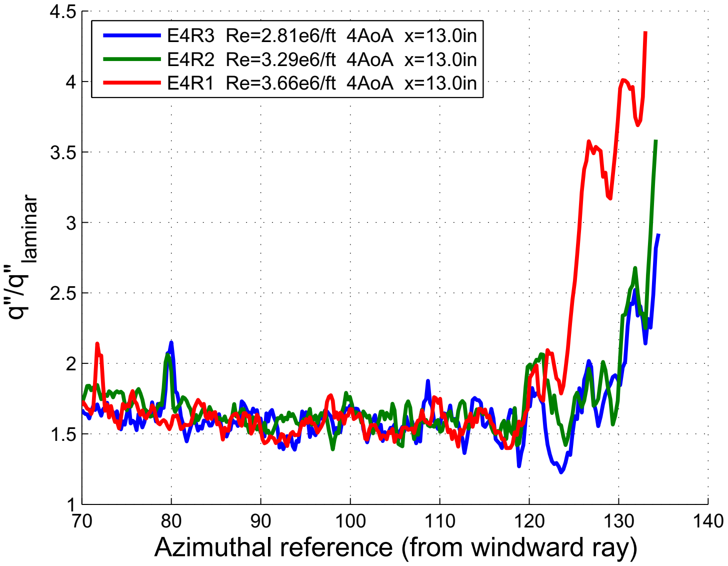

Figure 7.5. Spanwise heat transfer profile of E4R3, E4R2, and E4R1 at $x = 13.0$-in, 4°AoA, quiet flow, smooth surface.

To determine if this large increase in heat flux is attributed to the onset of transition, the PCB sensor at the 150° ray at $x = 14.3$-in was plotted for the three Reynolds number cases, shown in Figure 7.6. As the Reynolds number increases the noise levels increase across all frequencies. At the highest Reynolds number the spectra is relatively flat over all frequencies, indicating turbulence.

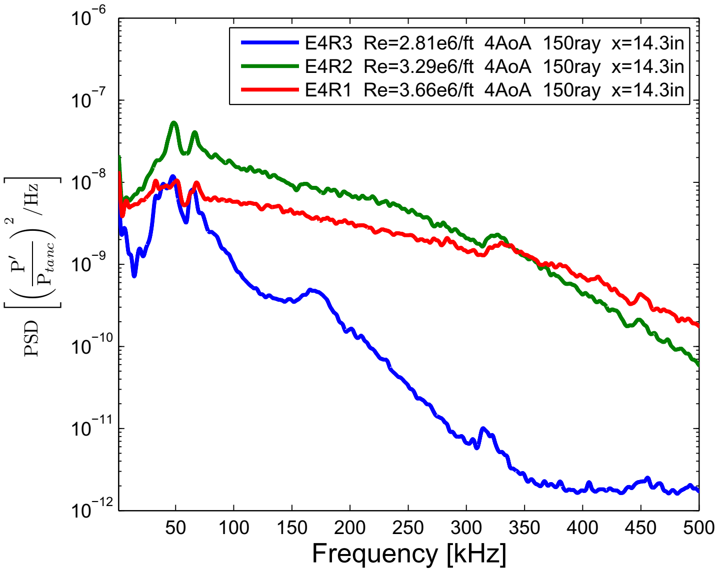

Figure 7.6. PSD of E4R3, E4R2, and E4R1. 4°AoA, Quiet flow, smooth surface, PCB sensor at the 150° ray.

7.2.2 120° Ray Results

Spatial resolution diminishes near the edges of the cone due to the glancing angle for the image. To study the stationary mode at rays closer to the lee, the model was rotated 30° toward the leeside with respect to the sting and the whole assembly (sting and model) was then rotated 30° so the image was centered near the 120° ray. This effectively moves the sensor positions 30° to the lee. A new windward ray is then referenced as the 0° ray. Figures 7.7 and 7.8 reveal that the streaks lie between the 120° and 160° rays. A clear pattern of streaks can be seen for the higher Reynolds number. The higher Reynolds number test also shows the strength of the vortices decaying after reaching a maximum. The PCB sensor on the 150° ray downstream of the growth and decay of these stationary waves show turbulent spectra. After the decay in amplitude of the stationary waves it appears the breakdown to turbulence.

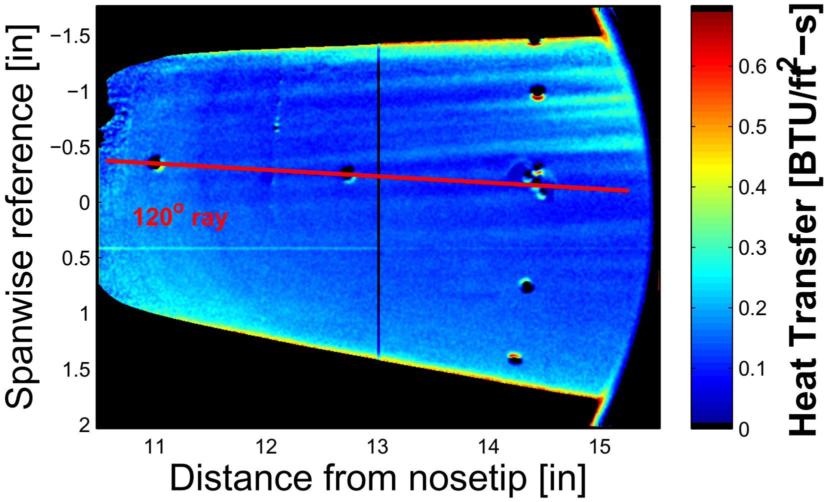

Figure 7.7. Heat transfer contour of E5R5. 4°AoA, quiet flow, smooth surface, Kulites near the 120° ray. $Re = 3.26{\times}10^6$/ft, $P_o = 140.0$ psia, $T_o = 302.3$°F, $T_w = 90.3$°F.

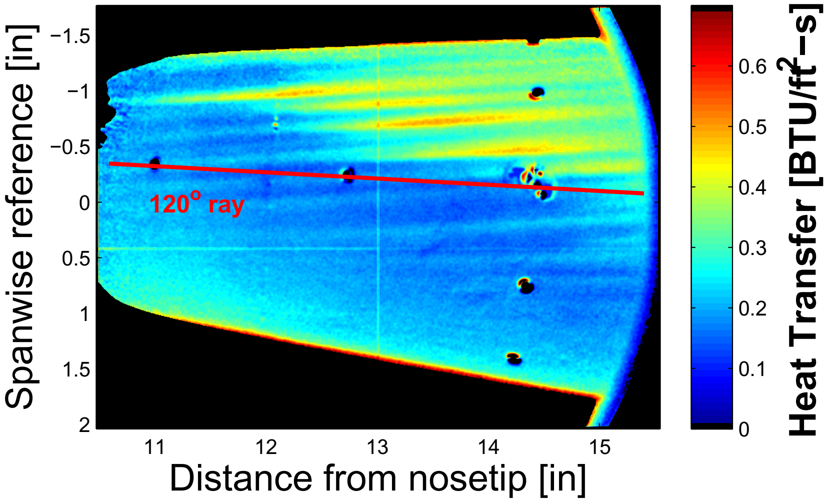

Figure 7.8. Heat transfer contour of E5R6. 4°AoA, quiet flow, smooth surface, Kulites near the 120° ray. $Re = 3.71{\times}10^6$/ft, $P_o = 158.0$ psia, $T_o = 299.4$°F, $T_w = 95.8$°F.

Figure 7.9 shows the azimuthal profile at $x = 12.0$-in. Heat-flux peaks are clearly present at the higher Reynolds number. The peak near the 146° ray increases by a factor of 4 from $Re = 3.26{\times}10^6$/ft to $Re = 3.71{\times}10^6$/ft. Figure 7.10 shows a azimuthal profile at $x = 13.0$-in, where vortex streaks are observed for both Reynolds numbers. The higher Reynolds number test shows streaks near the same rays as the lower Reynolds number. The amplitudes from the lower to higher Reynolds number increases by a factor of 4 near the 140° to 150° rays. The average peak-to-peak spacing is approximately 8° for the higher Reynolds number case.

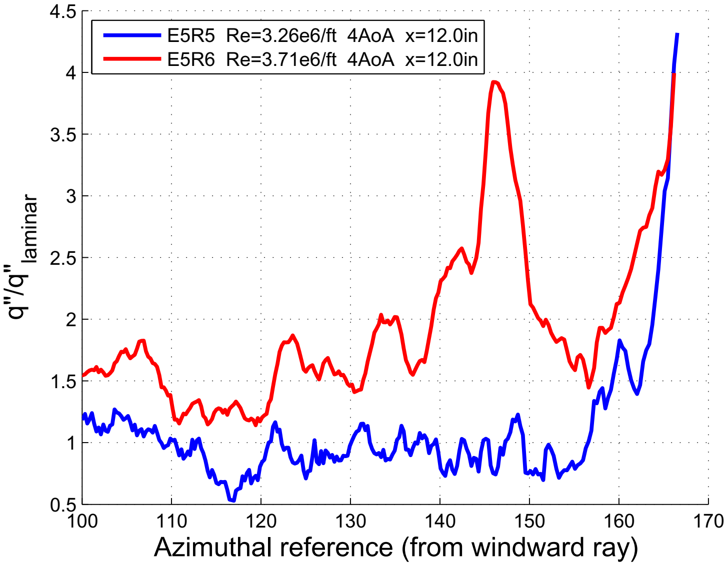

Figure 7.9. Spanwise heat transfer profile of E5R5 and E5R6 at $x =$ 12.0-in, 4°AoA, quiet flow, smooth surface.

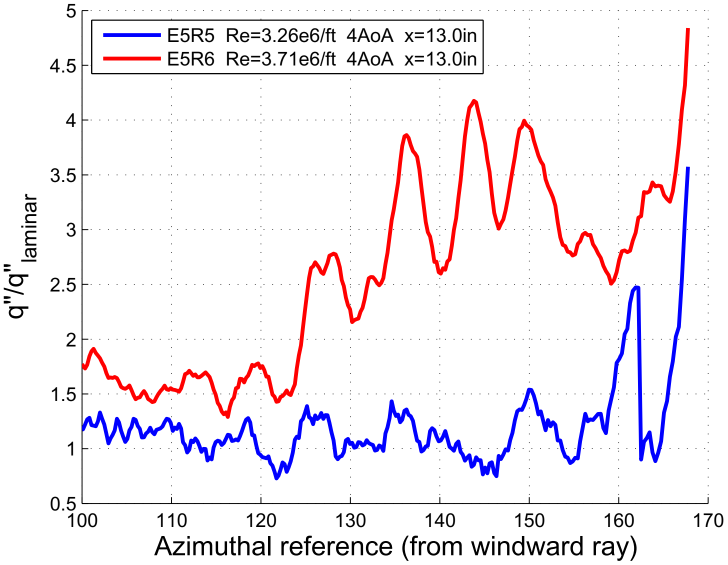

Figure 7.10. Spanwise heat transfer profile of E5R5 and E5R6 at $x = 13.0$-in, 4°AoA, quiet flow, smooth surface.

7.3 Angle of Attack Comparison

7.3.1 Smooth Surface Results

Three angles of attack were imaged for a smooth cone with the Kulite array at the 90° ray, shown in Figures 7.11, 7.12, and 7.13. As the angle of attack was increased, the streaks became visible to the lee of the 90° ray. The pressure gradient increases with angle of attack. This results in a larger crossflow component and the stationary vortices grow in amplitude. Increased heat transfer can be seen in Figure 7.13. A low amount of TSP was sprayed near $x = 10.5$-in for entry 6 so the variation in heat flux in this region of Figures 7.11, 7.12, and 7.13 are not physical.

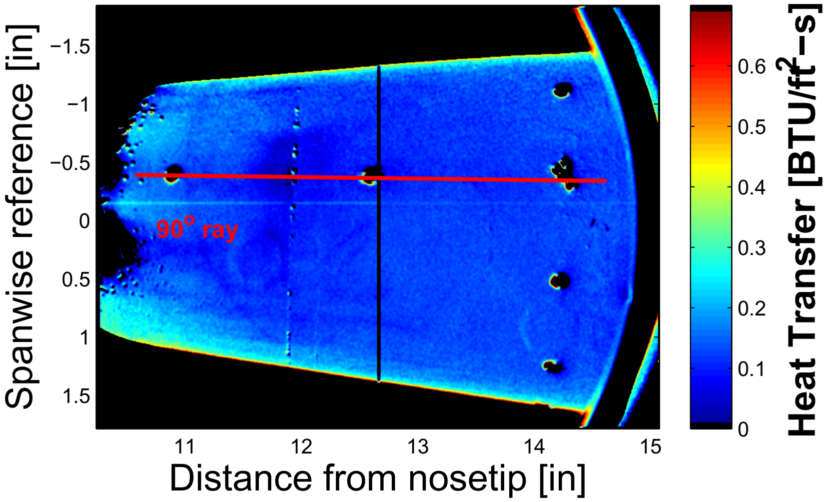

Figure 7.11. Heat transfer contour of E6R12. 2°AoA, quiet flow, smooth surface, Kulites near the 90° ray. $Re = 3.64 \times 10^6$/ft, P_o = 155.7 psia, T_o = 304.9°F, T_w = 79.8°F.

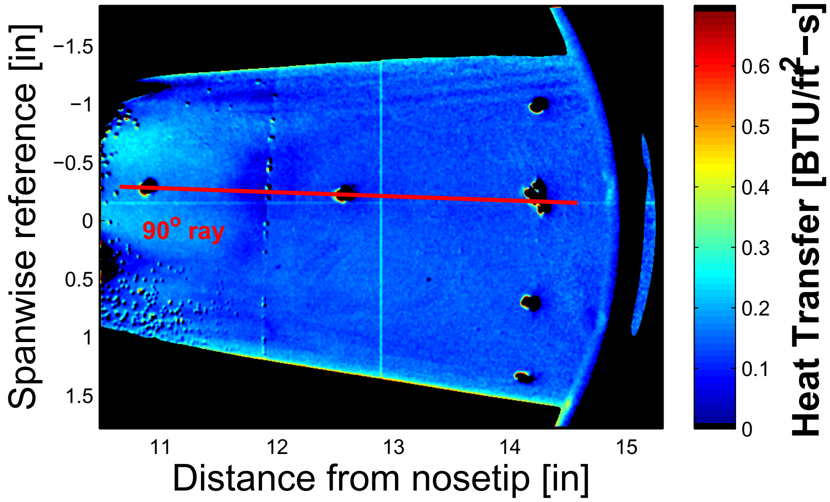

Figure 7.12. Heat transfer contour of E6R31. 3°AoA, quiet flow, smooth surface, Kulites near the 90° ray. $Re = 3.58{\times}10^6$/ft, $P_o =$ 157.2 psia, $T_o = 313.1$°F, $T_w = 86.7$°F.

An azimuthal profile was computed for the three cases: E6R12, E6R31, and E5R1, at $x = 13.5$-in to compare the heat transfer as a function of angle of attack, shown in Figure 7.14. The 2° and 3° AoA cases show approximately the same heat transfer as the theoretical laminar case at zero angle of attack, except to the lee of the 145° ray. Near the edge of the cone the intensity of light being emitted is low due to the glancing view, so heat flux values near the edge are not real. At 4° AoA heat-flux peaks are clearly seen. Since the image was centered near the 90° ray, heat flux information to the lee of the 140° ray suffers from low spatial resolution. No other tests had matching conditions to compare the three angles of attack at higher rays for smooth surface cases.

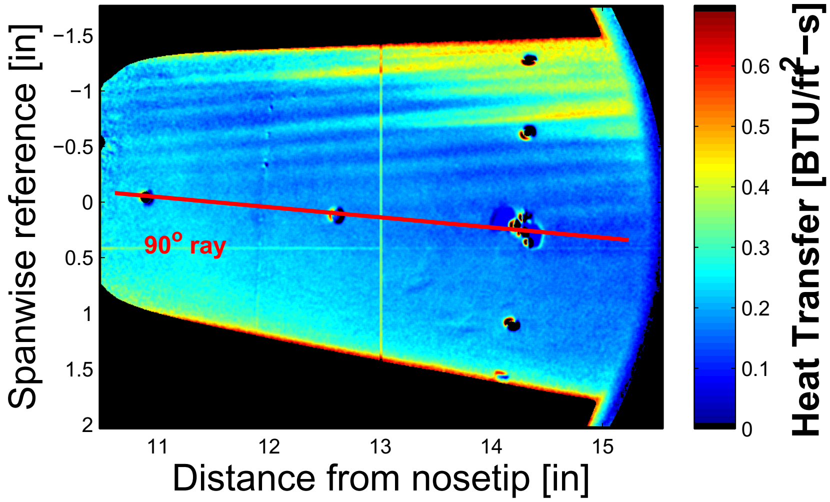

Figure 7.13. Heat transfer contour of E5R1. 4°AoA, quiet flow, smooth surface, Kulites near the 90° ray. $Re = 3.69\times10^6$/ft, $P_o =$ 157.6 psia, $T_o = 300.3$°F, $T_w = 90.4$°F.

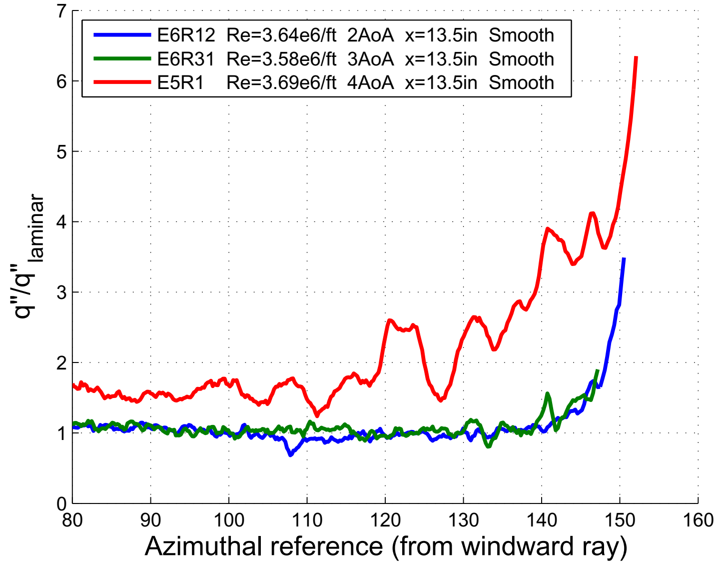

Figure 7.14. Spanwise heat transfer profile of E6R12, E6R31, and E5R1 at $x = 13.5$-in, quiet flow, smooth surface.

7.3.2 Torlon-insert Roughness Results

Tests imaging closer to the lee are shown in Figures 7.15, 7.16, and 7.17. These tests were conducted with the Torlon insert installed. The dimples indented into the Torlon create a discrete roughness used to excite stationary waves. The effects of the roughness are discussed in a later section. For this section, the results are presented to show the differences in angle of attack.

No clear streaks are observed for the heat transfer contour at 2° AoA, but at 3° and 4° AoA vortices are seen to the lee of the 120° ray. The rapid growth of the vortices is observed at the higher angles of attack. The onset of this region is located near $x = 12.5$-in for 3° AoA near the 150° ray and further upstream than could be imaged for 4° AoA near the same ray.

Azimuthal heat transfer profiles were taken for the three cases at $x = 11.5$-in and $x = 13.5$-in, shown in Figures 7.18 and 7.19 respectively. At $x = 11.5$-in a large peak in heat transfer was found near the 148° ray for the 4° AoA run. Further downstream at $x = 13.5$-in the streak near the 148° ray decays and stationary waves for the 3° AoA run grow larger than the 4° AoA run to the lee of the 145° ray. The cause of this appears to be due to the stationary waves forming further upstream and then breaking down at $x = 13.5$-in for the 4° AoA run. The azimuthal ray may not be able to resolve the exact location of the streaks to the lee of 150° ray, again, due to the edge of the cone.

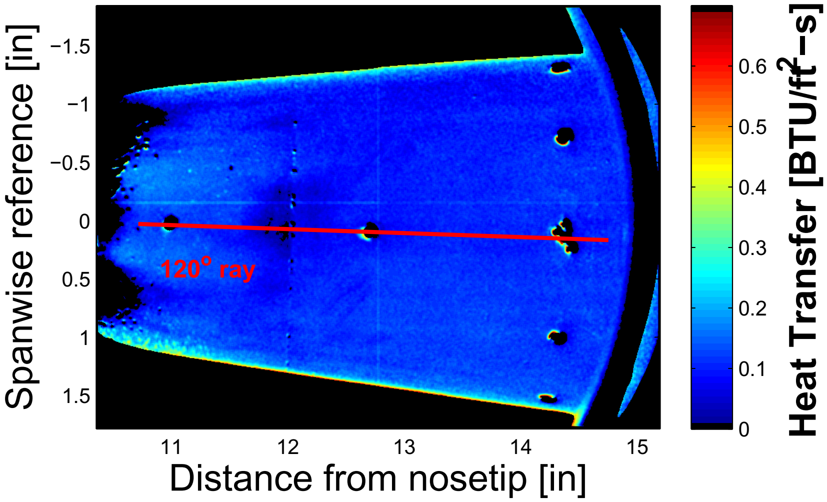

Figure 7.15. Heat transfer contour of E6R17. 2°AoA, quiet flow, Torlon insert, Kulites near the 120° ray. $Re = 3.60 \times 10^6$/ft, $P_o =$ 156.8 psia, $T_o = 309.3$°F, $T_w = 79.8$°F.

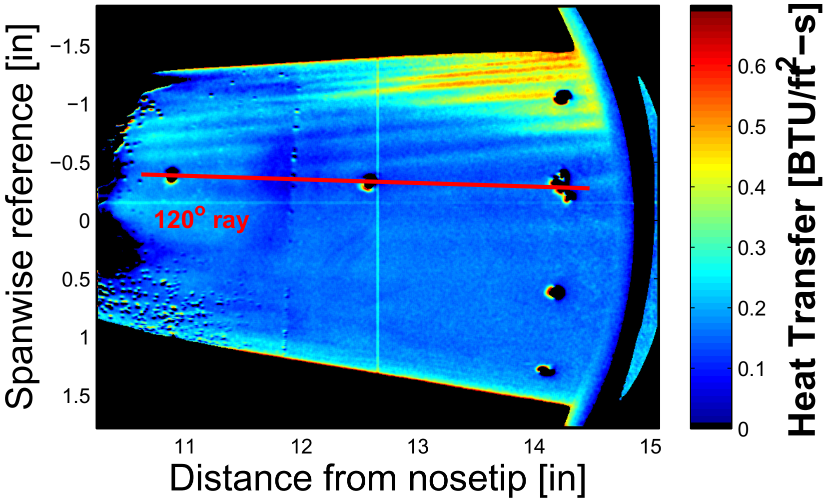

Figure 7.16. Heat transfer contour of E6R39. 3°AoA, quiet flow, Torlon insert, Kulites near the 120° ray. $Re = 3.61 \times 10^6$/ft, $P_o =$ 157.0 psia, $T_o = 308.1$°F, $T_w = 86.7$°F.

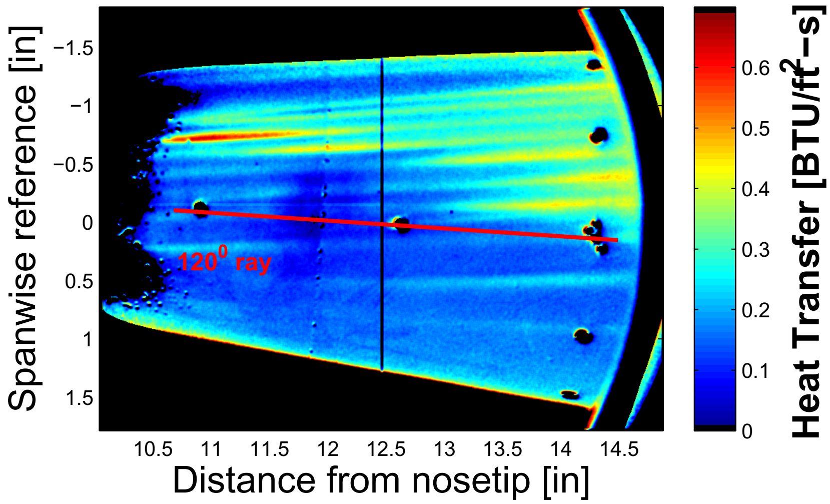

Figure 7.17. Heat transfer contour of E6R4. 4°AoA, quiet flow, Torlon insert, Kulites near the 120° ray. $Re = 3.62{\times}10^6$/ft, $P_o = 156.8$ psia, $T_o = 306.2$°F, $T_w = 90.4$°F.

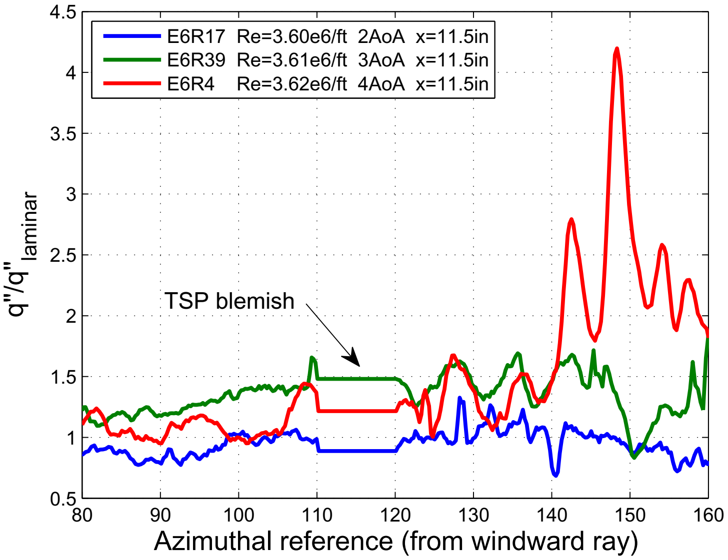

Figure 7.18. Spanwise heat transfer profile of E6R12, E6R31, and E5R1 at $x = 11.5$-in, quiet flow, Torlon insert.

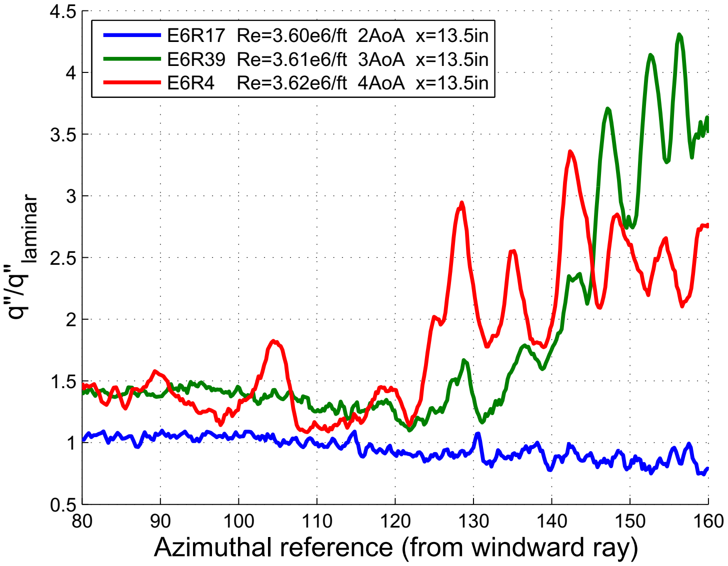

Figure 7.19. Spanwise heat transfer profile of E6R12, E6R31, and E5R1 at $x = 13.5$-in, quiet flow, Torlon insert.

The growth and breakdown of the stationary vortices were analyzed by taking axial heat transfer profiles along vortex streaks. The vortices analyzed between the 120° and 180° rays of E6R4 are shown in Figure 7.20. The axial profiles are shown in Figure 7.21. The profiles were averaged over each pixel in the spanwise direction. The number of pixels averaged depend on the width of a vortex streak, where the edges were determined when the heat flux began to show constant values below the peak value. An example of a profile that was averaged is shown in Figure 7.22, where four spanwise profiles was computed at distances along Vortex 2. The black line denotes the region that was averaged. Vortex 2 and 3 show a rapid increase in heat flux and then a decrease to a constant value. The PSD of the PCB at the 150° ray, just aft of the decay of the stationary-wave amplitude, was found to have turbulent spectra. This is most likely the result of the vortices breaking down. Vortices 4, 5, and 6 begin increasing in heat flux further downstream near $x = 12.0$-in, but their development was only imaged to $x = 14.5$-in.

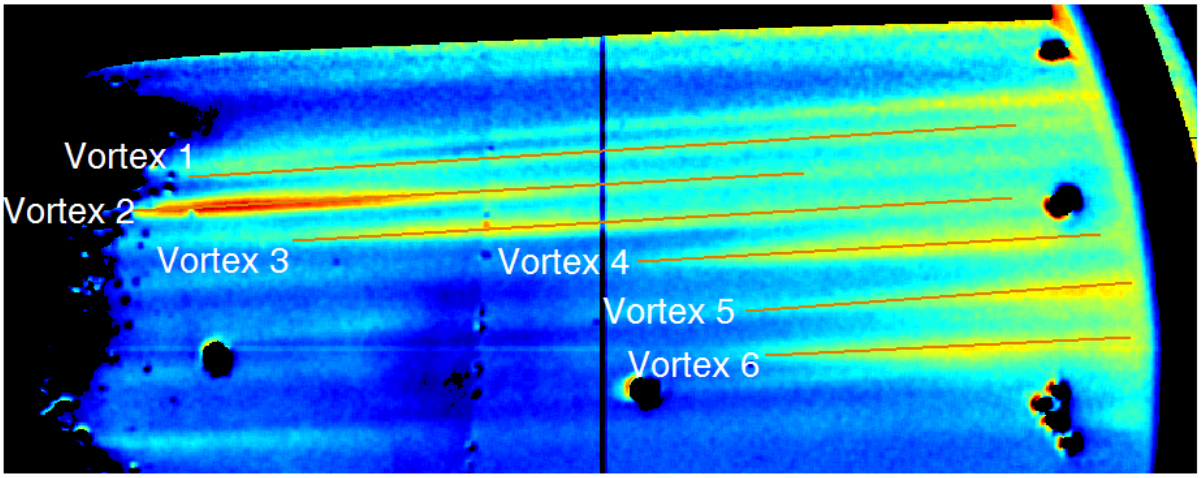

Figure 7.20. Heat transfer contour of E6R4 with vortex labels, quiet flow, Torlon insert.

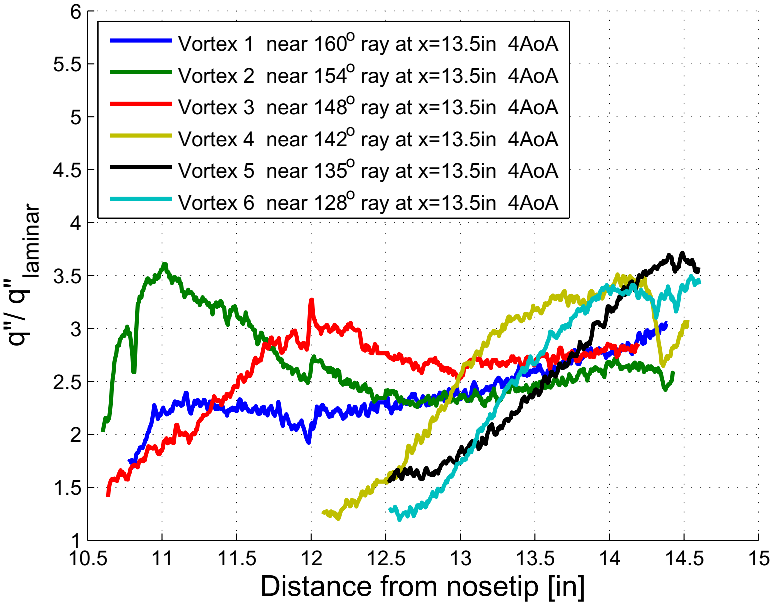

Figure 7.21. Axial heat transfer profiles of vortices for E6R4, quiet flow, Torlon insert.

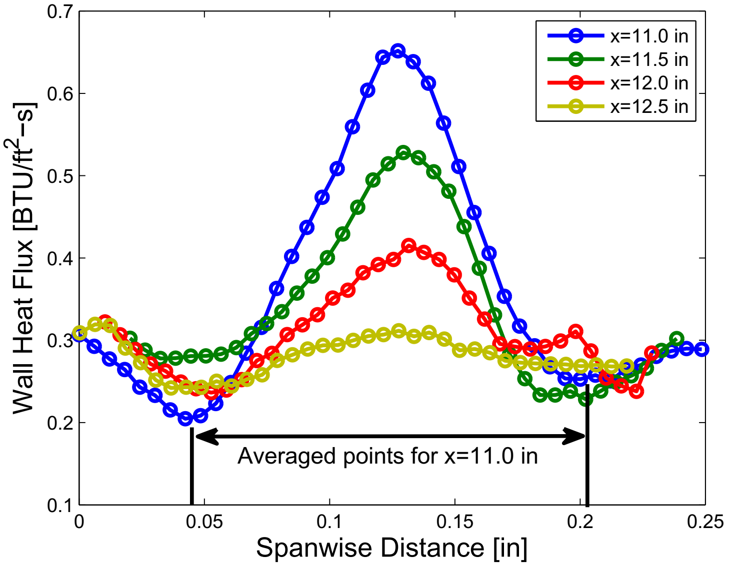

Figure 7.22. Spanwise profiles along Vortex 2.

7.4 Stationary Waves under Noisy Flow

Stationary vortices were apparently observed under noisy flow. Figure 7.23 shows the heat transfer contour of E3R7. The plot is scaled down $(0 - 0.5\ \frac{BTU}{ft^2-s})$ to observe the vortices to the lee of the 90° ray. The transition front is seen towards the lee side by the sudden change in heat flux. Two streaks are observed from $x = 11.0$-in at the 100° ray to the PCB sensor at $x = 14.3$-in at the 120° ray. These streaks look like stationary crossflow waves. The streaks can be seen before and after the transition front. No other streaks of this kind have been found while testing under noisy flow conditions.

7.5 Repeatability between Entries

For each entry, the model being tested was given a new TSP layer in order to obtain the highest signal from the luminescent paint. However, with a new paint layer, the distributed roughness changes across the model. Repeatability between

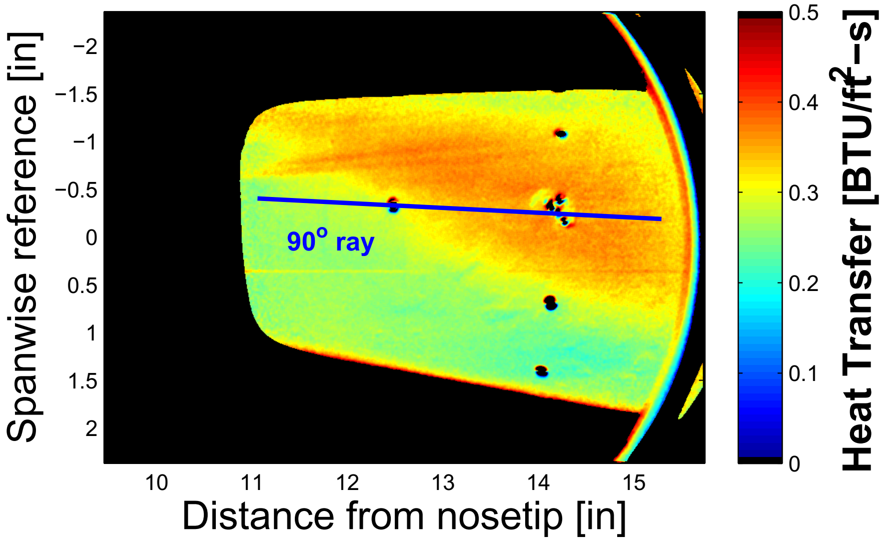

Figure 7.23. Heat transfer contour of E3R7. 4°AoA, noisy flow, smooth surface, Kulites near the 90° ray. $Re = 2.89\times10^6$/ft, $P_o =$ 114.7 psia, $T_o =$ 301.2°F, $T_w =$ 83.4°F.

entries was measured to determine if the distributed roughness had an effect. Entries 2, 3, 4, and 5 were compared at the matching conditions: 4° AoA, quiet flow, no applied roughness, and Reynolds number of approximately 3.65×10^6/ft.

Heat transfer contours are shown in Figures 7.24, 7.25, 7.26, and 7.27, for entries 2, 3, 4, and 5, respectively, for smooth Crossflow and Ward cones at 4° AoA under quiet flow. The RMS roughness over the surface of the TSP is compiled in Table B.1 for each entry. The images were centered near the 120° ray with the exception of entry 4 where the highest azimuthal position imaged was near the 90° ray. Azimuthal rays to the lee of the 120° ray were then difficult to compare. A rapid increase in heat flux is seen on all entries by $x =$ 13.0-in. The Crossflow cone was used for entry 2 so it is possible the difference in the radius of the nosetip could effect the vortex development along the cone.

An azimuthal heat transfer profile was taken at $x = 13.5$-in for each entry, shown in Figure 7.28. Entries 2, 3, and 5 show vortices near the same azimuthal rays, but differ in amplitude. The differences in heat transfer across each vortex suggests the random distributed roughness does effect the repeatability between entries. It is therefore recommended that TSP be applied only once. Concerns of TSP photodegradation were the reason for repainting models, but this issue is currently being investigated. Repeatability may also be possible using discrete roughnesses. Ward [46] changed the random roughness of the TSP, but kept the same discrete roughness elements. Heat transfer contours showed the stationary vortices were at the same location for each TSP roughness. Ward summarizes that the discrete roughness elements dominate the excitation of stationary vortices over the distributed roughness of the TSP.

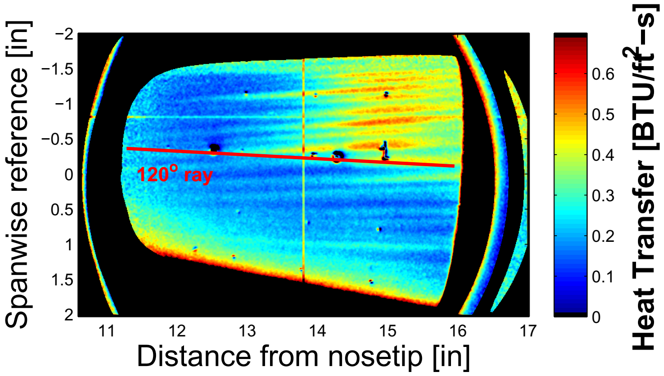

Figure 7.24. Heat transfer contour of E2R22. 4°AoA, quiet flow, smooth surface, PCBs at the 120° ray. $Re = 3.64{\times}10^6$/ft, $P_o = 158.2$ psia, $T_o = 308.3$°F, $T_w = 85.1$°F.

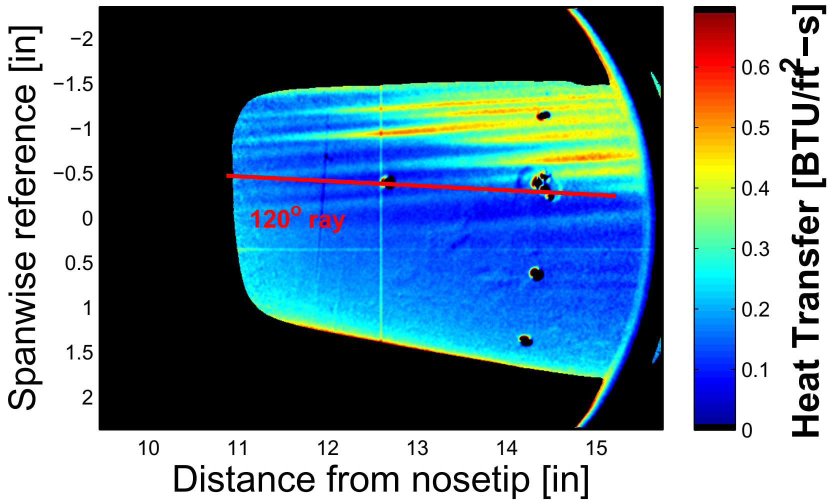

Figure 7.25. Heat transfer contour of E3R16. 4°AoA, quiet flow, smooth surface, Kulites near the 120° ray. $Re = 3.63{\times}10^6$/ft, $P_o =$ 156.1 psia, $T_o = 302.6°$F, $T_w = 94.6°$F.

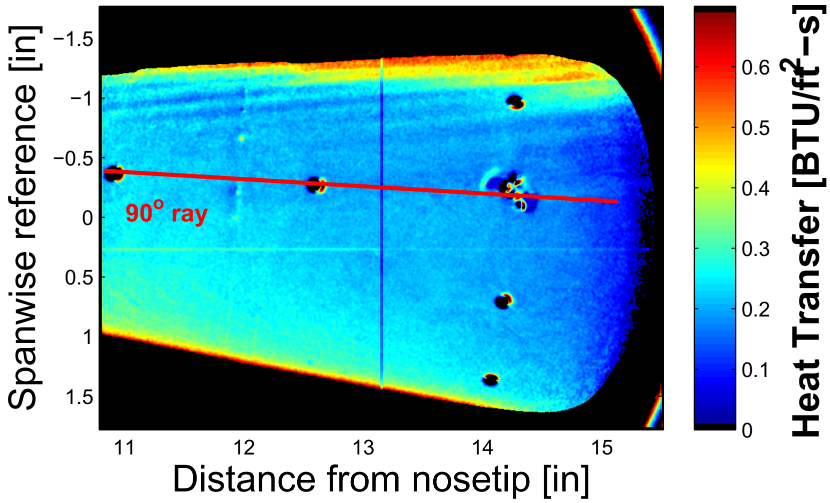

Figure 7.26. Heat transfer contour of E4R1. 4°AoA, quiet flow, smooth surface, Kulites near the 90° ray. $Re = 3.65{\times}10^6$/ft, $P_o =$ 156.8 psia, $T_o = 301.7°$F, $T_w = 74.6°$F.

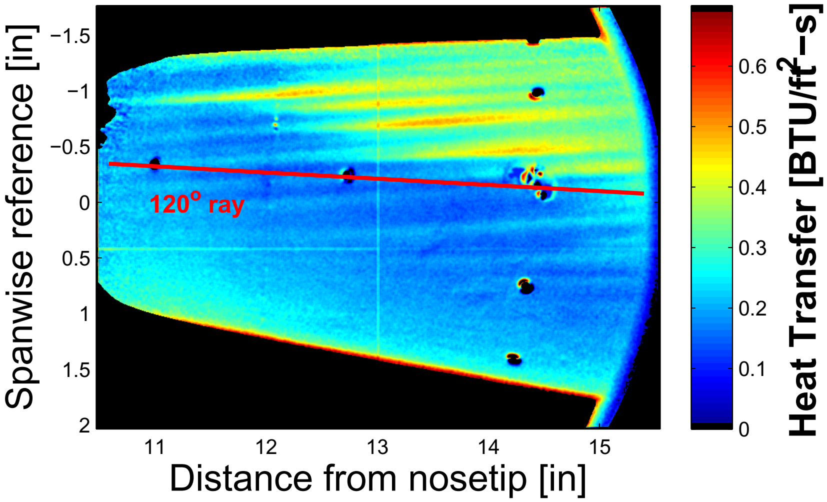

Figure 7.27. Heat transfer contour of E5R6. 4°AoA, quiet flow, smooth surface, Kulites near the 120° ray. $Re = 3.71{\times}10^6$/ft, $P_o =$ 158.0 psia, $T_o = 299.4$°F, $T_w = 90.4$°F.

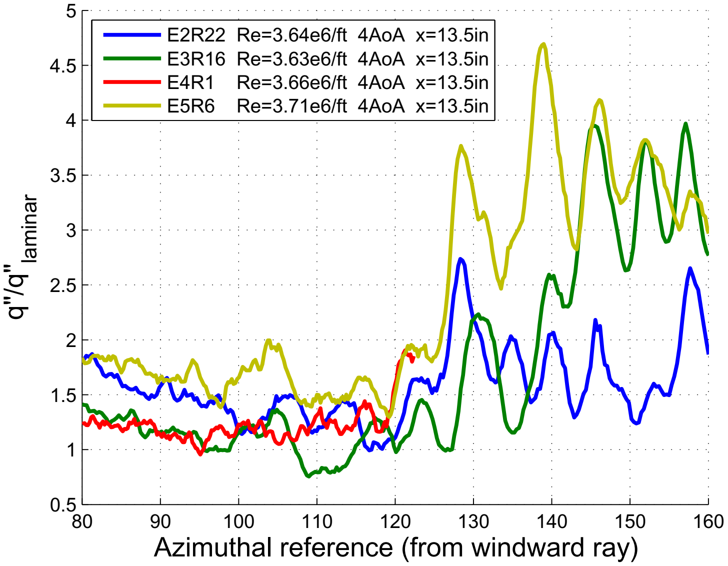

Figure 7.28. Spanwise heat transfer profile of entries 2, 3, 4, and 5 at $x = 13.5$-in, quiet flow, smooth surface.

8. TRAVELING CROSSFLOW INSTABILITY

Experiments conducted by the author detected instabilities between 20-80 kHz for a 7° half-angle cone at low angles of attack at Mach 6. Calculations were made to analyze the wave speed and direction of wave propagation of these disturbances, which appear to be traveling crossflow waves. The instabilities were detected by both PCB and Kulite sensors over a range of Reynolds numbers for quiet and noisy tunnel configurations. Angle of attack and sensor comparisons were also analyzed.

8.1 Wave Properties

Instability wave properties can be determined with measurements from three sensors in near proximity to each other, to resolve the angle and phase speed of the waves. An axial and circumferential surface coordinate system was transformed into a two-dimensional plane for small regions of surface curvature. The coordinate system was then transformed by rotating the axes by the wave angle (Φ) in the direction of the wave propagation, shown in Figure 8.1.

The Kulite sensor locations are transformed using Equations 8.1 and 8.2:

$$x' = xcos\Phi + ysin\Phi \tag{8.1}$$

$$y' = -xsin\Phi + ycos\Phi \tag{8.2}$$

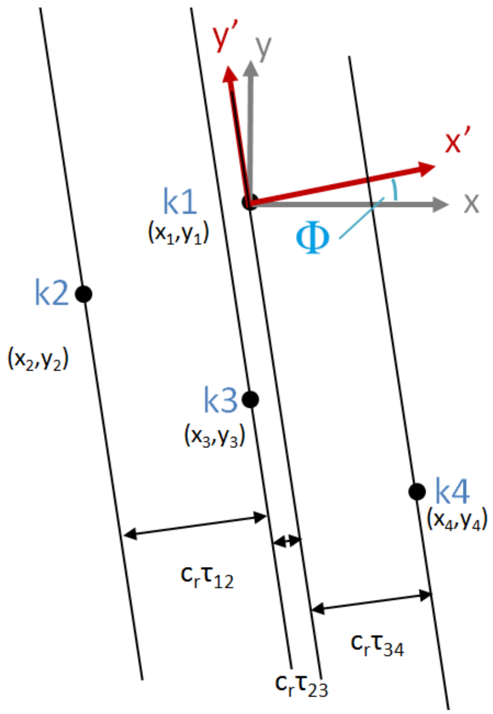

(a) Original coordinate system (x,y)

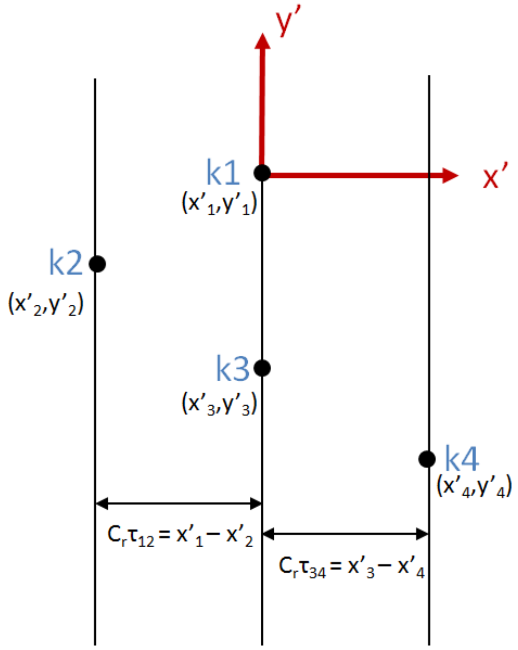

(b) Transformed coordinate system (x′,y′)

Figure 8.1. Orientation of coordinate systems for cross-spectral analysis. Drawing from Ref [15] is modified for Kulite Array 2 geometry.

The distance between the sensors in the rotated coordinate system can then be related to the time delay of a particular phase (τ) and its phase speed (c_r), shown in Equation 8.3:

$$c_r \tau_{ab} = x'_b - x'_a \tag{8.3}$$

where a and b are the sensor positions to be analyzed. Three independent equations can be formed from Equation 8.3 pairing between any of the four sensors, where a, b, c, and d are any of the sensor positions, such that $a \neq b$ and $c \neq d$. Equations 8.1 and 8.2 can be substituted into each of the three equations to solve for the wave angle, shown in Equation 8.4:

$$tan\Phi = \frac{\tau_{cd}(x_b - x_a) - \tau_{ab}(x_d - x_c)}{\tau_{ab}(y_d - y_c) - \tau_{cd}(y_b - y_a)} \tag{8.4}$$

The phase speed is determined from the same parameters. Figure 8.2 shows the coordinate system and the typical wave angle found in relation to Kulite Array 2.

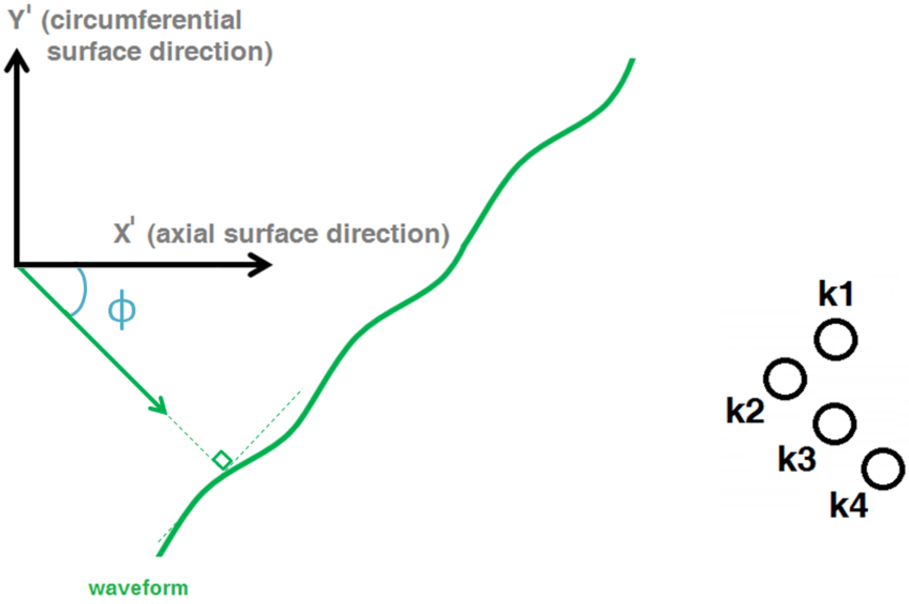

Figure 8.2. Schematic of Kulite Array 2 and reference frame used to determine wave orientation.

Three Kulite signals from E3R4 were used to determine if the traveling crossflow instability was present. The PSD of E3R4, shown in Figure 8.3, reveals a peak in the power spectra, indicating an instability is detected from 20 to 60 kHz at $x = 14.3$-in and at the 90° ray from windward at 4° AoA.

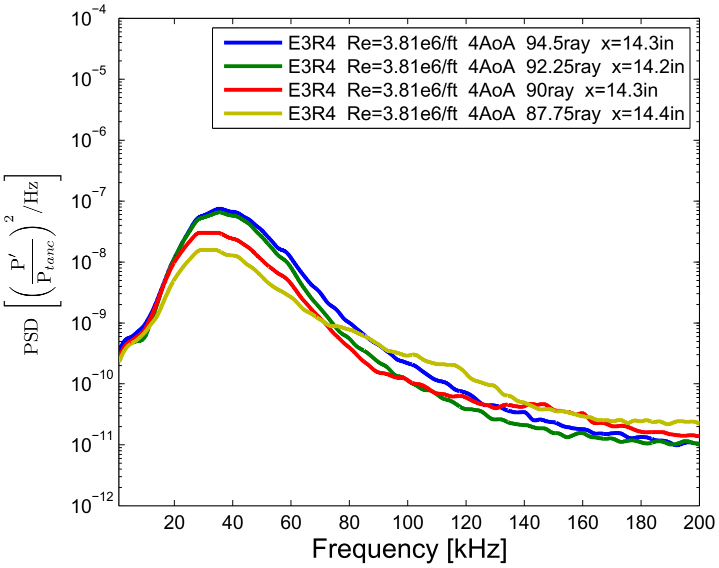

Figure 8.3. PSD of E3R4. Quiet flow, smooth surface, Kulites k1, k2, and k3 near the 90° ray.

8.1.1 Coherence

To determine if an instability is detected at multiple sensors the coherence was calculated. The square of the magnitude of the coherence (C_{xy}) is a measure of how well two signals correspond at each frequency. The coherence is a function of the power spectral densities of each signal, $PSD_{xx}(f)$ and $PSD_{yy}(f)$, and the cross power spectral density, $PSD_{xy}(f)$. Equation 8.5 shows the formula for the coherence.

$$C_{xy}(f) = \frac{|PSD_{xy}(f)|^2}{PSD_{xx}(f)\ PSD_{yy}(f)} \tag{8.5}$$

The values of the coherence range from 0 to 1, where 0 indicates the two signals have no relation and 1 indicates that the signals are perfectly correlated. Figure 8.4 plots the magnitude-squared coherence as a function of frequency. To compare the three sensors to each other in pairs, three combinations were plotted. A wide peak near 50 kHz indicates that all three sensors are detecting the same waves. The wave angles and phase speeds for this band were examined as they show the highest agreement in coherence and power.

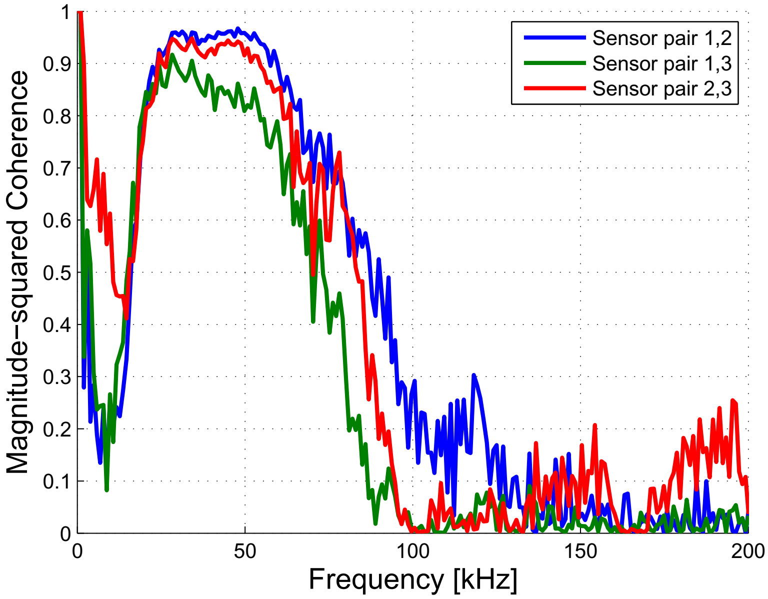

Figure 8.4. Coherence between Kulite sensors for E3R4.

8.1.2 Wave Angle

The direction of the detected waves can be determined from Equation 8.4. Figure 8.5 plots the wave angle as a function of frequency. Two different sensor pairs were compared to show agreement in wave angle across the three sensors. The wave angle was estimated to be between -62° and -58° for frequencies between 30 and 50 kHz, respectively. The angle of the wave was found to be negative with respect to the coordinate system used. This means the wave propagates from lee to wind at those angles.

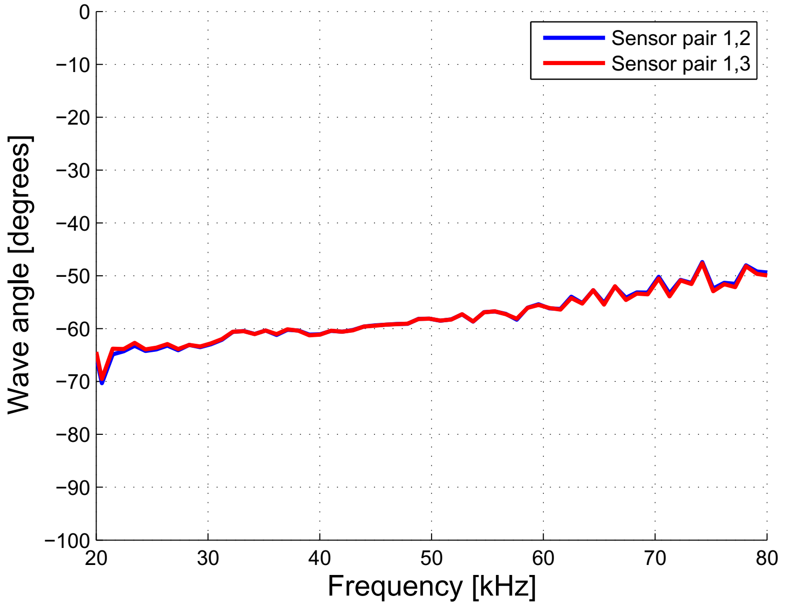

Figure 8.5. Calculated wave angle as a function of frequency for E3R4.

8.1.3 Phase Speed

The phase speed of the detected waves are calculated by the distance the wave travels, sensor to sensor in the direction of the wave angle, divided by the time a particular phase travels that distance. Figure 8.6 shows a plot of the phase speed as a function of frequency. Two different sensor pairs were compared to show agreement in the phase speed across the three sensors. The phase speed was estimated to be between 875 and 1455 ft/s for frequencies between 30 and 50 kHz, respectively.

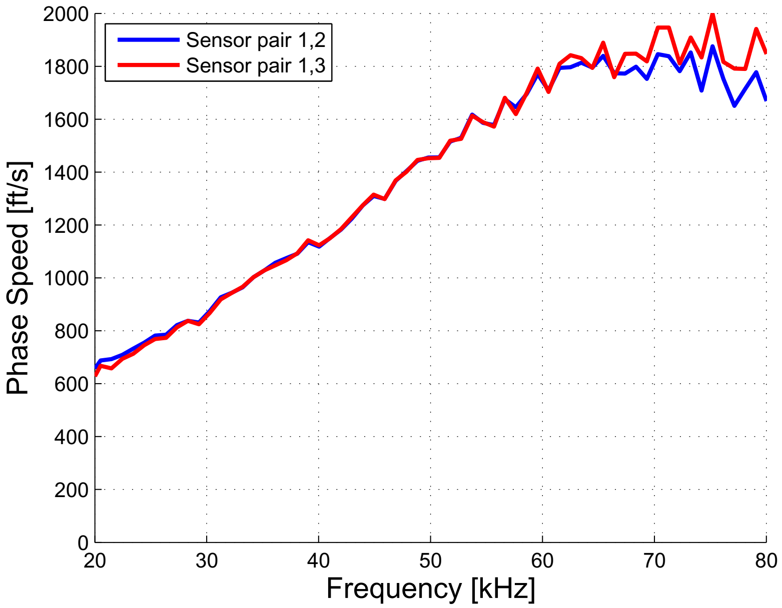

Figure 8.6. Calculated phase velocity as a function of frequency for E3R4.

8.1.4 Instability Analysis

The results from Li et al. [41] and Borg et al. [15], found traveling waves at frequencies below 100 kHz at Mach 6 on an inclined 7° half-angle cone and an elliptical cone, respectively. The results from the computations made by Li et al. found traveling crossflow waves with the highest N-factor values near 40 kHz at 3° and 6° AoA. The disturbances detected with the Kulites for E3R4 detected similar frequencies to the results from Li et al. at the same ray and distance from nosetip. This suggests that traveling crossflow waves are being measured. Additionally, Borg et al. detected disturbances near 40 kHz on an elliptical cone where crossflow was present. They were able to determine the disturbances were traveling waves by calculating the wave properties and comparing to computations.

All the runs that detected traveling waves over three Kulites were compiled in Table 8.1. A wave properties from a substantial number of runs could not be computed because a variety of reasons. Many runs were conducted at the maximum quiet pressure (170 psia) where the Kulite spectra was turbulent to the lee of the 90° ray. Many runs were also conducted below $Re = 2.87{\times}10^6$/ft where no disturbances were detected. Finally over the course of testing, Kulite sensors would fail. This resulted in not having the required amount of sensors to perform the analysis.

Table 8.1 Traveling wave characteristics for frequencies from 30 to 50 kHz. All runs shown are at 4° AoA.

Entry [−]	Run [−]	Re [$\times 10^6$/ft]	Ray [deg]	Wave Angle [deg]	Phase Velocity [ft/s]
3	4	3.81	90	-63 to -58	875 to 1455
3	5	3.41	90	-66 to -62	817 to 1246
3	13	2.88	105	-80 to -73	1074 to 1448
3	14	3.34	105	-66 to -63	829 to 1302
3	18	2.87	120	-58 to -58	789 to 1635
4	1	3.65	90	-66 to -65	734 to 1130
4	2	3.29	90	-68 to -68	865 to 1230
4	7	3.73	90	-67 to -67	723 to 1135
4	12	3.69	60	-60 to -65	800 to 1240

8.2 Reynolds Number Comparison

A range of Reynolds numbers were compared for a smooth cone at 4° AoA under quiet flow. Figure 8.7 shows the results for the Kulite at the 94.5° ray. The data show a peak in the spectra between 20 and 80 kHz, apparently caused by traveling crossflow waves. As the Reynolds number increases, the power of these waves increases.

Figure 8.8 shows the same comparison at the 124.5° ray. However, the highest Reynolds number at the 124.5° ray shows broadband noise over all frequencies which indicates turbulent flow at this position. The TSP image for the highest Reynolds number (E3R16), shown in Figure 7.25, suggests that a stationary vortex crosses over the Kulite at the 124.5° ray. The second highest Reynolds number run shows a broadening of the spectra, but a peak is still apparent near the expected traveling-wave frequencies. A vortex streak is also seen crossing over the Kulite sensor at the same ray. A quantitative analysis of the interaction between the stationary vortices and the traveling-wave amplitudes will be provided in the subsequent sections.

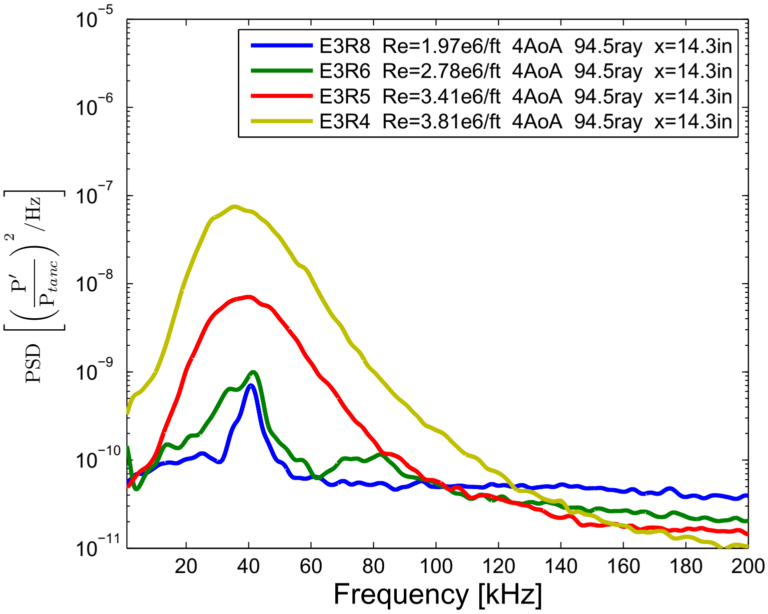

Figure 8.7. PSD of Reynolds number comparison for traveling-wave frequencies. 4° AoA, quiet flow, smooth surface, Kulite at the 94.5° ray.

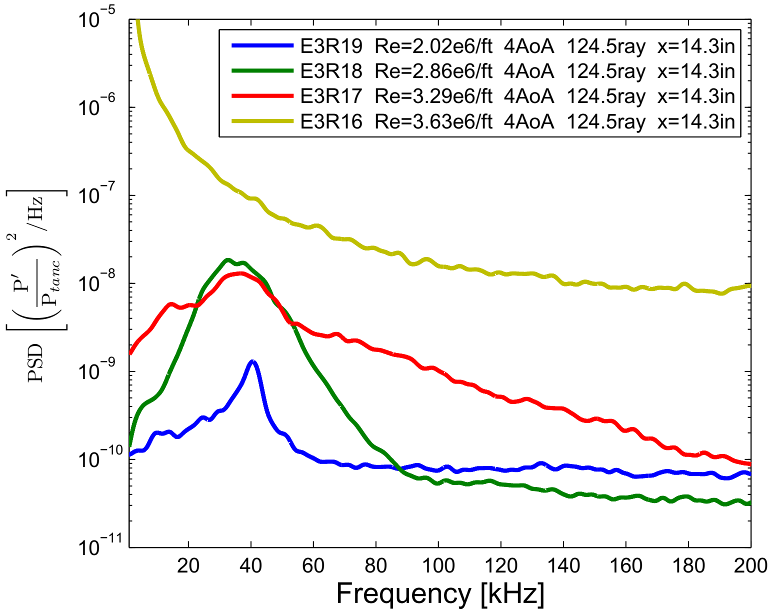

Figure 8.8. PSD of Reynolds number comparison for traveling-wave frequencies. 4° AoA, quiet flow, smooth surface, Kulite at the 124.5° ray.

The PSDs for each run were integrated between 20-80 kHz to determine the RMS fluctuations as a percent of the mean surface pressure. Figure 8.9 shows the RMS fluctuations as a function of the Reynolds number. The amplitudes of fluctuations increase with increasing Reynolds number and azimuthal ray from 60° to 124.5°. Reynolds numbers greater than 3.40×10^6/ft showed turbulent spectra for azimuthal rays to the lee of the 105° ray.

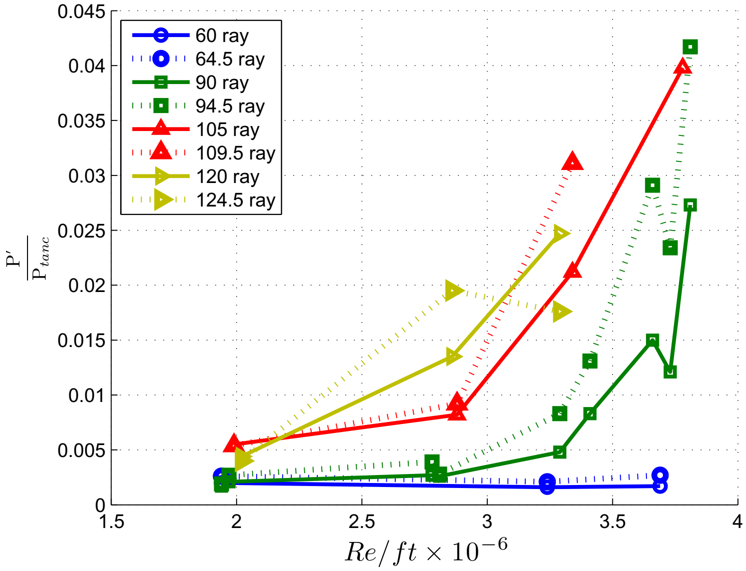

Figure 8.9. RMS fluctuations as a function of the Reynolds number for various azimuthal rays. RMS in the 20-80 kHz band of power spectra. 4° AoA, smooth surface.

8.3 Angle of Attack Comparison

Four angles of attack were compared to observe the effect on traveling-wave amplitudes. Figures 8.10 and 8.11 show the PSD for Kulites at the 90° and 120° ray, respectively, for the Ward cone with the Torlon insert installed. Much like the stationary mode, the traveling mode of crossflow grows with increasing angle of attack. The increase in angle of attack from 3° and 4° produces an order of magnitude increase in the power of the traveling mode at the 90° and 120° ray.

Figure 8.12 shows the PSD for a PCB sensor at the 150° ray. At 3° AoA two peaks are present in the PCB spectra. It is unclear whether the lower frequency peak at 75 kHz is the traveling mode, the second mode, or the result of some interaction between them. The higher frequency peak at 310 kHz appears to be the secondary instability of the stationary crossflow wave, and is discussed in a later section. Above this angle of attack the spectra becomes turbulent and large vortices are seen in the TSP.

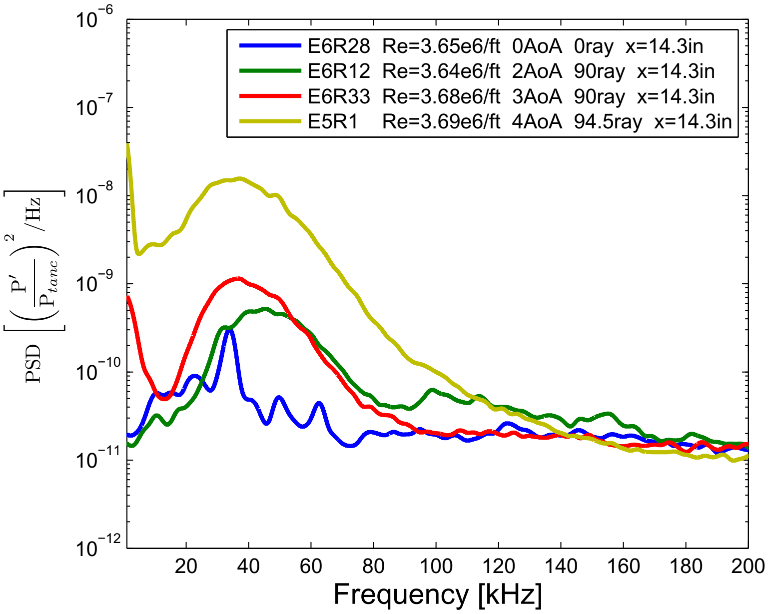

Figure 8.10. PSD of angle of attack comparison for traveling wave frequencies. Quiet flow, Torlon insert, Kulite at the 90° ray.

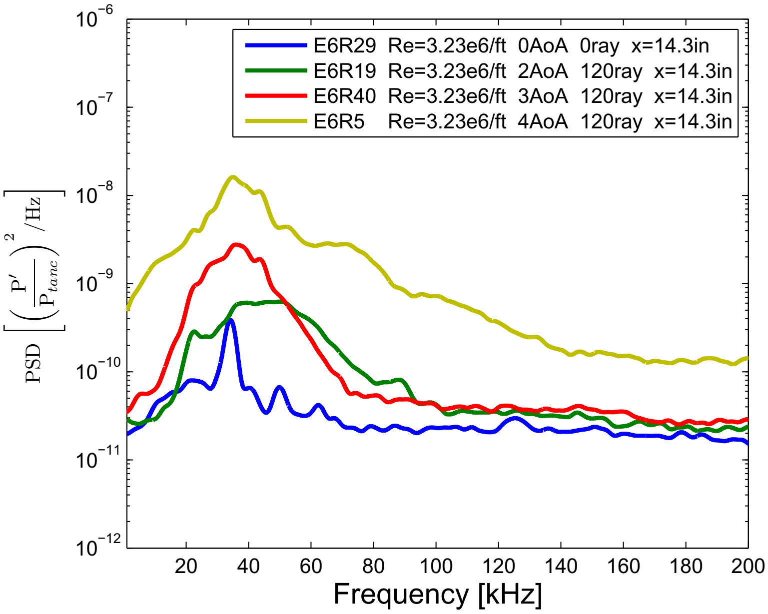

Figure 8.11. PSD of angle of attack comparison for traveling wave frequencies. Quiet flow, Torlon insert, Kulite at the 120° ray.

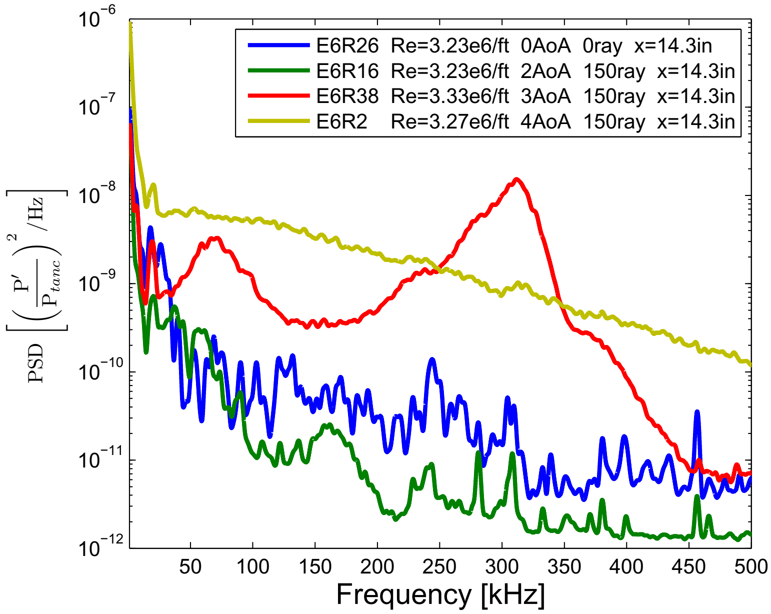

Figure 8.12. PSD of angle of attack comparison for traveling wave frequencies. Quiet flow, Torlon insert, PCB sensor at the 150° ray.

All spectra that detected the traveling crossflow instability at the 60°, 90°, and 120° ray were integrated between 20-80 kHz to determine the RMS fluctuations as a percent of the mean surface pressure, shown in Figure 8.13, 8.14, and 8.15, respectively. All data was taken from Kulites in the Kulite Array 2, where $x = 14.3$-in. Data from the 60° and 120° ray were taken from runs with the Torlon insert installed. The 90°-ray data were taken from runs with no applied roughness and the Torlon insert installed.

At the 60° ray, the amplitudes of the waves are below 0.3% of the mean surface pressure for all angles of attack. The traveling crossflow instability appears to not grow over this range of Reynolds numbers at this azimuthal angle.

At the 90° ray, the smooth and Torlon cases were compared along with the three angles of attack. Runs with vortices crossing over the sensors may alter the amplitudes of the traveling waves. The traveling-wave amplitudes at 2° AoA with the Torlon insert were slightly larger than the amplitudes at 3° AoA below $Re = 3.60\times10^6$/ft.

This is an unexpected result that needs more data to fully explain if this trend is legitimate. The data at 4° AoA shows wave amplitudes on the order of 3 times the amplitudes seen at 2° and 3° AoA for the smooth cases. No data at the 90° ray showed signs of turbulent spectra.

At the 120° ray, the data at 3° AoA shows lower amplitudes than the data at 2° AoA for the two higher Reynolds number cases. This may be due to the stationary vortices crossing over the Kulites causing a decrease in traveling-wave amplitude. Turbulent spectra was found above $Re = 3.23{\times}10^6$/ft for the data at 4° AoA.

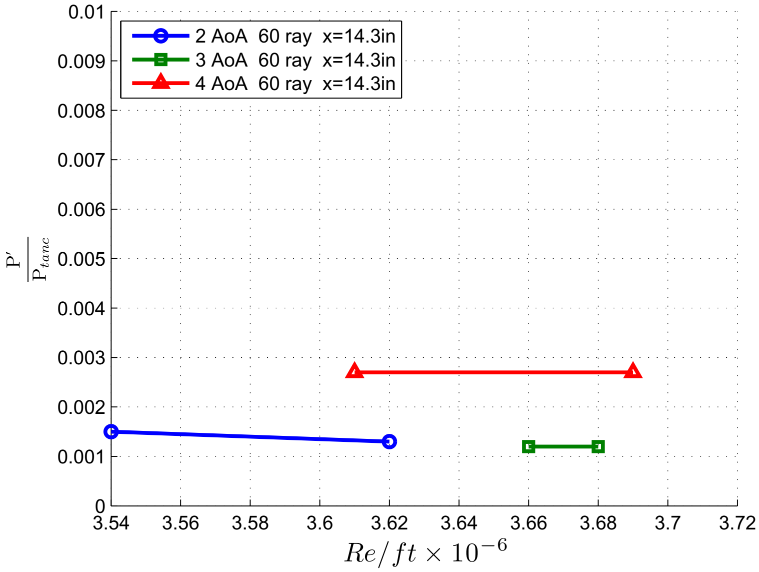

Figure 8.13. RMS fluctuations as a function of the Reynolds number at the 60° ray from windward for 2°, 3°, and 4° AoA. RMS in the 20-80 kHz band of power spectra. All data taken from entry 6 with Torlon insert installed.

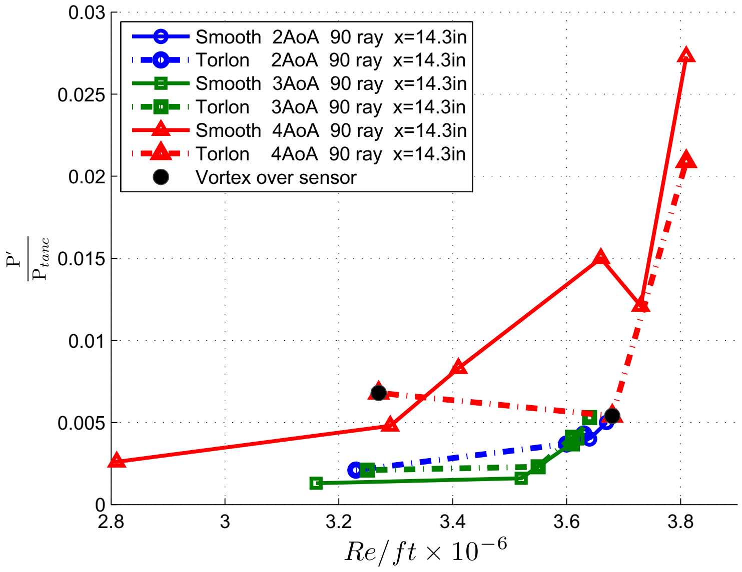

Figure 8.14. RMS fluctuations as a function of the Reynolds number at the 90° ray from windward for 2°, 3°, and 4° AoA. RMS in the 20-80 kHz band of power spectra.

8.4 Tunnel Noise Comparison

The effect of tunnel noise was evaluated during entry 3. Figure 8.16 compares E3R8 and E3R9 near the same Reynolds number with a Kulite at the 90° ray. A small peak is observed in the spectra near 40 kHz under quiet flow conditions. The low Reynolds number and the frequency of the peak suggest that the peak is the traveling crossflow instability with low power. Under noisy flow conditions, a region two orders of magnitude higher than the quiet flow spectra was observed between 20-60 kHz. Figure 8.17 shows quiet (blue lines) and noisy (red lines) spectra for a PCB sensor on the 90° ray at $x = 12.6$-in, 1.7 inches upstream of the Kulite array. A similar spectra is seen between the two sensor types between 20-60 kHz for the noisy flow case, but the PCB sensor did not detect any traveling waves under quiet flow conditions.

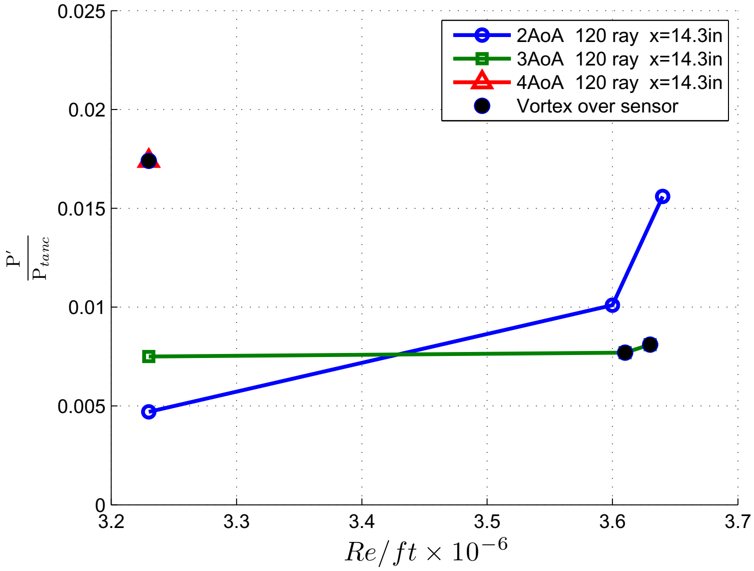

Figure 8.15. RMS fluctuations as a function of the Reynolds number at the 120° ray from windward for 2°, 3°, and 4° AoA. RMS in the 20-80 kHz band of power spectra.

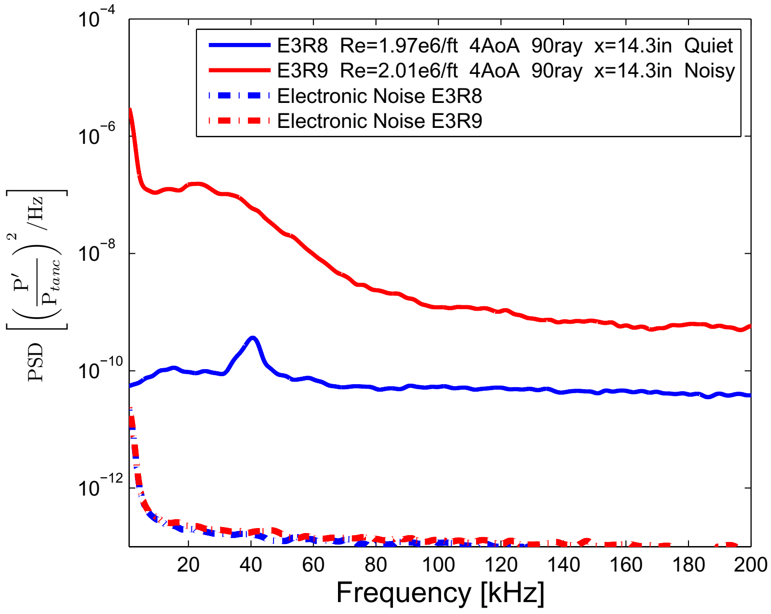

Figure 8.16. PSD for tunnel noise comparison for traveling-wave frequencies. 4° AoA, smooth surface, Kulite at the 90° ray.

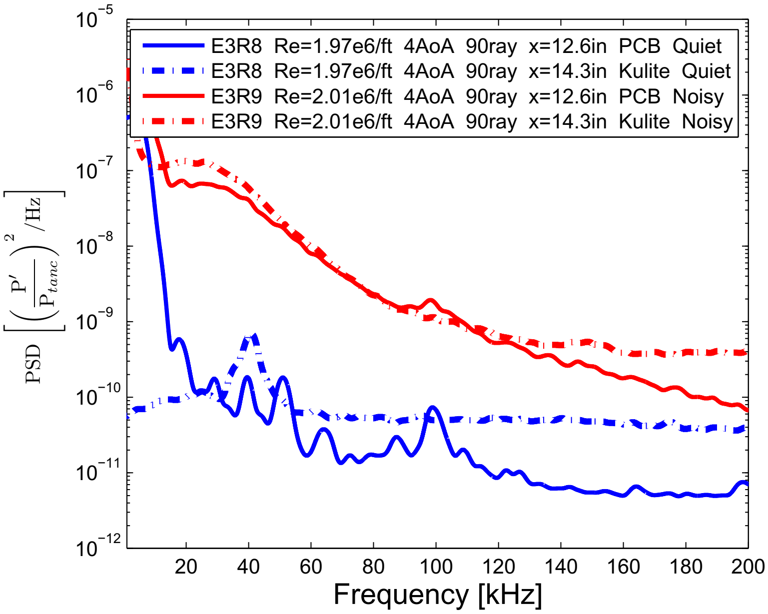

Figure 8.17. PSD for tunnel noise comparison for traveling wave frequencies. 4° AoA, smooth surface, Each sensor type at the 90° ray.

The spectral content between 20-60 kHz for the noisy flow results looks similar to power spectra seen from traveling waves under quiet flow if the 40 kHz peak was shifted near 20 kHz. The Kulite signals from noisy runs were analyzed to determine if wave properties could be calculated. Figure 8.18 shows the wave properties from three Kulites in Kulite Array 2 located near the 90° ray and $x = 14.3$-in. The three signals show coherence at frequencies below 70 kHz with the highest coherence near 30 kHz. The wave angles and phase speeds between 20-60 kHz also show agreeable trends between the sensor pairs. The calculated wave properties suggest that a wave-like instability is present under noisy flow conditions. The frequency of the instability under noisy flow is lower than the traveling-wave frequencies under quiet flow. The mechanism that would shift the traveling crossflow instability is not known by the author. The instability detected under noisy flow should be examined in future experiments to determine if the instability is a modulation of the traveling waves or another disturbance.

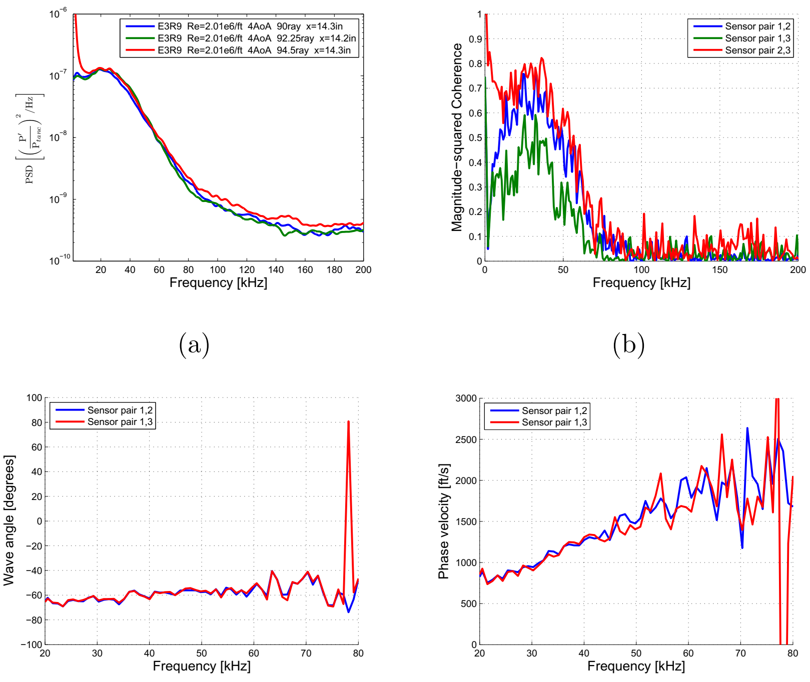

(a)

(b)

(c)

(d)

Figure 8.18. Wave calculations for E4R9. (a) PSD (b) Coherence (c) Wave angle (d) Phase velocity

8.5 Similarity between Pressure Sensors

PSD plots for the PCB 132A31 and the Kulite XCQ-062-15A transducers were compared to understand the differences in the sensing methods and how they affect the amplitude and frequency of the traveling mode. While testing angles of attack during entry 6, runs were tested with the Kulite Array 2 near the 60°, 90°, and 120° ray. Rotating the sensor positions by increments of 30° allowed the PCB sensors to be compared to the Kulites at the same azimuthal ray.

Figure 8.19 shows the comparison of two runs with a Kulite sensor (solid line) and two runs with a PCB sensor (dotted line) at the 90° ray. Most power spectra from PCB sensors used in these experiments showed noise levels above where Kulite sensors detect the traveling crossflow instability. This could be due to the size of the sensing element in the PCB sensor. The sensing element could be averaging over a significant portion of a wavelength of the traveling waves.

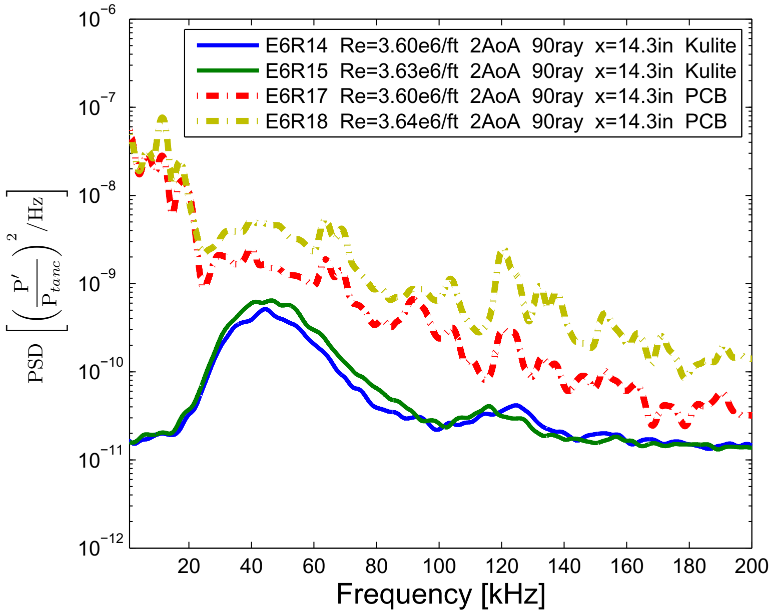

Figure 8.19. PSD of PCB and Kulite sensors with similar tunnel conditions and sensor location. 2° AoA, quiet flow, Torlon insert, both sensor types at the 90° ray.

Figure 8.20 compares each type of sensor at the 120° ray at 2° AoA. Comparing E6R14 and E6R39 at $Re = 3.60{\times}10^6/\text{ft}$, the detected traveling-wave frequencies agree well between the two sensors with a percent difference of 29.5% in RMS fluctuations, integrated from 20-80 kHz. The differences in amplitudes could be due to the experimental conditions between runs as well as calibration issues since the data from the PCB sensors are reduced using factory calibrations. Figure 8.21 compares each type of sensor at the 90° ray at 3° AoA. Comparing E6R35 and E6R45, the detected traveling-wave frequencies agree well between the two sensors with a percent difference of 2.7% in RMS fluctuations, integrated from 20-80 kHz. Figure 8.22 compares each type of sensor at the 120° ray at 3° AoA. Comparing E6R35 and E6R39, the detected traveling-wave frequencies agree well between the two sensors with a percent difference of 2.6% in RMS fluctuations, integrated from 20-80 kHz.

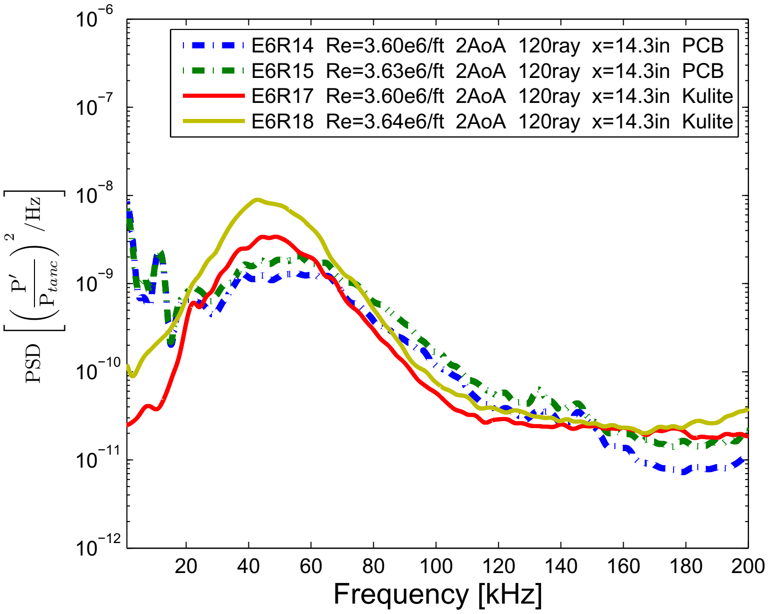

Figure 8.20. PSD of PCB and Kulite sensors with similar tunnel conditions and sensor location. 2° AoA, quiet flow, Torlon insert, both sensor types at the 120° ray.

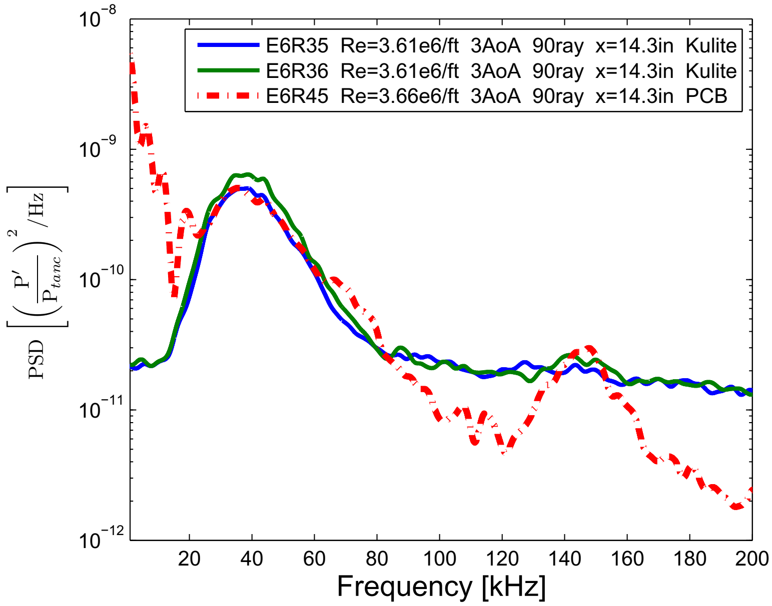

Figure 8.21. PSD of PCB and Kulite sensors with similar tunnel conditions and sensor location. 3° AoA, quiet flow, Torlon insert, both sensor types at the 90° ray.

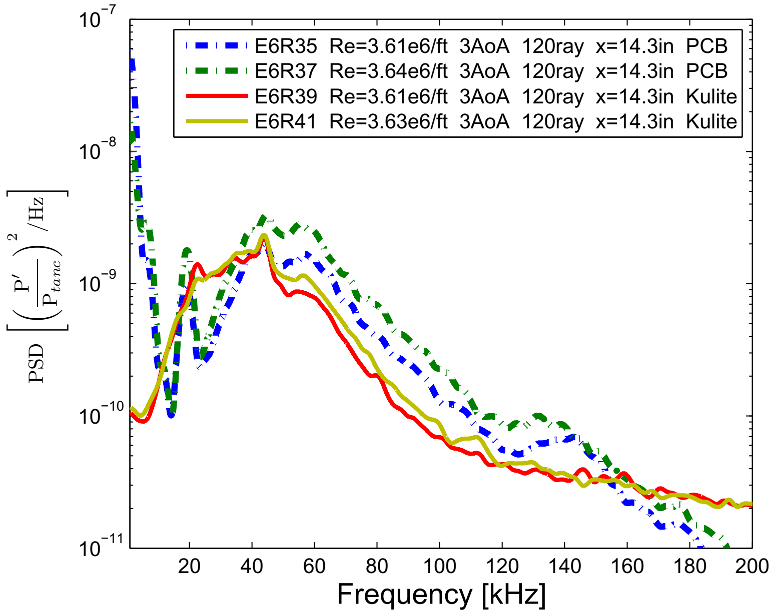

Figure 8.22. PSD of PCB and Kulite sensors with similar tunnel conditions and sensor location. 3° AoA, quiet flow, Torlon insert, both sensor types at the 120° ray.

9. INTERACTIONS BETWEEN STATIONARY & TRAVELING WAVES

Low-speed experiments have shown that the saturation amplitudes of stationary and traveling waves are dependent on their initial amplitudes. As Bippes and Lerche [33] have shown in their experiments, increasing the initial amplitudes of the traveling waves leads to a decrease in the saturation amplitudes of the stationary waves. Experiments were conducted to determine if the same relationship holds at hypersonic speeds as well as quantifying the interaction in terms of heat flux and RMS fluctuation. The interaction between the stationary and traveling waves was observed by modulating the growth of the stationary vortices. In order to alter the vortex positions and their growth along the cone, roughness elements were used with the Ward cone. Roughness elements were added during entries 4 and 6. Nail polish was used during entry 4 as a quick technique to determine if a sizable roughness could alter stationary vortices. Entry 6 used a Torlon insert near the nosetip as a more well-defined roughness element. The RMS roughness values of the TSP layers for each entry and nail polish applications are compiled in Table B.1, along with the dimensions of the Torlon insert roughness elements.

9.1 Entry 4 Interactions

For the fourth tunnel entry, the Ward cone was coated with TSP and a distributed roughness was added to the cone surface. The TSP coating was measured by the profilometer at random locations around the cone. The average RMS roughness was 0.05 mil. The paint was feathered near the TSP edge to create a gradual slope to the bare aluminum, but the slope of the feathered section was not measured. The roughness insert section of the Ward cone must align flush with the nosetip on the upstream edge and with the main body of the model on the downstream edge. The interface between each end is examined for steps or gaps that could have an affect on the flow. The upstream interface had a rearward facing step of 0.3 mil in the direction of flow. The downstream interface had a forward facing step of 0.15 mil in the same direction.

9.1.1 E4 Roughness Application and Measurement

An initial strip of blue nail polish was added to the Ward cone during entry 4 testing. The strip was added 8.75-in from the nosetip, just forward of Kulite Array 1. The strip covered approximately 60 degrees centered over the rays around the Kulite positions. The width of the strip was approximately 0.1-in. More blue nail polish was later added to connect the strip into a ring to cover all rays of the cone. Figure 9.1 shows both roughness patterns on the Ward cone.

Using the SJ-130 profilometer, the roughness ring was measured on the cone's surface and on the negative mold. Both surfaces are compared in Figure 9.2 at azimuthal positions 90° and 270° from the Kulite position k3. Both profiles match well in the region of large roughness, but deviate outside of this region. The negative-mold technique was used for all profilometer readings to reduce the error that could occur with measuring on a curved surface. This error would only occur when measuring across the span of the cone. The RMS roughness of the ring was measured across the width of the ring and averaged over multiple rays. The average RMS roughness was 2.04 mil.

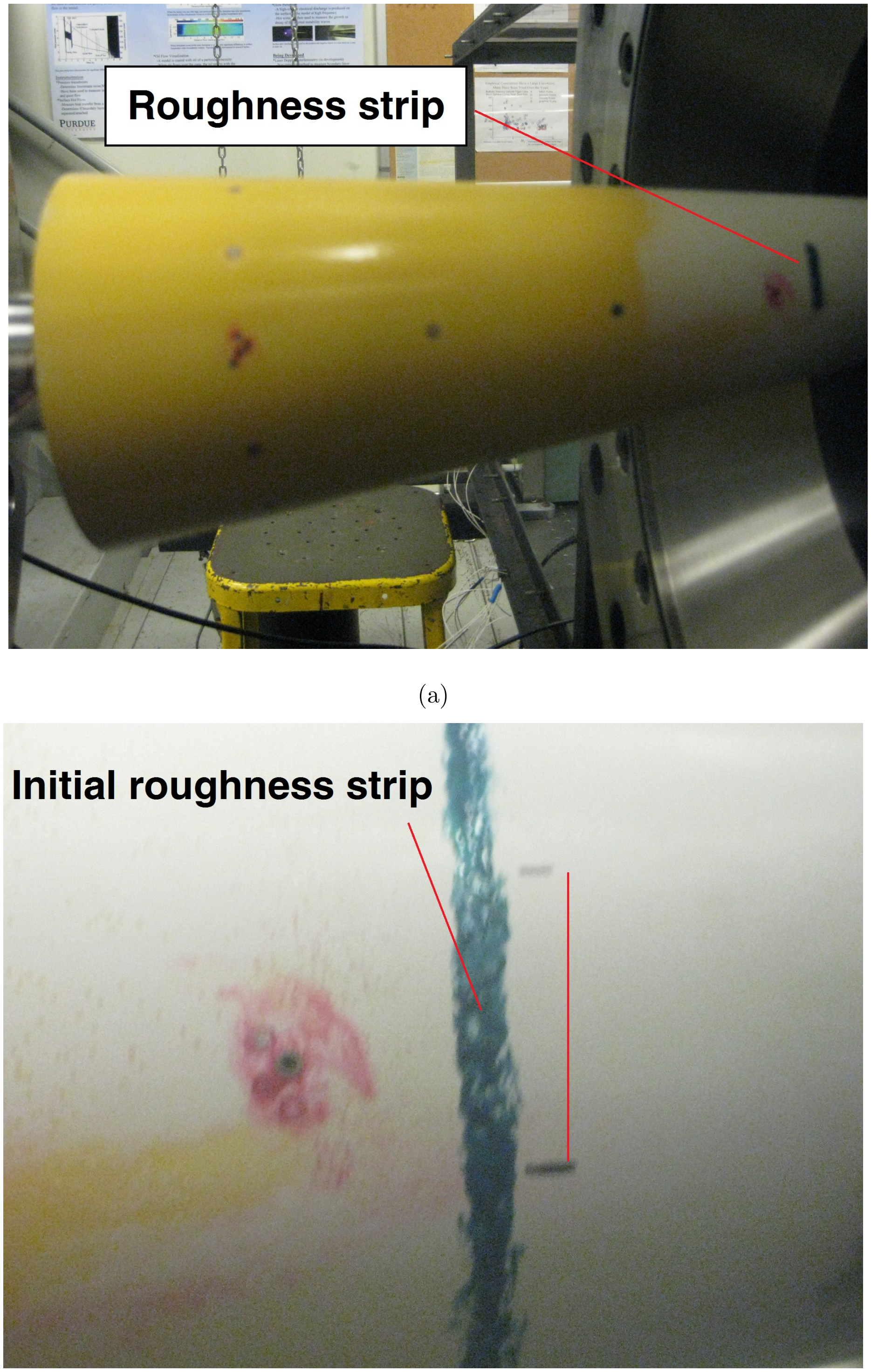

(a)

(b)

Figure 9.1. Photographs of Ward Cone during entry 4 testing with initial nail-polish roughness strip (a) and roughness ring (b).

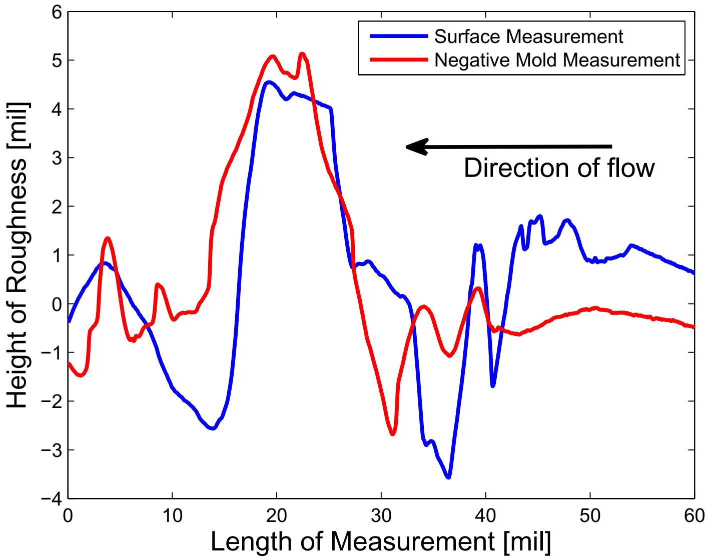

(a)

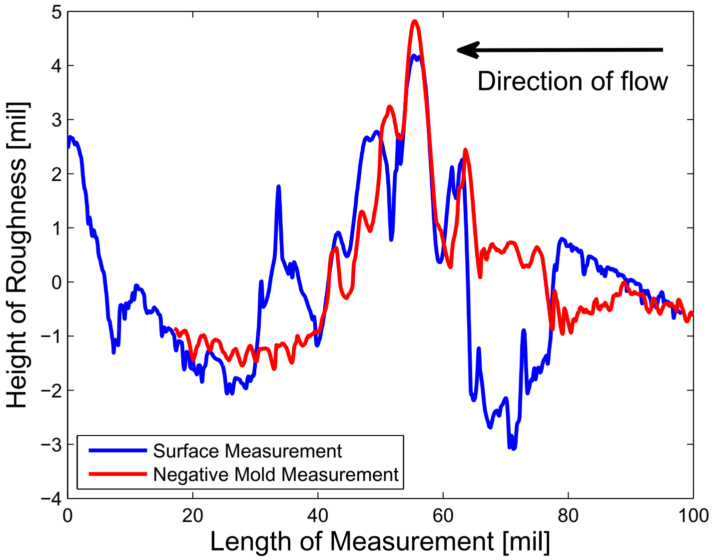

(b)

Figure 9.2. Surface and negative height profile of E4 roughness ring (a) 90° and (b) 270° from Kulite 3. Profiles from right to left were measured in the direction of flow.

9.1.2 E4 Roughness Effects

Global heat transfer contours for a smooth case (E4R1), a roughness strip (E4R23), and a roughness ring (E4R29) were imaged in Figures 9.3, 9.4, and 9.5, respectively. The smooth case shows a typical heating pattern with stationary vortices appearing above the 120° ray. For Figure 9.4, the nail polish strip was between the 60° and 120° rays. Adding the roughness strip produced higher heat transfer from the vortices. Results from the roughness ring show a large increase in the number of vortices observed on the cone. These vortices are due to the additional roughness on the wind and lee sides of the initial roughness strip exciting stationary waves at the other azimuthal rays.

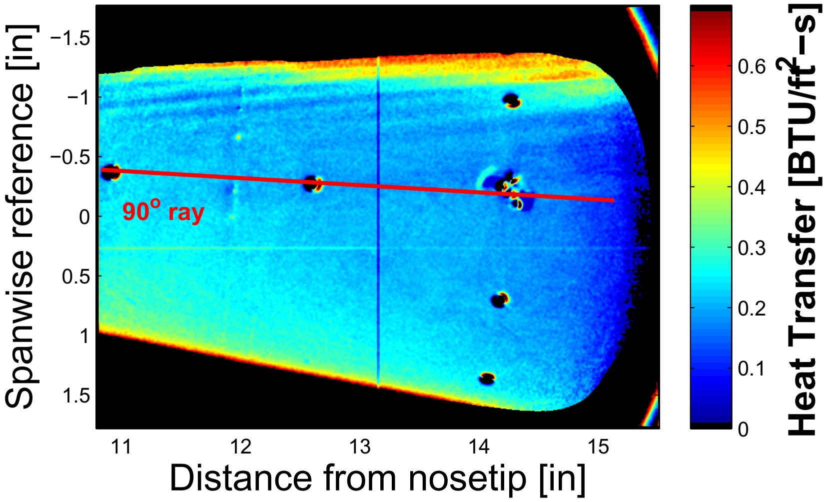

Figure 9.3. Heat transfer contour of E4R1. 4°AoA, quiet flow, smooth surface, Kulites near the 90° ray. $Re = 3.66\times10^6$/ft, $P_o = 156.8$ psia, $T_o = 301.7$°F, $T_w = 74.6$°F.

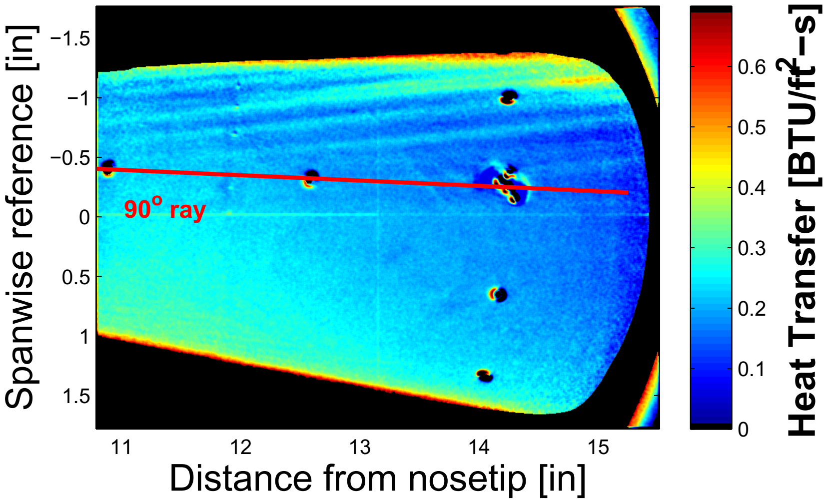

Figure 9.4. Heat transfer contour of E4R23. 4°AoA, quiet flow, E4 roughness strip, Kulites near the 90° ray. $Re = 3.68{\times}10^6$/ft, $P_o =$ 157.2 psia, $T_o = 299.6°$F, $T_w = 79.9°$F.

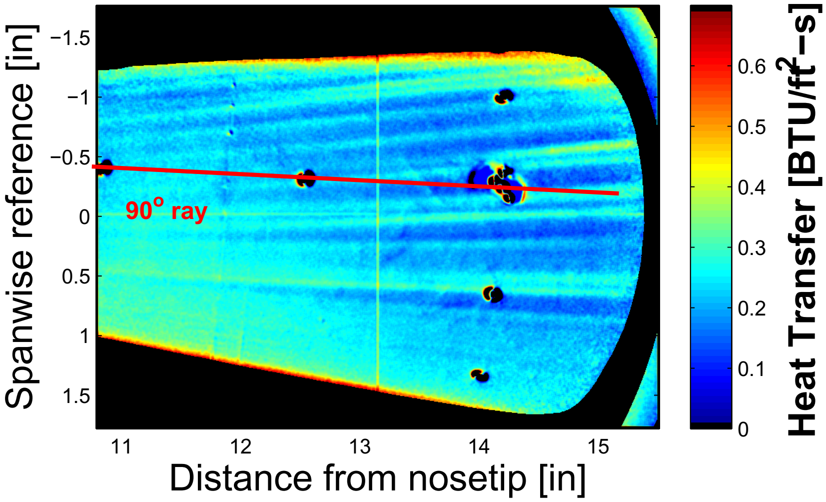

Figure 9.5. Heat transfer contour of E4R29. 4°AoA, quiet flow, E4 roughness ring, Kulites near the 90° ray. $Re = 3.66{\times}10^6$/ft, $P_o =$ 157.1 psia, $T_o = 302.1°$F, $T_w = 76.8°$F.

Azimuthal cuts were taken at $x = 12.5$-in, $x = 13.5$-in, and $x = 14.5$-in for the three runs as shown on Figures 9.6, 9.7, and 9.8, respectively. At $x = 12.5$-in peaks in heat flux are seen near the 105° and the 115° rays for both applied roughnesses. Further aft at $x = 13.5$-in, these peaks shift 5° to the lee and the peak at the 120° ray grows in amplitude for both roughness cases. Heat-flux peaks are also seen from the 60° to 100° ray for the roughness-ring case. The furthest aft position of $x = 14.5$-in shows the peaks again shift approximately 5° toward the lee side of the cone. From the TSP, the vortex paths move toward the lee side of the cone. The heat-flux peaks between the 60° and 120° rays were, on average, 50% higher than for the smooth case. To quantify the interaction between the stationary and traveling modes, the heat transfer from the vortices was compared to the pressure fluctuations from the Kulites that detected traveling waves. The sensors in Kulite Array 2 are marked on Figure 9.8 to show the azimuthal location of the sensors relative to where the vortices cross.

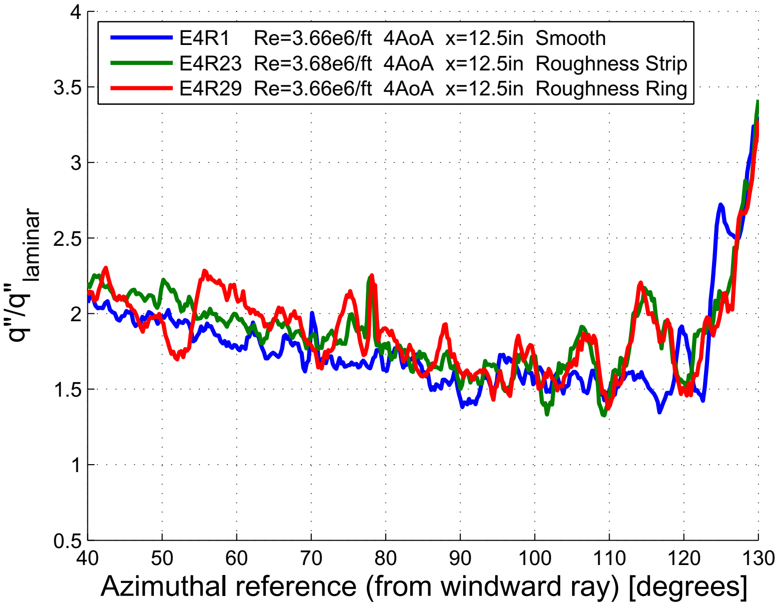

Figure 9.6. Spanwise heat transfer profile of E4R1, E4R23, and E4R29 at $x = 12.5$-in. 4°AoA, quiet flow, Kulite array near the 90° ray.

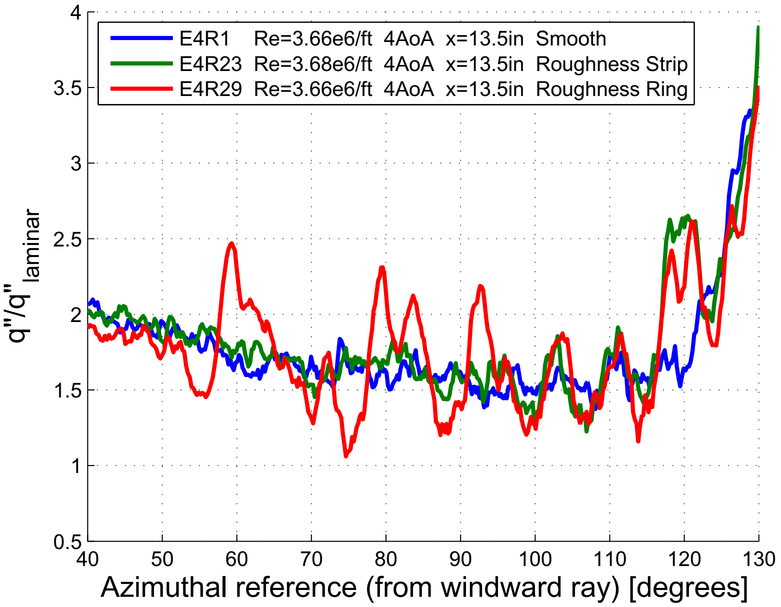

Figure 9.7. Spanwise heat transfer profile of E4R1, E4R23, and E4R29 at $x = 13.5$-in. 4°AoA, quiet flow, Kulite array near the 90° ray.

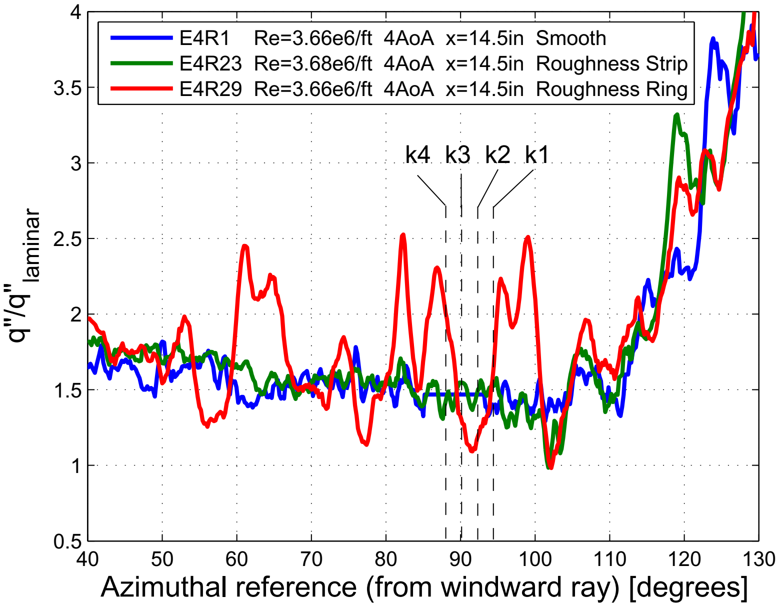

Figure 9.8. Spanwise heat transfer profile of E4R1, E4R23, and E4R29 at $x = 14.5$-in. 4°AoA, quiet flow, Kulite array near the 90° ray.

The heat transfer profiles of E4R29 show the vortices crossing over Kulite k4 and k1 at the 87.75° and 94.5° ray, respectively. The spectra from these sensors was compared against sensors k2 and k3 to determine the effects of the interaction between the stationary and traveling crossflow waves. Figure 9.9 shows the PSD of the four sensors in Kulite Array 2 for E4R29. Kulite k4 shows a reduction in power an order of magnitude lower than the other three Kulites. This inverse relationship is similar to low-speed crossflow properties. Both k1 and k4 spectra were found to have stationary waves crossing over each sensor, but a decrease in the traveling-wave amplitude was not observed in the k1 spectrum. Instead, a disturbance near 410 kHz was found. A discussion of this disturbance is provided in the subsequent section.

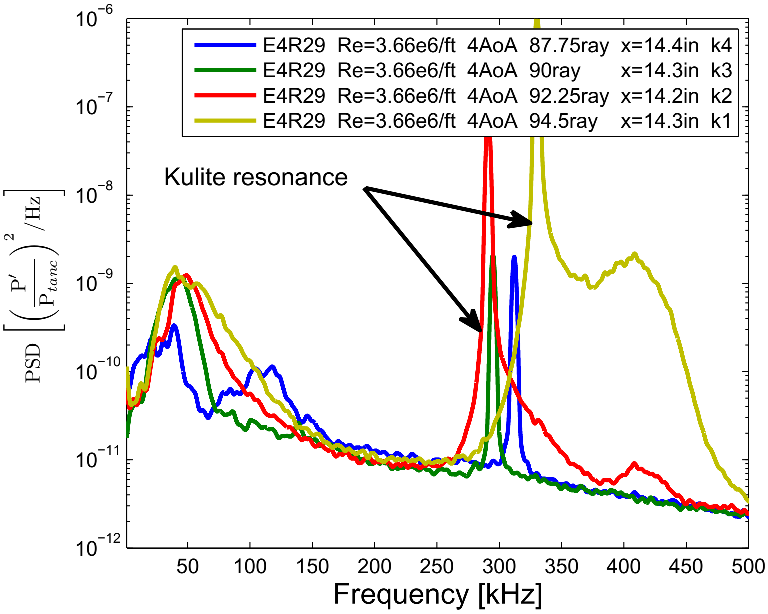

Figure 9.9. PSD of all sensors in Kulite Array 2 for E4R29.

Kulite k4 was compared over the three roughness cases in Figure 9.10. The comparison reveals a reduction in the amplitude of the traveling waves when the roughness ring was added. The local heat transfer grew 51% higher from the smooth to roughness ring case and the traveling wave amplitudes decreased nearly two orders of magnitude. The traveling-wave amplitude is slightly smaller for the roughness strip case with respect to the smooth case.

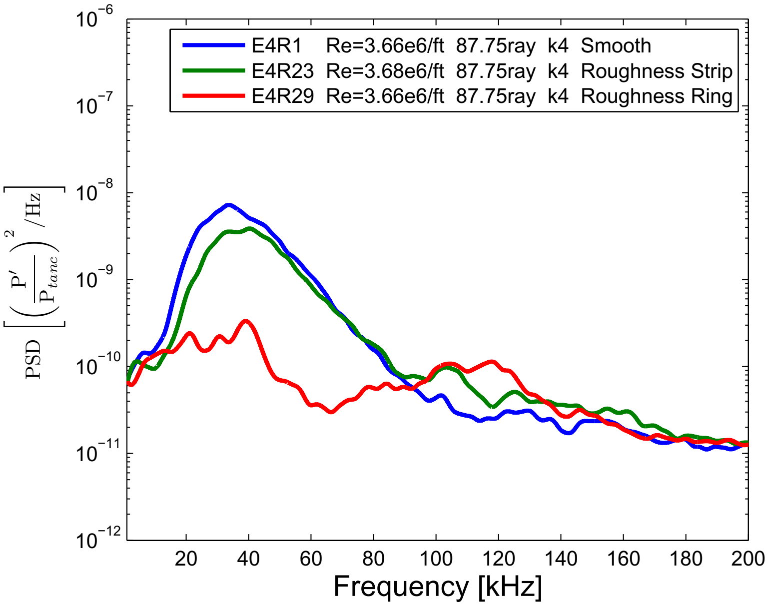

Figure 9.10. PSD of E4R1 (smooth surface), E4R24 (E4 roughness strip), and E4R29 (E4 roughness ring) at $x = 14.4$-in, 4°AoA, quiet flow, Kulite 4 at the 87.75° ray.

A similar comparison was made for Kulite k2 (92.25° ray), positioned 5° to the lee of k4. At this position the sensor was not in the path of a vortex streak during the roughness ring test (E4R29). A PSD comparison for the same three roughness cases is shown on Figure 9.11.

Much like the comparisons at k4, the roughness-ring spectrum at k2 shows traveling-wave power an order of magnitude lower than the smooth and roughness strip cases. However, the roughness-ring spectrum shows a peak around 45 kHz whereas a peak was not found for the same run at k4. A vortex streak is not seen crossing over the k2 position for the three roughness cases. It is possible that the stationary vortices at higher rays and upstream of the sensor are altering the flowfield to reduce the amplitudes of the traveling waves as they pass across the cone. A schematic of the process is shown in Figure 9.12.

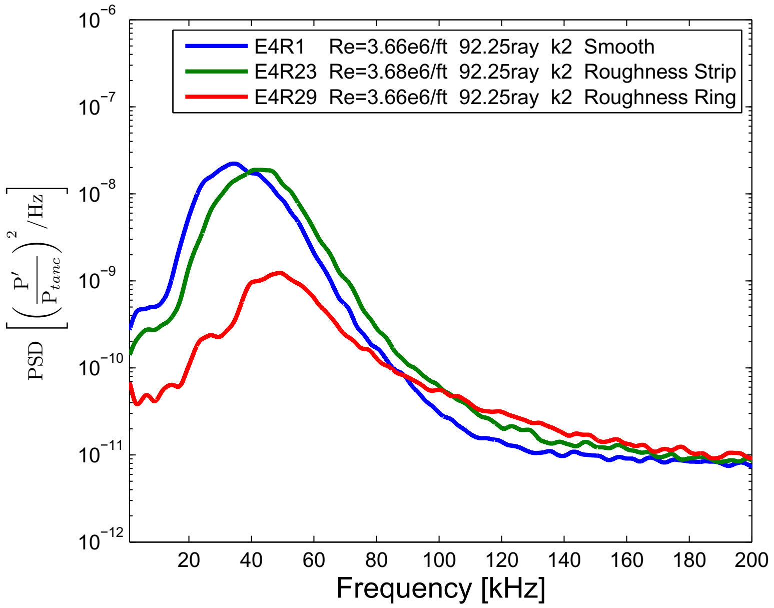

Figure 9.11. PSD of E4R1 (smooth surface), E4R24 (E4 roughness strip), and E4R29 (E4 roughness ring) at $x = 14.2$-in, 4°AoA, quiet flow, Kulite 2 at the 92.25° ray.

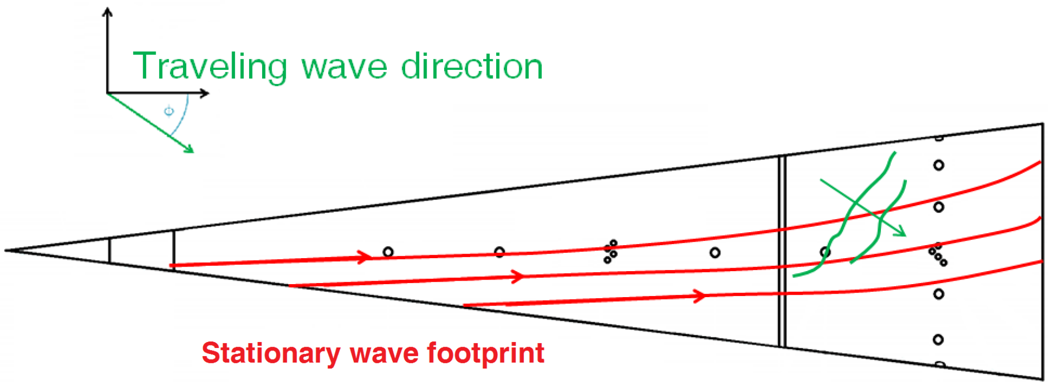

Figure 9.12. Schematic of the stationary and traveling crossflow wave directions.

9.2 Entry 6 Interactions

The sixth tunnel entry used discrete roughness elements on Torlon insert #6 near the nosetip to induce vortices. The insert was designed to have approximately the same roughness dimensions for all rays. The TSP coating was measured to have an average RMS roughness of 0.10 mil.

9.2.1 E6 Roughness Application and Measurement

The dimples in the Torlon insert were first measured to approximate the roughness shape and size. The first measurements of the dimples were taken from the dimensions of the pin used to indent the Torlon. The diameter of the pin was 31 mil and it was pressed into the Torlon to a depth of 24 mil. Figure 9.13 shows a photograph of the Torlon insert with the roughnesses. A Keyence digital microscope was used by the manufacturer to survey the indentions as a sample. A contour plot of the roughnesses is shown on Figure 9.14 and measurements of the cross-section are shown on Figure 9.15. The average diameter of the roughnesses, measured at the rim of the indention, was 30 mil using the digital microscope. Only two measurements were made to calculate the depth of the indentions. The average of the two measurements was 4.94 mil. The profilometer was also used to approximate the diameter and depth of the indentions, shown on Figure 9.16. An accurate depth was difficult to measure since there is no method to guide the profilometer stylus exactly over the center of each indention. The maximum depth recorded by the profilometer was 4 mil.

Figure 9.13. Photograph of Torlon insert assembled to the Ward Cone and nosetip.

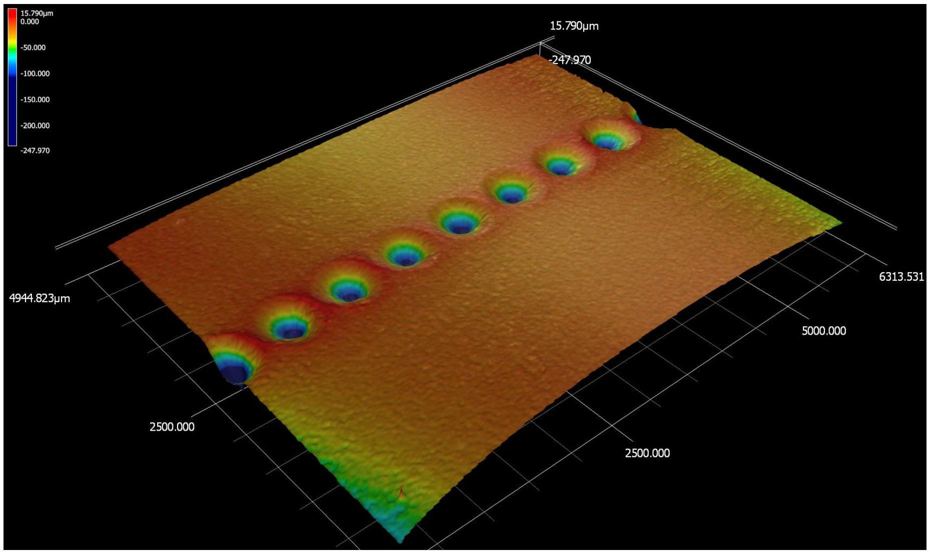

Figure 9.14. Contour of Torlon insert.

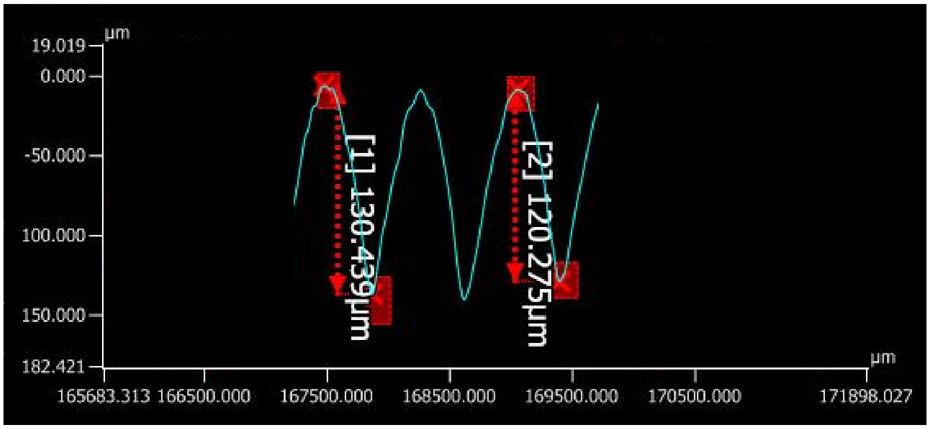

Figure 9.15. Profile of Torlon insert using the Keyence digital microscope. Measured depths of 4.74 mil (120.28 μm) and 5.14 mil (130.44 μm).

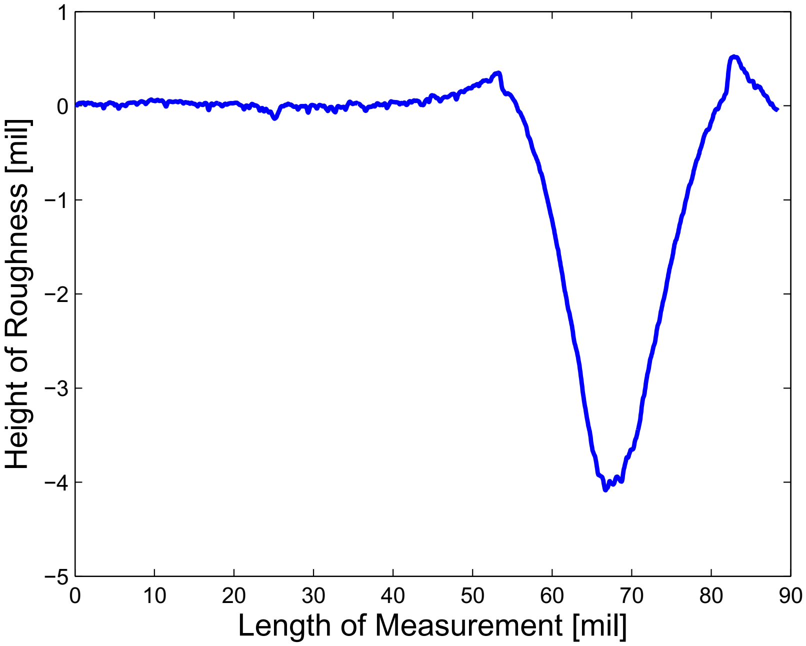

Figure 9.16. Profile of Torlon insert using the SJ-130 profilometer.

9.2.2 E6 Roughness Effects

The effects of the roughness-induced crossflow waves were compared to smooth cases for 2°, 3°, and 4° angle of attack. At 2° angle of attack, the global heat transfer contours are shown in Figures 9.17 and 9.18. Faint streaks are visible near the PCB sensor at the 120° ray in Figure 9.18. An azimuthal profile, shown in Figure 9.19, reveals slight differences in heat flux between the runs near the 110° and 120° rays at $x = 14.0$-in .

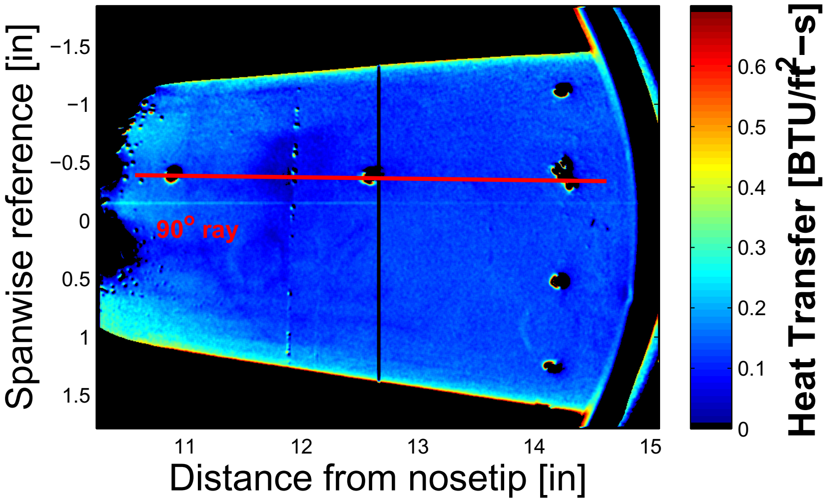

Figure 9.17. Heat transfer contour of E6R12. 2°AoA, quiet flow, smooth surface, Kulite array on the 90° ray. $Re = 3.64x10^6/ft$, $P_o =$ 155.7 psia, $T_o =$ 300.4°F, $T_w =$ 79.8°F.

As expected, the power spectra of the two cases at the 90° ray, Figure 9.20, shows the traveling-wave amplitudes are nearly the same. At the 120° ray, runs E6R13 and E6R14 were also compared to show similar findings to E6R12 and E6R15, shown in Figure 9.21. The traveling-wave amplitudes for the four cases showed similar results. A disturbance near 225 kHz was observed in both smooth cases, but not in the Torlon insert cases. The faint streaks observed near the 120° ray when the Torlon insert was

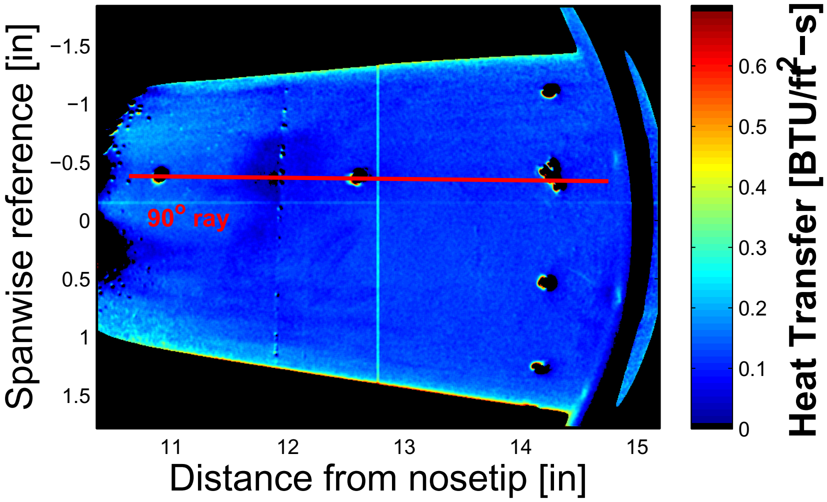

Figure 9.18. Heat transfer contour of E6R15. 2°AoA, quiet flow, Torlon insert, Kulite array on the 90° ray. $Re = 3.63x10^6/ft$, $P_o =$ 156.9 psia, $T_o = 304.9$°F, $T_w = 86.5$°F.

installed may be the cause of this disturbance dampening. The author believes this disturbance to be the second-mode instability. At angles of attack closer to zero, the crossflow component may not be as dominant, so the second-mode could still develop. When the Torlon insert is added, stationary vortices are excited which may inhibit the growth of the second-mode.

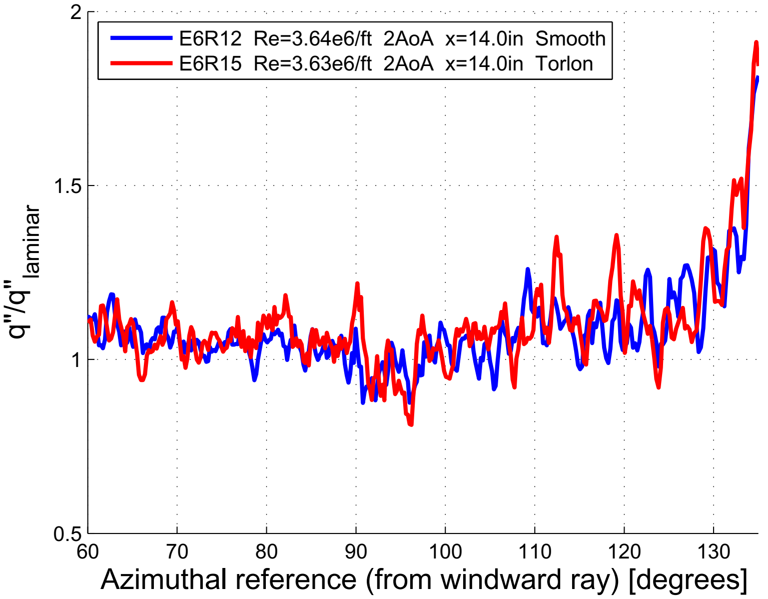

Figure 9.19. Spanwise heat transfer profile of E6R12 and E6R15 at $x = 14.0$-in. 2°AoA, quiet flow, Kulite array near the 90° ray.

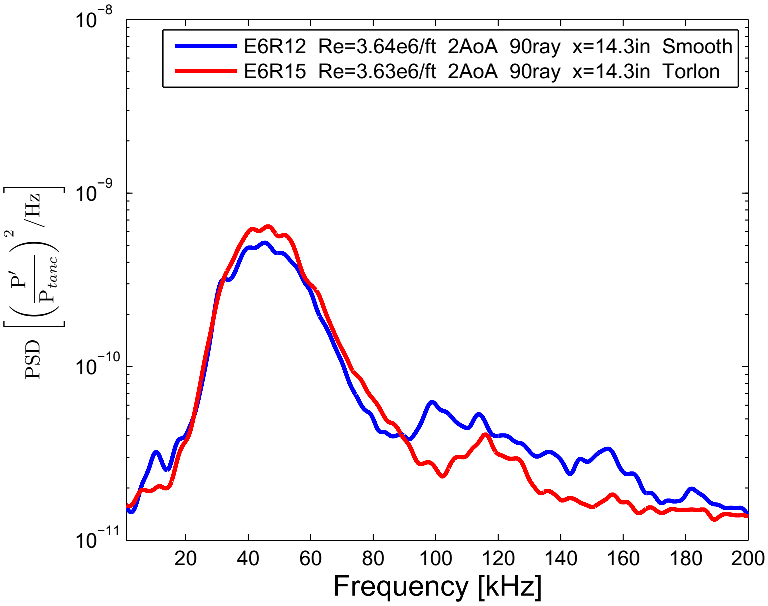

Figure 9.20. PSD of E6R12 (smooth surface) and E6R15 (Torlon insert) for cone at 2°AoA under quiet flow. Kulite at 90° ray and $x = 14.3$-in.

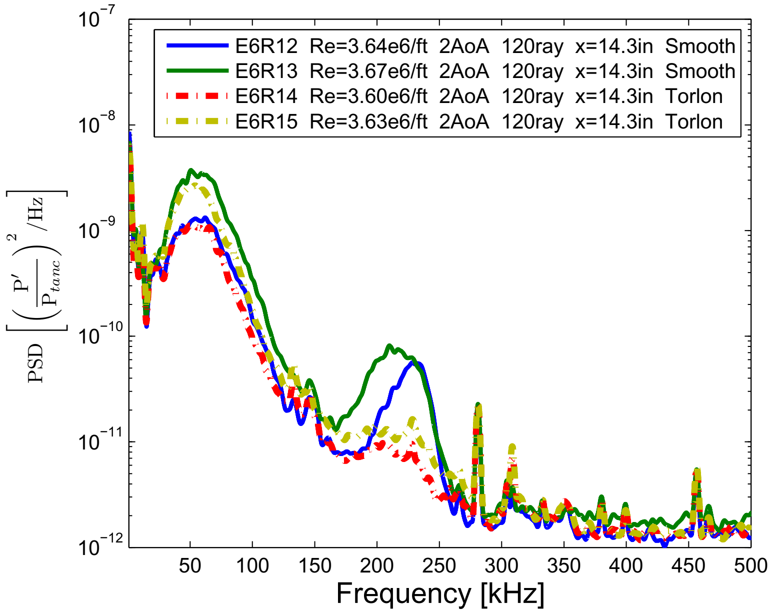

Figure 9.21. PSD of E6R12 E6R13 (smooth surface, solid lines) and E6R14 E6R15 (Torlon insert, dotted lines) for cone at 2°AoA under quiet flow. PCB at the 120° ray and $x = 14.3$-in.

At 3° angle of attack, the global heat transfer contours in Figure 9.22 and Figure 9.23 show differences in the vortex streaks that appear to the lee of the 90° ray. For the Torlon insert case, faint vortex streaks were observed near the 110° and 120° rays at $x = 14.3$-in, while more definitive streaks are seen to the lee of the 120° ray. An azimuthal profile at $x = 14.0$-in, Figure 9.24, was taken to quantify the differences in heat transfer and streak paths between the two cases. One peak in heat flux was found at the 130° ray for the smooth case while four peaks spaced approximately 10° apart were found in the Torlon insert case (105°, 115°, 125°, and 133°). The traveling-wave amplitudes at the 90° and 120° rays were smaller when the Torlon insert was installed, shown in Figure 9.25 and Figure 9.26.

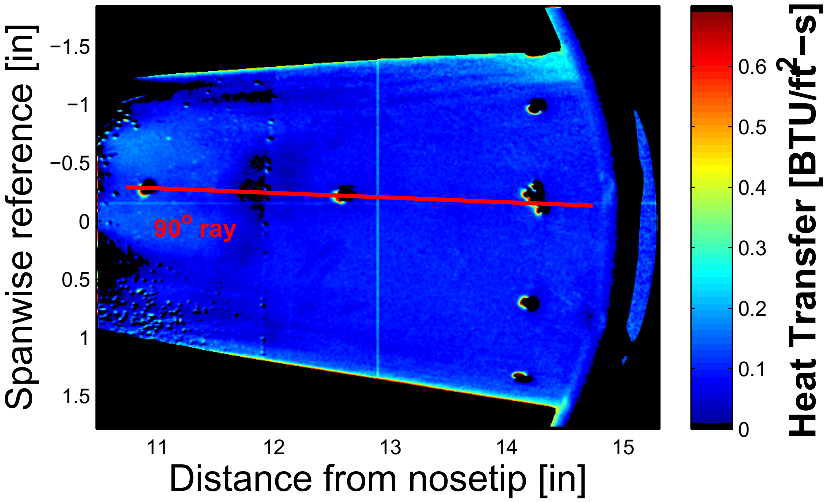

Figure 9.22. Heat transfer profile of E6R33. 3°AoA, quiet flow, smooth surface, Kulite array near the 90° ray. $Re = 3.63x10^6/ft$, $P_o = 153.0$ psia, $T_o = 294.5$°F, $T_w = 95.7$°F.

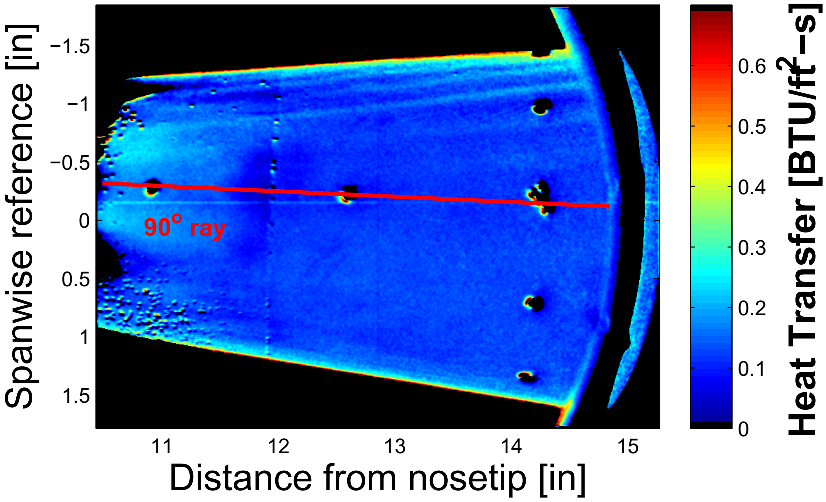

Figure 9.23. Heat transfer profile of E6R34. 3°AoA, quiet flow, Torlon insert, Kulite array near the 90° ray. $Re = 3.63x10^6/ft$, $P_o = 158.5$ psia, $T_o = 310.2$°F, $T_w = 82.4$°F.

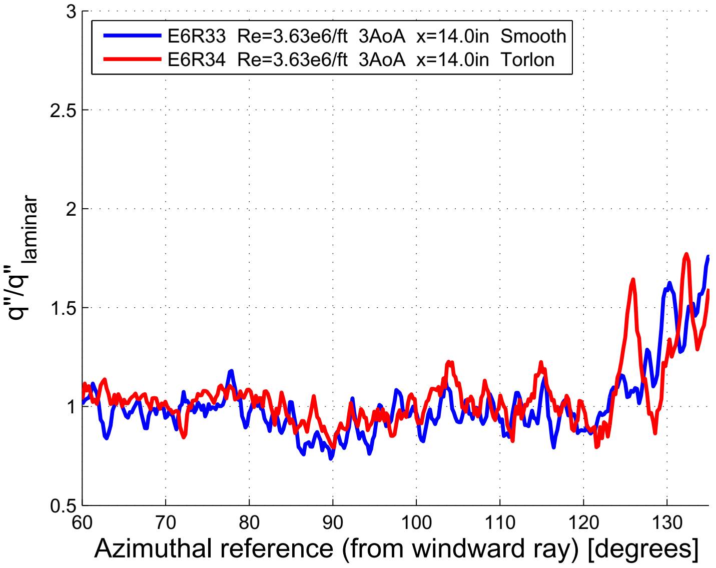

Figure 9.24. Spanwise heat transfer profile of E6R33 (smooth surface) and E6R34 (Torlon insert) at $x = 14.0$-in, 3°AoA, quiet flow.

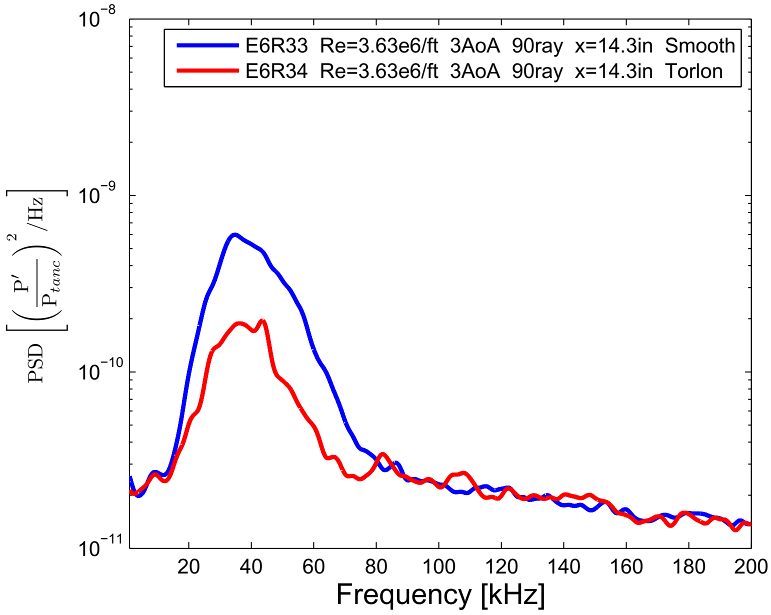

Figure 9.25. PSD of E6R33 (smooth surface) and E6R34 (torlon insert) for cone at 3°AoA under quiet flow. Kulite at 90° ray and $x = 14.3$-in.

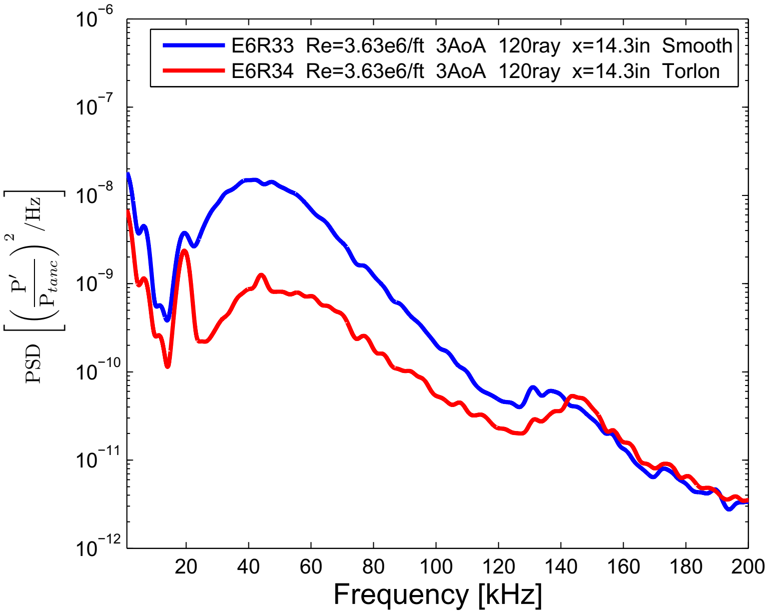

Figure 9.26. PSD of E6R33 (smooth surface) and E6R34 (torlon insert) for cone at 3°AoA under quiet flow. PCB at 120° ray and $x = 14.3$-in.

Most cases at 4° angle of attack with the Torlon insert yielded inconclusive results. Large vortices were observed crossing over sensors of interest causing turbulent spectra. Only two Torlon insert cases could be compared to smooth cases at 4° angle of attack. Figures 9.27 and 9.28 are shown as temperature difference contours. The heat transfer contour for E6R3 could not be computed due to a failure in a SB gauge. A vortex is observed crossing over the Kulite sensor at the 94.5° ray for smooth and Torlon cases. The Torlon case showed a larger vortex over the same position. The traveling-wave amplitudes for this Kulite were smaller when the Torlon insert was installed, as shown in Figure 9.29.

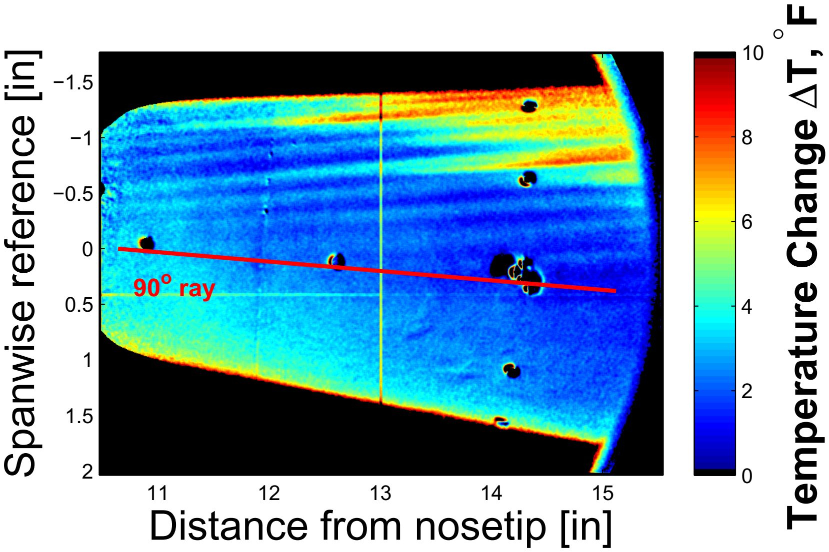

Figure 9.27. Temperature difference contour of E5R1. 4°AoA, quiet flow, smooth surface, Kulite array near the 90° ray. $Re = 3.69x10^6/ft$, $P_o = 157.6$ psia, $T_o = 300.3$°F, $T_w = 90.4$°F.

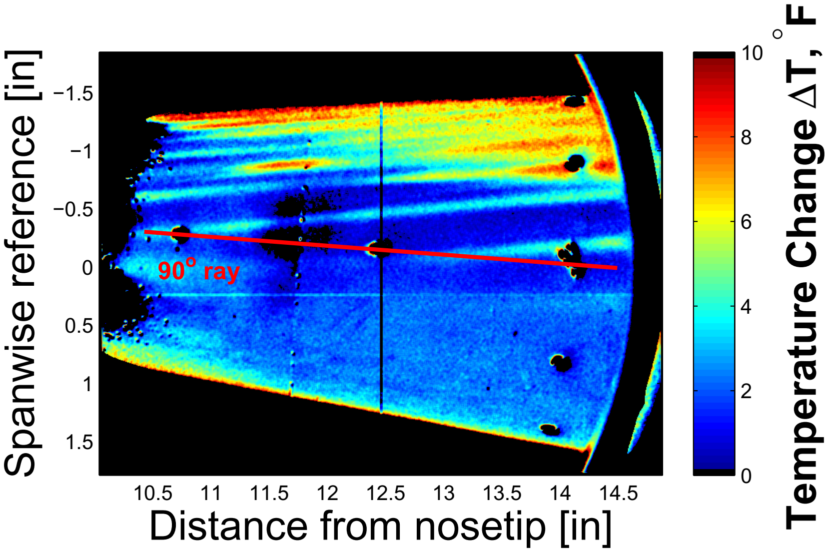

Figure 9.28. Temperature difference contour of E6R1. 4°AoA, quiet flow, Torlon insert, Kulite array near the 90° ray. $Re = 3.70x10^6/ft$, $P_o = 150.4$ psia, $T_o = 277.8$°F, $T_w = 77.5$°F.

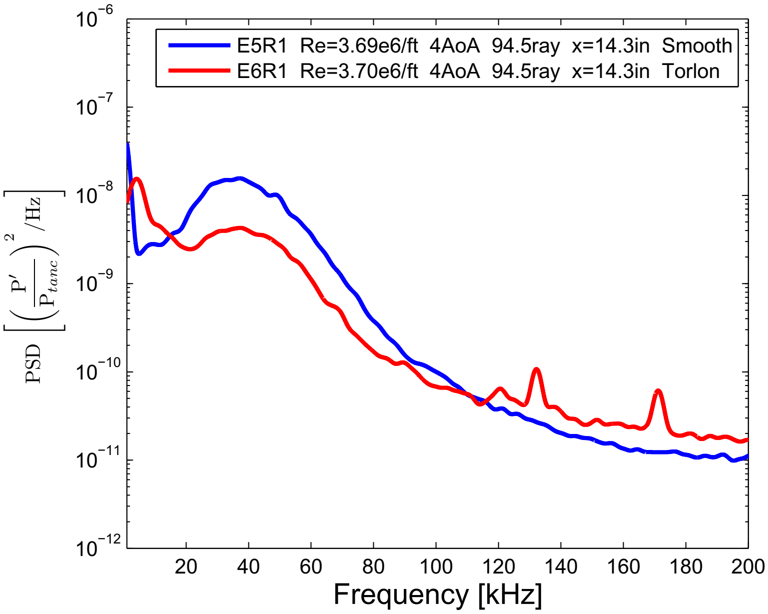

Figure 9.29. PSD of E5R27 (smooth surface) and E6R3 (Torlon insert) for cone at 4°AoA under quiet flow. Kulite at 94.5° ray and $x = 14.3$-in.

9.3 Interaction Analysis

An analysis was conducted to compare traveling-wave amplitudes with the local heat flux observed near the sensor that detects the traveling waves. The traveling-wave amplitudes for each case were obtained by integrating the spectra from 20 to 80 kHz. The results are listed in Table 9.1. The amplitude of the traveling waves shows a decrease when roughness is added.

Table 9.1 Smooth and added roughness effects on traveling-wave amplitude. PSDs integrated from 20 to 80 kHz. All runs at $Re = 3.62 \pm 0.04{\times}10^6$/ft.

Entry	Run	AoA	Ray	$q''/q''_{laminar}$	P'/P_{tanc}	Surface
[−]	[−]	[degree]	[degree]	[−]	[−]	[−]
4	1	4	87.75	1.56	0.013	Smooth
4	29	4	87.75	1.98	0.003	E4 Roughness ring
4	1	4	92.25	1.53	0.023	Smooth
4	29	4	92.25	1.17	0.006	E4 Roughness ring
5	1	4	94.5	-	0.021	Smooth
6	1	4	94.5	-	0.012	Torlon insert
6	33	3	90	0.84	0.004	Smooth
6	34	3	90	0.99	0.002	Torlon insert
6	33	3	120	0.97	0.022	Smooth
6	34	3	120	1.11	0.006	Torlon insert

When comparing the heat-flux values directly to the RMS fluctuations an inverse trend can be observed, but the heat flux at the sensor may not yield the true relationship between the stationary and traveling waves. An improved analysis was used for comparison by noting the location of the vortices relative to the sensors. Table 9.2 compares the matching smooth and rough cases and shows the percent reduction of the traveling-wave amplitudes while describing the vortex positions. Each pair of runs showed a reduction of at least 40% in traveling-wave amplitudes after applying roughness. Larger reductions in the amplitudes occurred when a vortex was observed to be within 5° of the pressure sensor that detected the waves.

Table 9.2 Matching smooth and added-roughness runs to compare traveling-wave amplitudes.

Entry [−]	Run [−]	AoA [degree]	Ray [degree]	Amplitude [% Reduction]	Vortex location in roughness case [−]
6	33 & 34	3	90	42.5	No vortex near sensor
6	33 & 34	3	120	72.0	Vortex passing over sensor
4	1 & 29	4	87.75	79.6	Vortex passing over sensor
4	1 & 29	4	92.25	75.2	Vortices at ±3° of sensor.
5 & 6	1 & 1	4	94.5	42.9	Larger vortex over sensor

10. POSSIBLE SECONDARY INSTABILITY OF THE STATIONARY CROSSFLOW VORTICES

Fluctuations were found in PCB and Kulite PSDs that were higher in frequency than was expected for the traveling crossflow and second-mode disturbances. These fluctuations were only found using sensors that had vortex streaks crossing over them. These characteristics suggest they may be caused by the secondary instability of the stationary crossflow instability.

10.1 High-frequency Instability Cases

10.1.1 Disturbances near the 60° and 95° rays at 4° AoA

A comparison of smooth and rough surfaces was conducted during entry 4 at 4° AoA. Tests E4R1 and E4R29 were compared at matching Reynolds number. The roughness ring applied for E4R29 showed new vortex streaks (Figure 10.2) as compared to the smooth case (Figure 10.1).

Axial heat transfer profiles were taken over the path a vortex streak spanned along the cone. The profiles were averaged over each pixel in the spanwise direction. The number of post-binned pixels averaged depended on the width of a vortex streak, where the edges were determined when the heat flux began to show constant values below the peak. Figure 10.3 shows axial profiles of the vortex streaks that crossed over the pressure sensors at the 60° and 95° ray along with the a smooth case axial profile taken on the 95° ray. The heat transfer was normalized by the theoretical laminar heat transfer for a 7° half-angle cone at zero angle of attack.

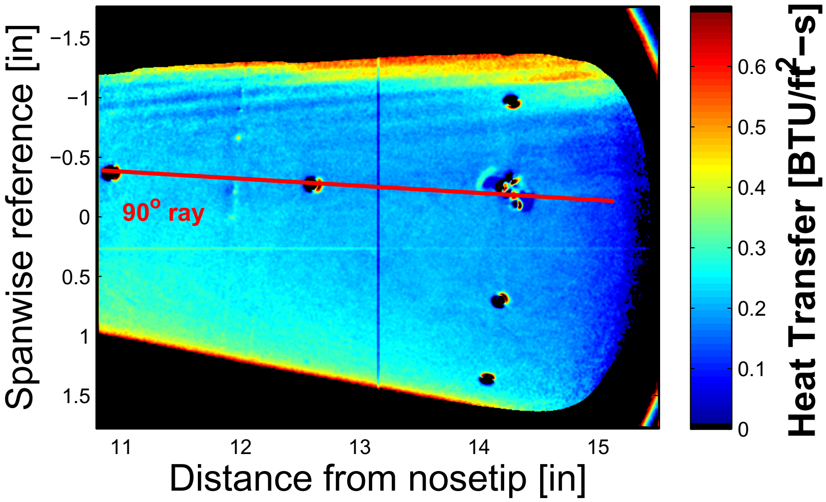

Figure 10.1. Heat transfer contour of E4R1. 4°AoA, quiet flow, smooth surface, Kulites near the 90° ray. $Re = 3.66{\times}10^6$/ft, $P_o = 156.8$ psia, $T_o = 301.7$°F, $T_w = 74.6$°F.

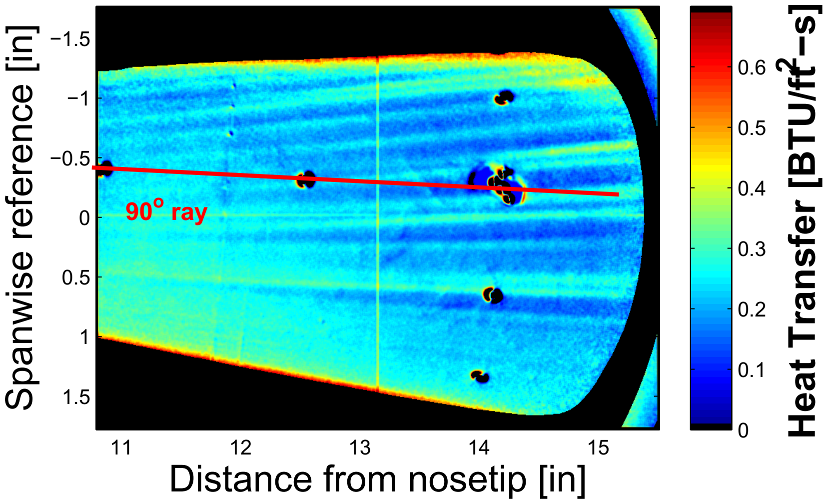

Figure 10.2. Heat transfer contour of E4R29. 4°AoA, quiet flow, E4 roughness ring, Kulites near the 90° ray. $Re = 3.66{\times}10^6$/ft, $P_o = 157.1$ psia, $T_o = 302.1$°F, $T_w = 76.8$°F.

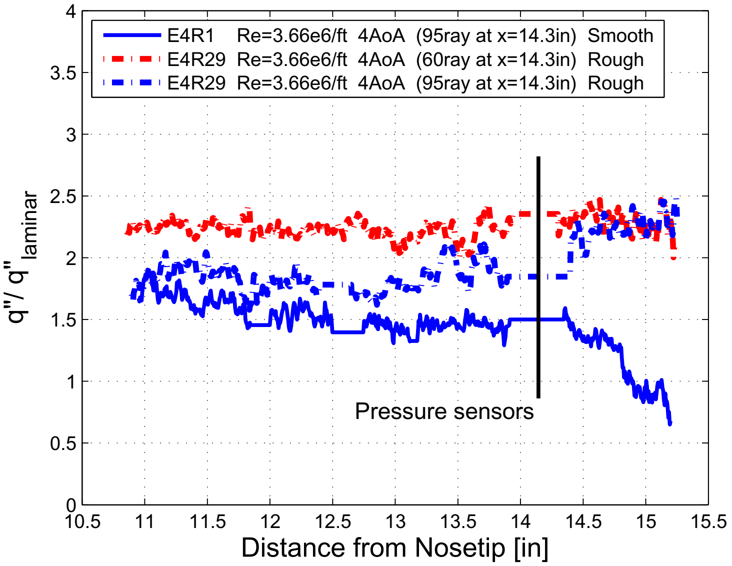

Figure 10.3. Axial heat transfer profile of E4R1 and E4R29.

The PCB sensor at the 60° ray was found to have a vortex streak above it. The PSD of this PCB sensor over these two runs, shown in Figure 10.4, shows a 475 kHz peak in the vortex-streak case. The rest of the frequency spectra remains the same between the two cases. This may be a secondary instability of the stationary vortex.

A vortex was also observed to cross on the leeside edge of Kulite Array 2, approximately at the 95° ray in Figure 10.2. Figure 10.5 shows the spectra for three Kulites in Kulite Array 2, along with the spectra for the PCB sensor at the 60° ray. The Kulite at the 90° ray does not detect the disturbance, but at the 92.25° ray a small peak was found near 410 kHz and at 94.5° the peak is two orders of magnitude higher. Note that the frequency is higher at the ray closer to the windward ray. The vortex position over these Kulites also suggest the high-frequency disturbances are the secondary instability of the stationary mode of crossflow.

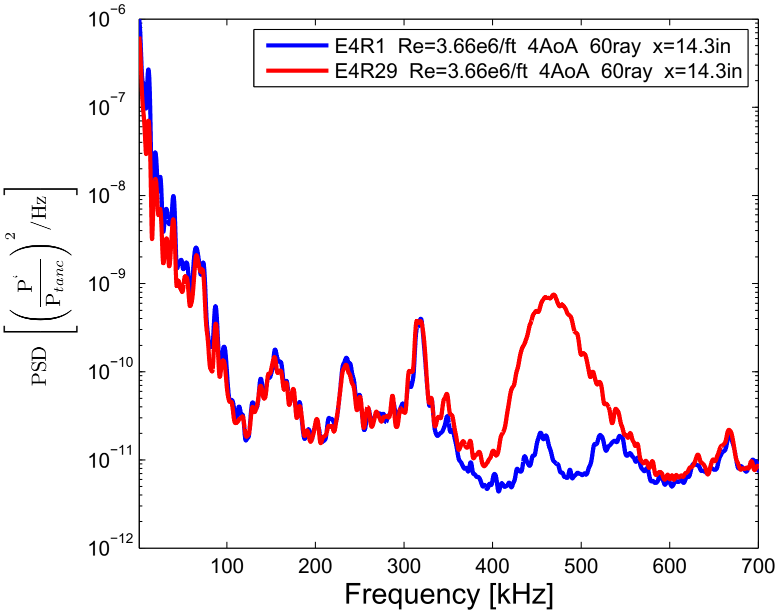

Figure 10.4. PSD comparison of E4R1 (blue) with smooth surface and E4R29 (red) with E4 roughness ring. Both spectra from PCB sensor at $x = 14.3$-in. on the 60° ray.

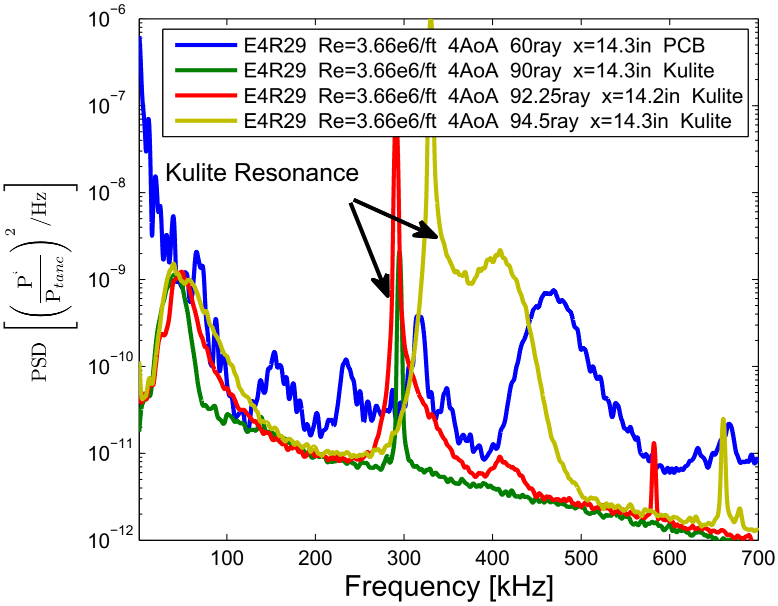

Figure 10.5. PSD of E4R29 with E4 roughness ring under quiet flow for a cone at 4° AoA. Spectra of PCB and Kulite sensors where crossflow vortices are breaking down over sensor positions.

10.1.2 Disturbances near the 120° ray at 4° AoA

A high-frequency PSD peak was discovered for E6R2 at $x = 14.3$-in for 4° AoA on the 120° ray. A vortex streak in Figure 10.6 is seen passing over the PCB sensor at the 120° ray. Another streak is observed passing over the Kulite array, but no disturbances were detected. The figure is displayed as the temperature gradient referenced from the model temperature due to a failure in a SB gauge. Figure 10.7 shows the spectra of the PCB sensor, with a high-frequency peak near 410 kHz. Another peak near 40-50 kHz is most likely the traveling mode of the crossflow instability.

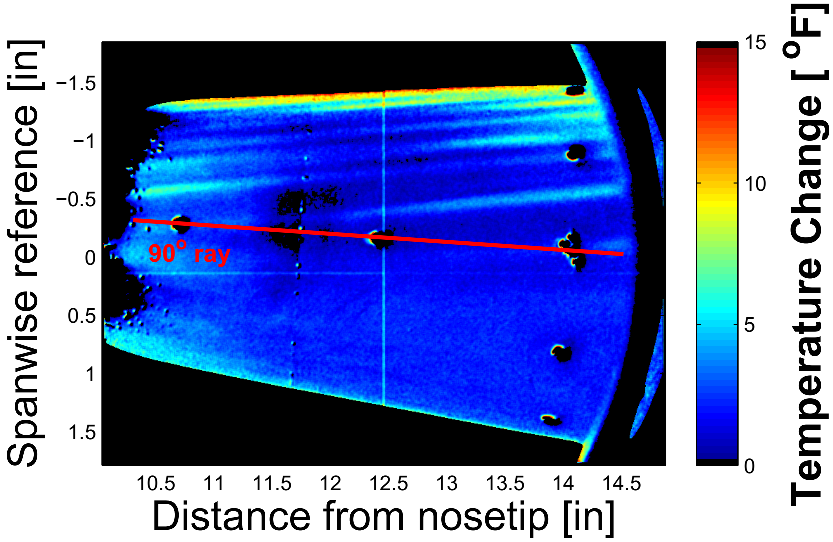

Figure 10.6. Temperature difference contour of E6R2. 4°AoA, quiet flow, Torlon insert, Kulite array on the 90° ray. $Re = 3.27{\times}10^6$/ft, $P_o = 136.8$ psia, $T_o = 290.0$°F, $T_w = 74.6$°F.

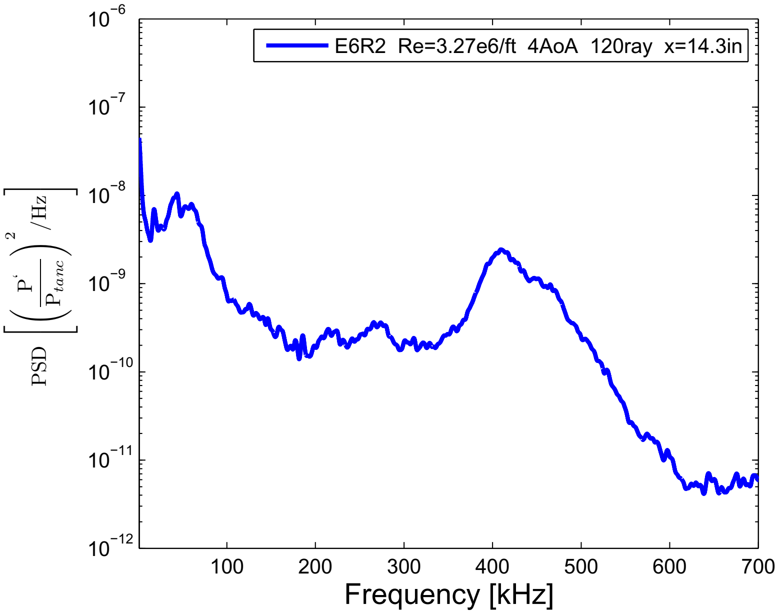

Figure 10.7. PSD comparison of E6R2 with Torlon insert. PCB sensor at $x = 14.3$-in. on the 120° ray.

Another high-frequency peak was discovered for E6R5 at $x = 14.3$-in for 4° AoA on the 120° ray. A faint vortex streak in Figure 10.8 is seen crossing over the Kulite at the 120° ray. Figure 10.9 shows the PSD of the Kulite signal (in red) with a high-frequency peak near 375 kHz. The narrow peak near 300 kHz is again the resonant frequency of the sensor. Another peak near 40 kHz is likely the traveling mode of the crossflow instability. A larger vortex streak is seen crossing over the PCB sensor on the 150° ray. The PSD of this PCB sensor shows turbulent spectra without any indication of a secondary instability. Figure 10.10 shows the axial profile of each sensor. The profile over the 120° ray shows a near-constant heat flux across the length of the cone. It is unclear if the vortex streak has saturated or is just forming. The heat-flux profile near the 150° ray shows the vortex streak growing and then saturating before crossing the PCB sensor.

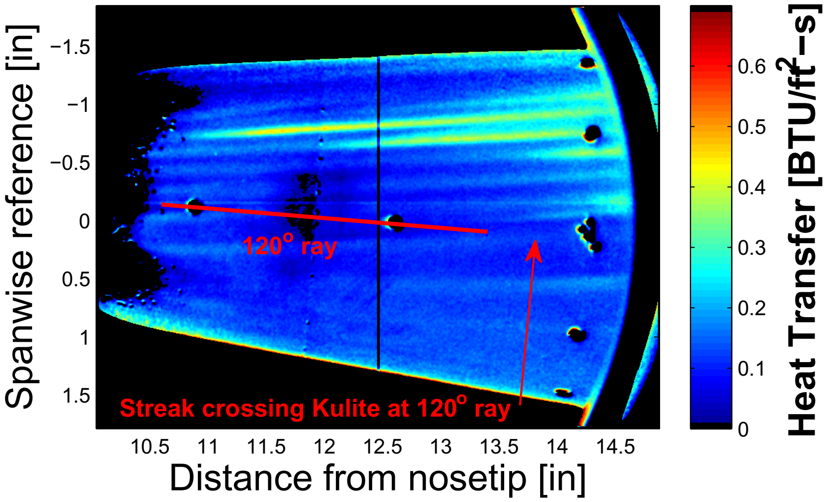

Figure 10.8. Heat transfer profile of E6R5. 4°AoA, quiet flow, Torlon insert, Kulites at the 120° ray. Re $= 3.23\times10^6$/ft, $P_o = 138.7$ psia, $T_o = 301.7$°F, $T_w = 90.9$°F.

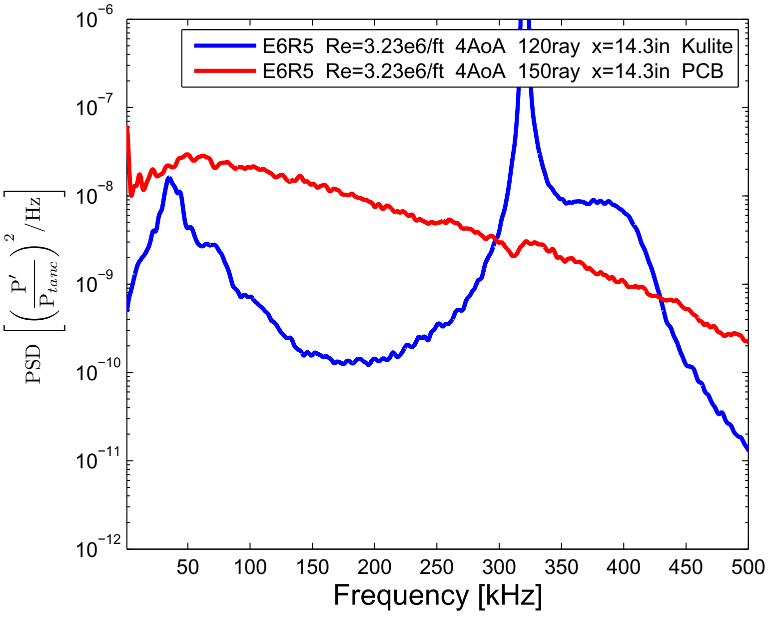

Figure 10.9. PSD of E6R5 with Torlon insert for cone at 4°AoA under quiet flow. Kulite sensor at the 120° ray and $x = 14.3$-in.

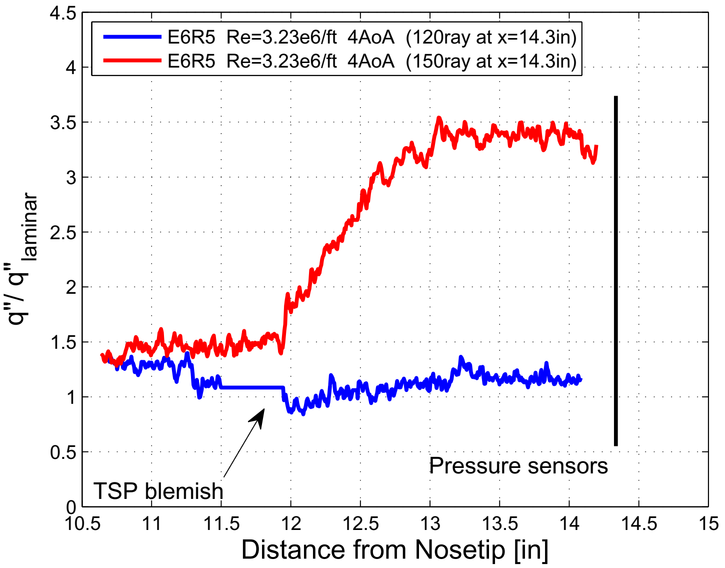

Figure 10.10. Axial heat transfer profile of E6R5 over vortex streaks at the 120° and 150° ray from windward.

10.1.3 Disturbances near the 139.5°, 150°, and 165° ray at 3° AoA

At 3° AoA, a high-frequency peak was found for E6R38 at $x = 14.3$-in on the 150° ray at 3° AoA. The leeside edge of the TSP image in Figure 10.11 marks the 150° ray where the PCB sensor detected the high-frequency disturbance. It is difficult to determine if a vortex streak has passed over the PCB sensor at the edge of the TSP image, however, streaks are observed between the 120° and 150° ray, suggesting a vortex is likely present near the 150° ray. The PSD of the PCB sensor that was positioned at the 150° ray shows a peak near 310 kHz in Figure 10.12. Another peak near 75 kHz was detected. Computations by Li et al. [41] show traveling-wave frequencies with the largest N factors near 40 kHz at 3° angle of attack. Therefore, it is unclear if this lower frequency disturbance is the traveling mode of the crossflow instability, another disturbance, or a modulated case of the traveling mode caused by other instabilities.

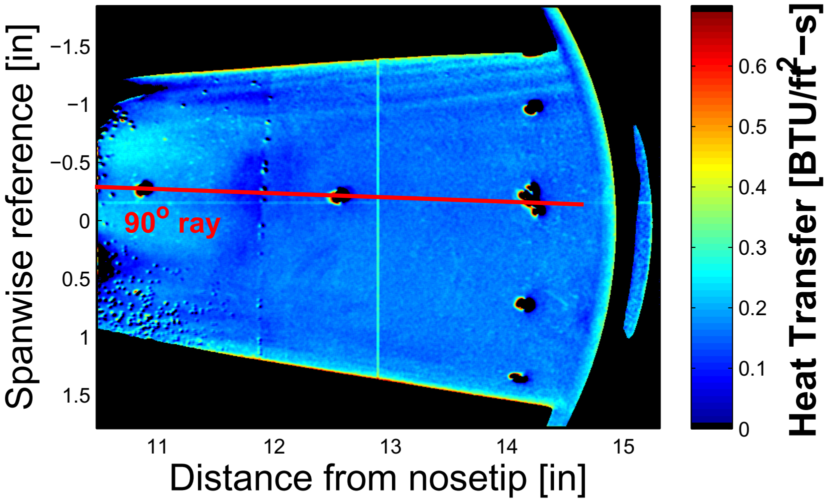

Figure 10.11. Heat transfer profile of E6R38. 3°AoA, quiet flow, Torlon insert, Kulites at 90° ray. Re = 3.33×10^6/ft, P_o = 142.1 psia, T_o = 299.3°F, T_w = 99.3°F.

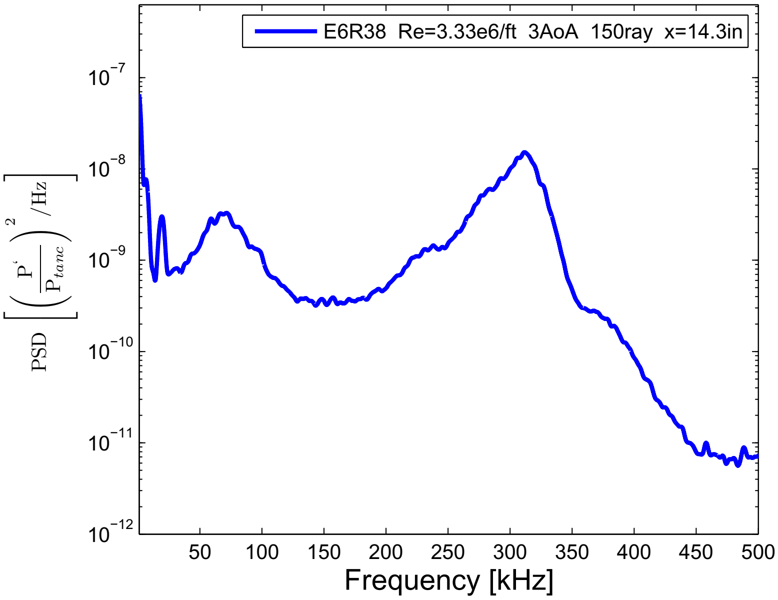

Figure 10.12. PSD of E6R38 with Torlon insert for cone at 3°AoA under quiet flow. PCB sensor at the 150° ray and x = 14.3-in.

The final high-frequency peaks were detected at $x = 14.3$-in on the 139.5° and 165° ray at 3° angle of attack. E6R43 was processed at four sequential times during the run: 0.5, 1.0, 1.5, and 1.9 seconds after the diaphragms burst. The heat transfer contours are shown for each time processed in Figures 10.13, 10.14, 10.15, and 10.16. Vortex streaks are observed crossing over the Kulite sensor at the 139.5° ray and a region of closely packed vortices crossing over the PCB sensor at the 165° ray. As the Reynolds number decreases during the run, the heat transfer over the model decreases. A decrease in the strengths of the vortex streaks were also observed.

The PSD of the PCB sensor at the 165° ray is shown in Figure 10.17. A large peak is observed that is centered near 260 kHz. The frequency was normalized by the square root of the freestream Reynolds number at $x = 14.3$-in. The magnitude and frequency of this disturbance decreases as the Reynolds number decreases. This suggests the disturbance is dependent on the boundary-layer thickness. Figure 10.18 shows the PSD of the Kulite sensor at the 139.5° ray where a peak near 325 kHz can be seen. The resonant frequency conceals most of the disturbance, but a decrease in power is observed as the Reynolds number decreases. Traveling waves are also detected near 40 kHz.

An axial heat transfer profile was computed for each vortex streak that crossed above the PCB and Kulite sensors. Figure 10.20 shows the axial profile of the streak that crosses the Kulite sensor at the 139.5° ray. All four Reynolds number cases show an increase in heat flux with distance from the nosetip approaching the Kulite sensor at $x = 14.3$-in. As expected from the heat transfer contours, the heat flux over the profile decreases as the Reynolds number decreases. Figure 10.19 shows the axial profile of the streak that crosses the PCB sensor at the 165° ray. The same trends are observed with the vortex streak over the 165° ray. The highest Reynolds number case showed a greater increase in heat flux near the PCB sensor at $x = 14.3$-in.

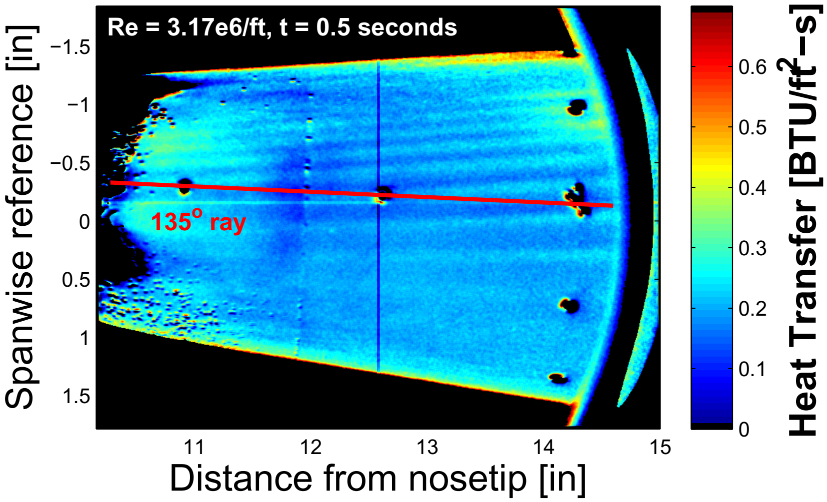

Figure 10.13. Heat transfer profile of E6R43. 3°AoA, quiet flow, Torlon insert, Kulites near the 135° ray. Re = 3.17×10^6/ft, P_o = 143.6 psia, T_o = 327.6°F, T_w = 84.4°F.

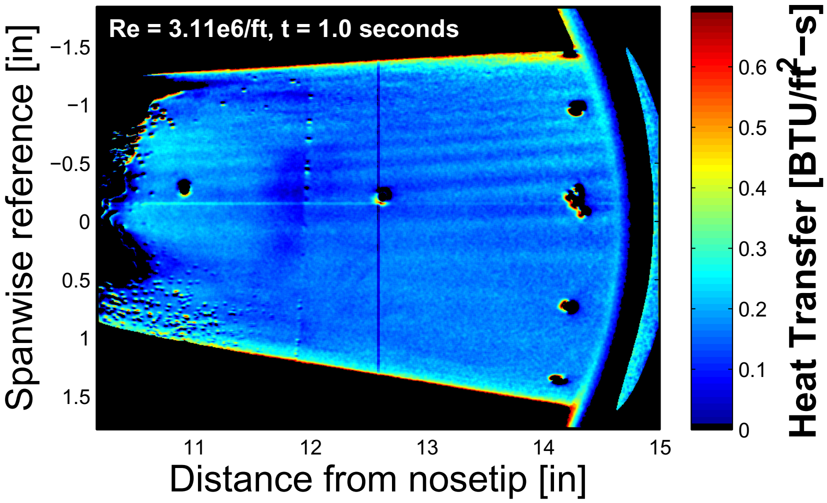

Figure 10.14. Heat transfer profile of E6R43. 3°AoA, quiet flow, Torlon insert, Kulites near the 135° ray. Re = 3.11×10^6/ft, P_o = 138.7 psia, T_o = 319.8°F, T_w = 84.4°F.

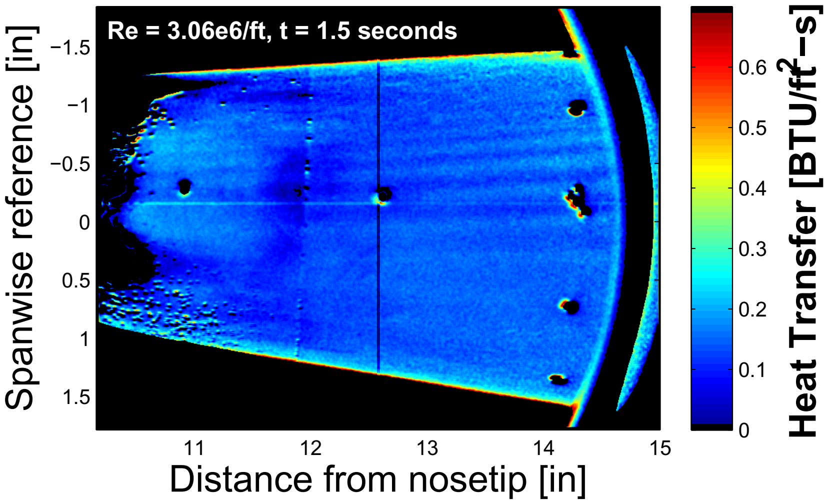

Figure 10.15. Heat transfer profile of E6R43. 3°AoA, quiet flow, Torlon insert, Kulites near the 135° ray. Re = 3.06×10^6/ft, P_o = 134.3 psia, T_o = 312.6°F, T_w = 84.4°F.

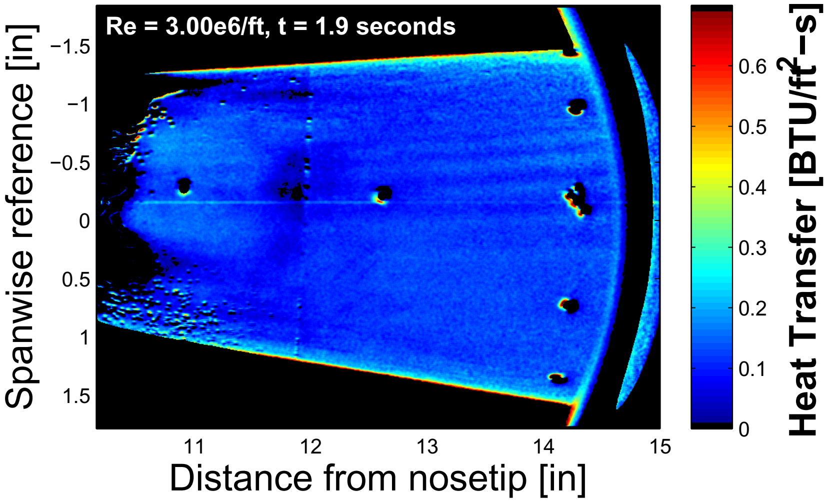

Figure 10.16. Heat transfer profile of E6R43. 3°AoA, quiet flow, Torlon insert, Kulites near the 135° ray. Re = 3.00×10^6/ft, P_o = 129.9 psia, T_o = 305.3°F, T_w = 84.4°F.

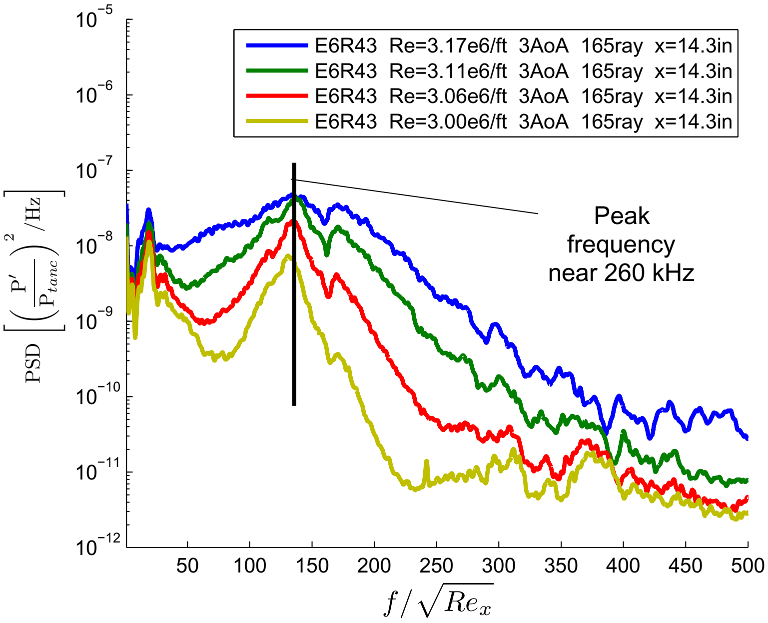

Figure 10.17. PSD of E6R43 over a range of Reynolds numbers with Torlon insert for cone at 3°AoA under quiet flow. PCB sensors at $x = 14.3$-in.

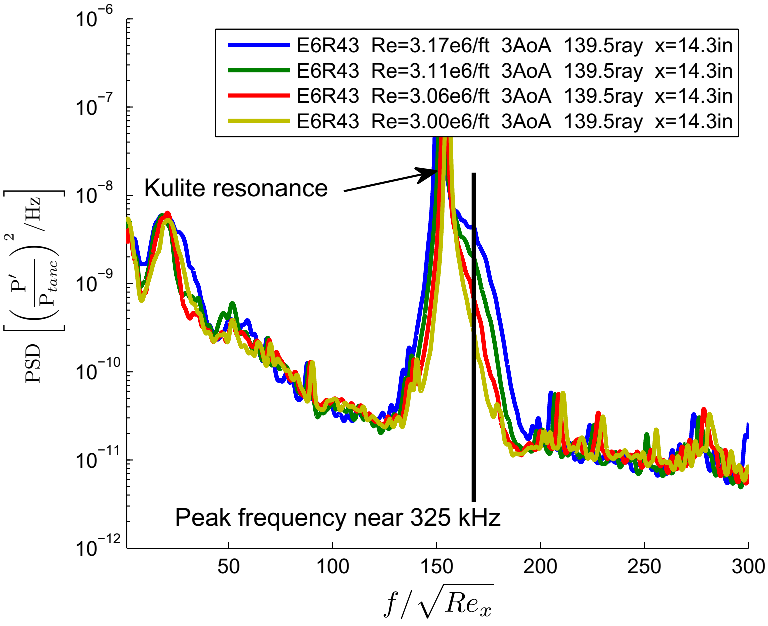

Figure 10.18. PSD of E6R43 over a range of Reynolds numbers with Torlon insert for cone at 3°AoA under quiet flow. Kulite sensors at $x = 14.3$-in.

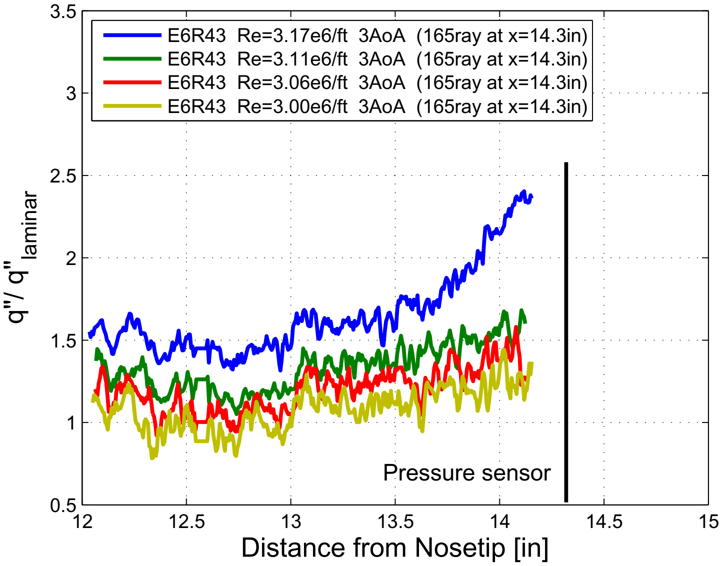

Figure 10.19. Axial heat transfer profile of E6R43. Profile along vortex streak crossing over PCB sensor at the 165° ray.

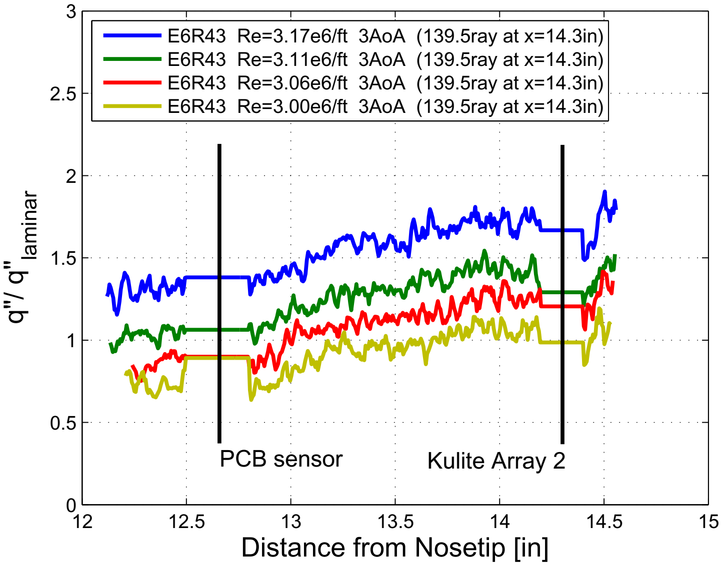

Figure 10.20. Axial heat transfer profile of E6R43. Profile along vortex streak crossing over Kulite sensor at the 139.5° ray.

10.2 Runs with Vortices over Pressure Sensors without High-Frequency Disturbances

Most tests that revealed vortices over PCB or Kulite sensors did not detect high-frequency disturbances. Some cases have been shown previously in this section. Four additional tests show similar results. Figure 10.21 shows E3R5 where a vortex streak is observed crossing the PCB sensor at $x = 14.3$-in on the 120° ray. Figure 10.22 shows E3R4 where a region of streaks are observed crossing the same PCB sensor. Figure 10.23 shows E5R20 where vortex streaks are observed crossing a Kulite sensor near the 124.5° ray and a PCB sensor on the 150° ray. Figure 10.24 shows the last test, E5R21, where vortex streaks are breaking down in front of the PCB sensor on the 150° ray. The PSD of the PCB sensors mentioned show turbulent spectra in Figure 10.25. All four cases show varying levels of a vortex's strength crossing over a pressure sensor, but high-frequency disturbances were not measured in any case. The secondary instability could have occured upstream in these cases.

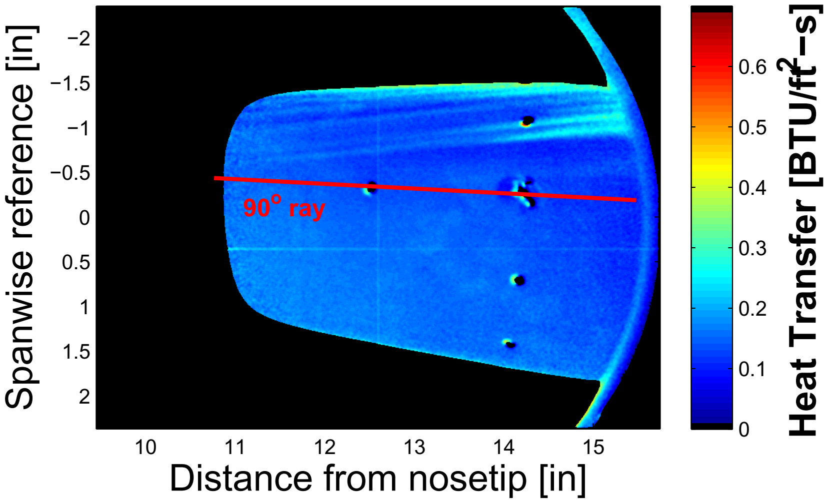

Figure 10.21. Heat transfer profile of E3R5. 3°AoA, quiet flow, smooth case, Kulites near the 90° ray. Re = 3.41×10^6/ft, $P_o = 139.6$ psia, $T_o = 281.8$°F, $T_w = 84.4$°F.

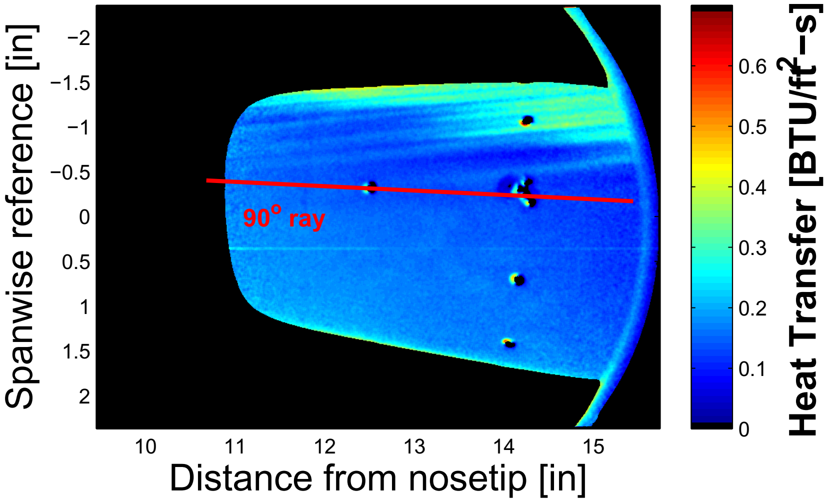

Figure 10.22. Heat transfer profile of E3R4. 3°AoA, quiet flow, smooth case, Kulites near the 90° ray. Re = 3.86×10^6/ft, $P_o = 157.4$ psia, $T_o = 279.2$°F, $T_w = 84.4$°F.

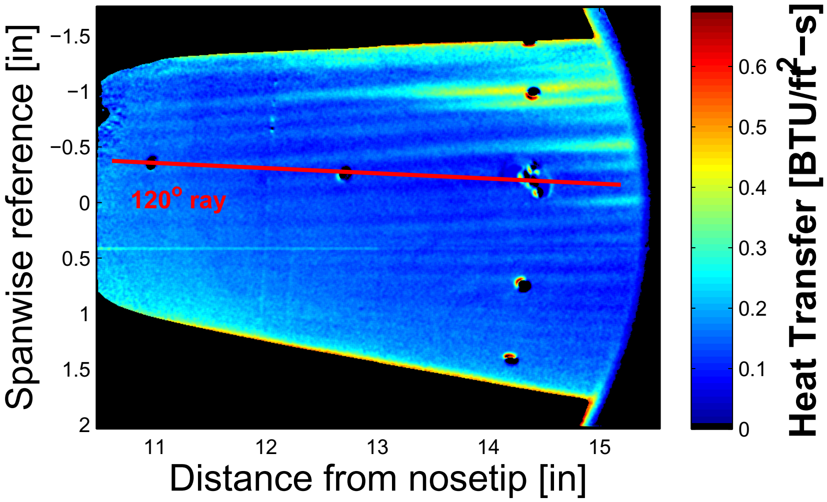

Figure 10.23. Heat transfer profile of E5R20. 3°AoA, quiet flow, E5 Roughness 2, Kulites near the 120° ray. Re $= 3.28\times10^6$/ft, $P_o = 139.7$ psia, $T_o = 298.3$°F, $T_w = 84.4$°F.

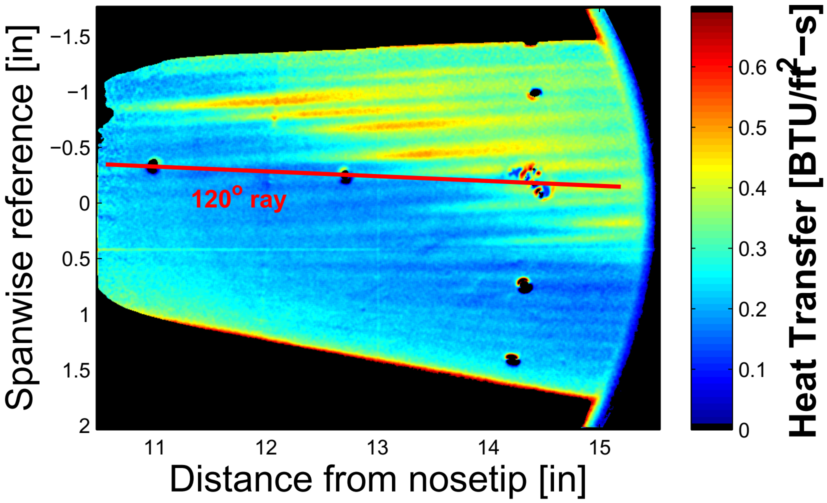

Figure 10.24. Heat transfer profile of E5R21. 3°AoA, quiet flow, E5 Roughness 2, Kulites near the 120° ray. Re $= 3.71\times10^6$/ft, $P_o = 157.8$ psia, $T_o = 297.8$°F, $T_w = 84.4$°F.

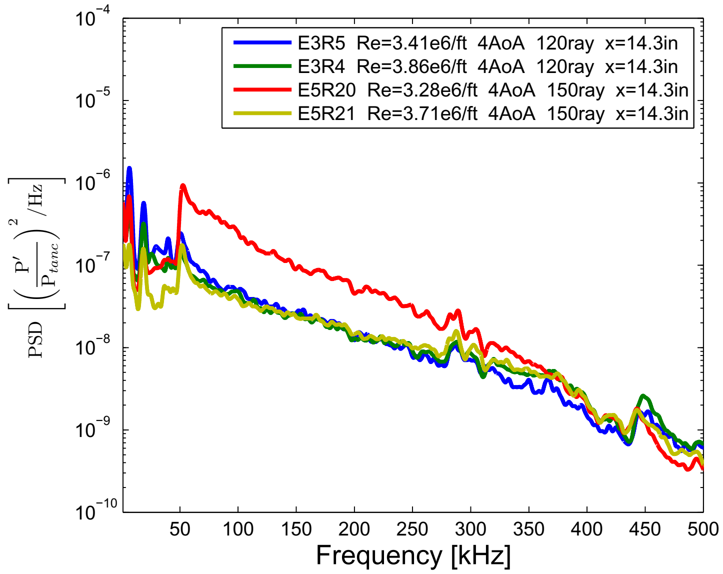

Figure 10.25. PSD of E3R4, E3R5, E5R20, and E5R21. Spectra taken from PCB sensor at $x = 14.3$-in.

10.3 Disturbance Analysis

The data from a few tests found high-frequency disturbances in power spectra where vortices were seen crossing a pressure sensor. The cause of the appearance in the few cases is not known. The author speculates that the entries where the disturbances were found, entry 4 and 6, used additional roughnesses. The disturbances are observed where the amplitudes of the stationary waves are growing, but not after the waves have saturated. This observation is counter to what is generally seen in past low-speed experiments and computations. A larger collection of conditions should be tested to understand these high-frequency disturbances.

Figure 10.26 shows the disturbance frequencies as a function of the ray angle. The plot reveals an inverse relationship between the ray angle and disturbance frequency for rays nearer the lee side. This could be due to the larger boundary layer thickness approaching the lee ray. The data from each run were compiled in Table 10.1. The heat flux near each pressure sensor and the RMS pressure fluctuations of the disturbances were also tabulated. The Reynolds number and angle of attack were also varied within these experiments. No clear trends could be determined from the heat transfer and RMS pressure fluctuations.

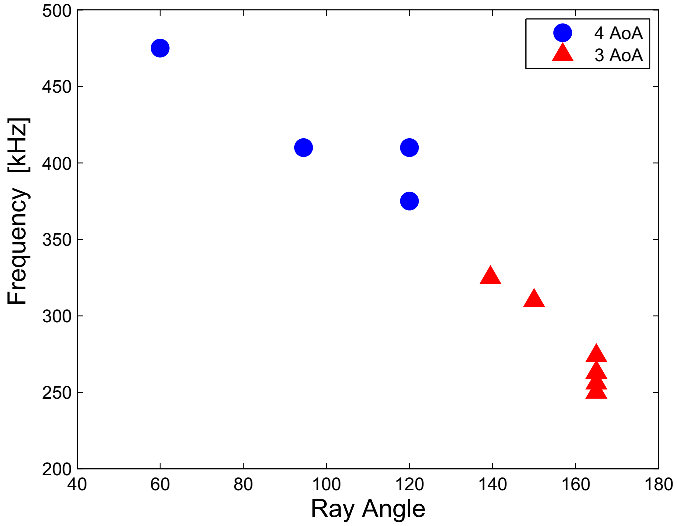

Figure 10.26. Disturbance frequencies as a function of the ray angle with respect to the windward ray. All disturbances detected at $x =$ 14.3-in.

Table 10.1 Disturbance properties for all tests with possible secondary instabilities. All sensors at $x = 14.3$-in. Asterisk denotes Kulite sensors where the frequency response past 60 kHz is not known.

Entry [−]	Runs [−]	Re [$\times 10^6$/ft]	AoA [degree]	Ray [degree]	Frequency [kHz]	$q''/q''_{laminar}$ [−]	P'/P_{tanc} [−]
4	29	3.66	4	60.0	475	1.86	0.006
4	29	3.66	4	94.5	410	1.57	0.011*
6	2	3.27	4	120.0	410	-	0.013
6	5	3.23	4	120.0	375	1.17	0.023*
6	43	3.17	3	139.5	325	1.50	0.012*
6	38	3.33	3	150.0	310	2.09	0.026
6	43	3.17	3	165.0	274	2.07	0.092
6	43	3.11	3	165.0	263	1.29	0.065
6	43	3.06	3	165.0	256	1.14	0.038
6	43	3.00	3	165.0	250	0.93	0.022

11. CONCLUSIONS AND FUTURE WORK

11.1 Conclusions

A 7° half-angle cone was positioned at low angles of attack to observe crossflow effects in a Mach 6 quiet tunnel. The stationary and traveling crossflow instabilities were examined as well as the interaction between them. Temperature sensitive paint was used to quantify inferred heat transfer into the model. PCB and Kulite pressure sensors were used to detect disturbances on the surface of the model.

The cones was placed at zero angle of attack to set a baseline for comparing to inclined positions. Under quiet flow conditions, the second-mode instability was found to have a frequency near 275 kHz at $x = 14.3$-in. for $Re = 3.67\times10^6$/ft. Similar tests were performed for noisy tunnel conditions. Under noisy flow conditions, the second-mode amplitudes were at least an order of magnitude larger than under quiet flow and shifted to slightly higher frequencies at comparable Reynolds numbers. Pate's correlation, used for predicting boundary-layer transition under noisy flow, agreed within the experiment's uncertainty.

The stationary mode was observed as streaks of increased heat flux. The streaks grew axially and curved to the lee of the cone. The strength of these high-heat transfer streaks were generally larger at higher Reynolds number. Heat-flux profiles for each entry were compared, to show the effects of the paint roughness. The proximity of the stationary waves to pressure sensors suggests the location of the vortices has an effect on the traveling-wave amplitudes.

The traveling crossflow mode was detected using Kulite and PCB pressure transducers. Traveling waves were found between the 90° and 150° rays at 2°, 3°, and 4° angle of attack. At $x = 14.3$-in the frequency of the traveling waves was between 40-50 kHz under quiet flow for unit Reynolds numbers between 1.97×10^6/ft and

3.81×10^6/ft. The amplitude of the traveling waves increased with Reynolds number and angle of attack. The wave angle and phase speed were calculated through cross correlations between nearby sensors. The typical wave traveled at a 60° angle from lee to wind. Typical phase speeds were near 1000 ft/s. Under noisy flow, a disturbance was detected at 20-30 kHz for Reynolds numbers near 2.00×10^6/ft. Due to the low frequency of the disturbance, the disturbance can be mistaken for noise. However, a wave analysis shows the disturbance has similar wave angles and phase speeds as observed from traveling waves under quiet flow. More data should be collected to confirm this.

The interaction of the stationary and traveling modes of crossflow was quantified by measuring the heat transfer from the stationary vortices near pressure sensors and the amplitudes of the traveling waves. Nail-polish and Torlon-insert roughnesses were successful in altering the vortex streaks observed under quiet flow conditions.

The secondary instability of the stationary mode was apparently discovered during testing. A high-frequency disturbance was found between 300-500 kHz only when a stationary vortex crossed over the sensor. The vortices that passed over the sensor generally had little growth, suggesting the disturbances arise before the rapid growth and saturation of the vortices. The disturbance's frequency decreased with increasing azimuthal angle.

11.2 Future Work

Many more experiments should be conducted to provide additional insight into the mechanisms that govern crossflow-related laminar-to-turbulent boundary-layer transition.

Traveling waves were analyzed at $x = 14.3$-in between the 90° and 120° rays. Additional axial positions for the Kulite sensors should be tested to further define the traveling waves. Kulite Array 1 or new ports along a ray should be used to compare the amplitudes of the traveling waves. The growth rates of the traveling mode could then be examined. A larger database of traveling-wave amplitudes as a function of the Reynolds number and wall temperature should also be developed. Such data might help to explain the effects that each variable has on the traveling waves.

Additional studies of the stationary-traveling mode interaction should also be conducted. The cases tested used Reynolds numbers that were too high to observe traveling waves to the lee of the 120° ray. Lower Reynolds number cases can be tested so the interaction can be observed closer to the lee ray.

The most important recommendation for future work is focused on the high-frequency disturbances, which seem likely to be the secondary instability of stationary crossflow waves. Using the Torlon insert, the vortices along the cone are fixed. PCB sensors should be positioned in a line, azimuthally, to detect when high-frequency disturbances appear and break down. By varying the Reynolds number, the growth and saturation regions of the vortices can be made to pass over this PCB array. The development of these disturbances could help define a transition Reynolds number for crossflow-related flows.

LIST OF REFERENCES

LIST OF REFERENCES

[1] J.J. Bertin and R.M. Cummings. Fifty Years of Hypersonics: Where We've Been, Where We're Going. *Progess in Aerospace Sciences*, 39:511–536, 2003.

[2] K.E. Wurster. An Assessment of the Impact of Transition on Advanced Winged Entry Vehicle Thermal Protection System Mass. AIAA Paper 1981-1090, June 1981.

[3] S.P. Schneider. Developing Mechanism-Based Methods for Estimating Hypersonic Boundary-Layer Transition in Flight: The Role of Quiet Tunnels. AIAA Paper 2013-2608, June 2013.

[4] E. Reshotko. Transition Issues at Hypersonic Speeds. AIAA Paper 2006-707, January 2006.

[5] J.L. van Ingen. A Suggested Semi-empirical Method for the Calculation of the Boundary Layer Transition Region. Technical Report VTH-74, TU Delft, September 1956.

[6] S.P. Schneider. Effects of High-Speed Tunnel Noise on Laminar-Turbulent Transition. *Journal of Spacecraft and Rockets*, 38(3):323–333, May–June 2001.

[7] S.P. Schneider. Development of Hypersonic Quiet Tunnels. *Journal of Spacecraft and Rockets*, 45(4):641–664, August 2008.

[8] D.C. Reda. Boundary-Layer Transition Experiments on Sharp, Slender Cones in Supersonic Free Flight. *AIAA Journal*, 17(8):803–810, August 1979.

[9] E. White and W.S. Saric. Secondary Instability of Crossflow Vortices. *Journal of Fluid Mechanics*, 525:275–308, 2005.

[10] J.C. Adams Jr. and W.R. Wartindale. Engineering Analysis of Hypersonic Lifting Body Windward Surface Inviscid and Viscous Flowfields at High Angles of Attack. AIAA Paper 1973-637, July 1973.

[11] J.J. Kuehl, E. Perez, and H.L. Reed. JoKHeR: NPSE Simulations of Hypersonic Crossflow Instability. AIAA Paper 2012-0921, January 2012.

[12] J.E. Gronvall, H.B. Johnson, and G.V. Candler. Hypersonic Three-Dimensional Boundary Layer Transition on a Cone at Angle of Attack. AIAA Paper 2011-3561, June 2011.

[13] W.S. Saric and H.L. Reed. Supersonic Laminar Flow Control on Swept Wings Using Distributed Roughness. AIAA Paper 2002-0147, January 2002.

[14] M.R. Malik, F. Li, and C.-L. Chang. Crossflow disturbances in three-dimensional boundary layers: nonlinear development, wave interaction and secondary instability. *Journal of Fluid Mechanics*, 268:1–36, 1994.

[15] M.P. Borg, R.L. Kimmel, and S. Stanfield. Traveling Crossflow Instability for HIFiRE-5 in a Quiet Hypersonic Wind Tunnel. AIAA Paper 2013-2737, June 2013.

[16] F. Muñoz, D. Heitmann, and R. Radespiel. Instability Modes in Boundary Layers of an Inclined Cone at Mach 6. AIAA Paper 2012-2823, June 2012.

[17] M. Högberg and D. Henningson. Secondary Instability of Cross-flow Vortices in Falkner-Skan-Cooke Boundary Layers. *Journal of Fluid Mechanics*, 368:339–357, 1998.

[18] M.R. Malik, F. Li, M.M. Choudhari, and C.-L. Chang. Secondary Instability of Crossflow Vortices and Swept-wing Boundary-layer Transition. *Journal of Fluid Mechanics*, 399:85–115, 1999.

[19] P. Wassermann and M. Kloker. Mechanisms and Passive Control of Crossflow-vortex-induced Transtion in a Three-dimensional Boundary Layer. *Journal of Fluid Mechanics*, 456:49–84, 2002.

[20] J.D. Swearingen and R.F. Blackwelder. The Growth and Breakdown of Streamwise Vortices in the Presence of a Wall. *Journal of Fluid Mechanics*, 182:255–290, 1987.

[21] L.M. Mack. Boundary Layer Linear Stability Theory. *Special Course on Stability and Transition of Laminar Flow*, pages 3.1–3.81, June 1984. AGARD-R-709.

[22] L.M. Mack. On the Inviscid Acoustic-Mode Instability of Supersonic Shear Flows. *Theoretical and Computational Fluid Dynamics*, 2(2):97–123, March 1990.

[23] R.L. Kimmel. Aspects of Hypersonic Boundary-Layer Transition Control. AIAA Paper 2003-772, January 2003.

[24] A. Fedorov. Transition and Stability of High-Speed Boundary Layers. *Annual Review of Fluid Mechanics*, 43:79–95, January 2011.

[25] J.D. Anderson Jr. *Modern Compressible Flow with Historical Perspective*, chapter 9.9, Historical Note: The 1935 Volta Conference. McGraw-Hill, New York, 3rd edition, 2003.

[26] W.E. Gray. The Effect of Wing Sweep on Laminar Flow. R.A.E. Tech. Memo. 255, 1952.

[27] N. Gregory, J.T. Stuart, and W.S. Walker. On the Stability of Three-Dimensional Boundary Layers with Application to the Flow Due to a Rotating Disk. *Philosophical Transactions of the Royal Society of London. Series A, Mathematical and Physical Sciences*, 248(943):155–199, July 1955.

[28] D.I.A. Poll. Some Observations of the Transition Process on the Windward Face of a Long Yawed Cylinder. *Journal of Fluid Mechanics*, 150:329–356, 1985.

[29] Y. Kohama. Some Expectation on the Mechanism of Cross-Flow Instability in a Swept Wing Flow. *Acta Mechanica*, 66:21–38, April 1987.

[30] B. Müller and H. Bippes. Experimental Study of Instability Modes in a Three-Dimensional Boundary Layer. *In AGARD Conf. on Fluid Dynamics of Three-Dimensional Turbulent Shear Flows and Transition*, pages 13.1–16.15, 1988. AGARD-R-438.

[31] P. Nitschke-Kowsky and H. Bippes. Instability and Transition of a Three-Dimensional Boundary Layer on a Swept Flat Plate. *Physics of Fluids*, 31:786–795, 1988.

[32] R.H. Radeztsky Jr., M.S. Reibert, and W.S. Saric. Effect of Isolated Micron-Sized Roughness on Transition in Swept-Wing Flows. *AIAA Journal*, 37(11):1370–1377, November 1999.

[33] H. Bippes and T. Lerche. Transition Prediction in Three-Dimensional Boundary-Layer Flows Unstable to Crossflow Instability. AIAA Paper 1997-1906, 1997.

[34] M.S. Reibert. *Nonlinear Stability, Saturation, and Transition in Crossflow-dominated Boundary Layers.* PhD thesis, Arizona State University, Tempe, AZ, August 1996.

[35] W. Koch, F.P. Bertolotti, A. Stolte, and S. Hein. Nonlinear Equilibrium Solutions in a Three-Dimensional Boundary Layer and Their Secondary Instability. *Journal of Fluid Mechanics*, 406:130–174, 1994.

[36] H. Bippes. Basic Experiments on Transition in Three-dimensional Boundary Layers Dominated by Crossflow Instability. *Progress in Aerospace Sciences*, 35(4):363–412, 1999.

[37] W.S. Saric, H.L. Reed, and E. White. Stability and Transition of Three-Dimensional Boundary Layers. *Annual Review of Fluid Mechanics*, 35:413–440, 2003.

[38] M. Choudhari, C.-L. Chang, C. Streett, and P. Balakumar. Integrated Transition Prediction: A Case Study in Supersonic Laminar Flow Control. AIAA Paper 2003-973, January 2003.

[39] F. Li and M.M. Choudhari. Spatially Developing Secondary Instabilities and Attachment Line Instability in Supersonic Boundary Layers. AIAA Paper 2008-590, January 2008.

[40] E.O. Swanson and S.P. Schneider. Boundary-Layer Transition on Cones at Angle of Attack in a Mach-6 Quiet Tunnel. AIAA Paper 2010-1062, January 2010.

[41] F. Li, M. Choudhari, C.-L. Chang, and J. White. Analysis of Instabilities in Non-Axisymmetric Hypersonic Boundary Layers over Cones. AIAA Paper 2010-4643, June 2010.

[42] E. Perez, H.L. Reed, and J.J. Kuehl. Instabilities on a Hypersonic Yawed Straight Cone. AIAA Paper 2013-2879, June 2013.

[43] B.C. Chynoweth, C.A.C. Ward, R.T. Greenwood, G.R. McKiernan, R.A. Fisher, and S.P. Schneider. Measuring Transition and Instabilities in a Mach 6 Hypersonic Quiet Wind Tunnel. AIAA Paper 2014-2643, June 2014.

[44] C.A.C. Ward, R.R. Greenwood, A.D. Abney, and S.P. Schneider. Transition and Instability Measurements in a Mach 6 Hypersonic Quiet Wind Tunnel. AIAA Paper 2013-2738, January 2013.

[45] C.A.C. Ward and R.O. Henderson. TSP Roughness Effects. Private Communication - Email, July 2014.

[46] C.A.C. Ward. *Crossflow Instability and Transition on a Circular Cone at Angle of Attack in a Mach-6 Quiet Tunnel.* PhD thesis, Purdue University School of Aeronautics & Astronautics, West Lafayette, Indiana, to be published December 2014.

[47] J. Poggie and R.L. Kimmel. Traveling Instability Waves in a Mach 8 Flow over an Elliptic Cone. *AIAA Journal*, 38(2):251–258, February 2000.

[48] T.J. Juliano. *Instability and Transition of the HIFiRE-5 in a Mach-6 Quiet Tunnel.* PhD thesis, Purdue University, West Lafayette, IN, August 2010.

[49] L.E. Steen. Characterization and Development of Nozzles for a Hypersonic Quiet Wind Tunnel. Master's thesis, Purdue University, West Lafayette, IN, December 2010.

[50] T.J. Juliano, E.O. Swanson, and S.P. Schneider. Transition Research and Improved Performance in the Boeing/AFOSR Mach-6 Quiet Tunnel. AIAA Paper 2007-535, January 2007.

[51] C.A.C. Ward. Hypersonic Crossflow Instability and Transition on a Circular Cone at Angle of Attack. Master's thesis, Purdue University School of Aeronautics & Astronautics, West Lafayette, IN, December 2010.

[52] M. Choudhari and C.A.C. Ward. Wavelength of Travelling Crossflow Waves on a 7-deg Cone at 6-deg AoA. Private Communication - Email, September 2012.

[53] B.M. Wheaton. Roughness-Induced Instability in a Laminar Boundary Layer at Mach 6. Master's thesis, Purdue University School of Aeronautics & Astronautics, West Lafayette, IN, December 2009.

[54] M.A. Rotea, L.A. Randall, G. Song, and S.P. Schneider. Model Identification of a Kulite Pressure Transducer. AIAA Paper 1996-2278, June 1996.

[55] S.J. Beresh, J.F. Henfling, R.W. Spillers, and B.O.M. Pruett. Pressure Power Spectra Beneath a Supersonic Turbulent Boundary Layer. AIAA Paper 2010-4274, July 2010.

[56] K. Fujii. Experiment of Two-Dimensional Roughness Effect on Hypersonic Boundary-Layer Transition. *Journal of Spacecraft and Rockets*, 43(4):731–738, July 2006.

[57] S.J. Rufer and D.C. Berridge. Experimental Study of Second-Mode Instabilities on a 7-Degree Cone at Mach 6. AIAA Paper 2011-3877, June 2011.

[58] S.J. Laurence, A. Wagner, K. Hannemann, V. Wartemann, H. Lüdeke, H. Tanno, and K. Itoh. Time-Resolved Visualization of Instability Waves in a Hypersonic Boundary Layer. *AIAA Journal*, 50(1):243–246, January 2012.

[59] T. Liu and J. Sullivan. *Pressure and Temperature Sensitive Paints.* Springer, 1st edition, 2005.

[60] M.P. Borg. *Laminar Instability and Transition on the X-51A.* PhD thesis, Purdue University School of Aeronautics & Astronautics, West Lafayette, Indiana, August 2009.

[61] J.P. Sullivan, S.P. Schneider, T. Liu, J. Rubal, C.A.C. Ward, J. Dussling, C. Rice, R. Foley, Z. Cai, B. Wang, and S. Woodiga. Quantitative Global Heat Transfer in a Mach-6 Quiet Tunnel. Technical Report 217331, NASA Langley Research Center, February 2012.

[62] K.M. Casper. Hypersonic Wind-Tunnel Measurements of Boundary-Layer Pressure Fluctuations. Master's thesis, Purdue University School of Aeronautics & Astronautics, West Lafayette, IN, July 2009.

[63] D.C. Berridge. Measurements of Second-Mode Instability Waves in Hypersonic Boundary Layers with a High-Frequency Pressure Transducer. Master's thesis, Purdue University School of Aeronautics & Astronautics, West Lafayette, IN, December 2010.

[64] D.C. Berridge. *Generating Low-Pressure Shock Waves for Calibrating High-Frequency Pressure Sensors.* PhD thesis, Purdue University School of Aeronautics & Astronautics, West Lafayette, Indiana, to be published February 2015.

[65] S.R. Pate. Dominance of Radiated Aerodynamic Noise on Boundary-Layer Transition in Supersonic/Hypersonic Wind Tunnels. Technical Report AEDC-TR-77-107, Arnold Engineering Development Center, March 1978.

APPENDICES

A. Symmetry Check

Second-mode amplitudes were computed from the PSDs of the pressure sensors for E3R3 around the azimuth at $x = 14.3$-in. The spectra was integrated over 200-350 kHz, where the disturbances were found. A percent difference was then computed from each signal's second-mode amplitude against the mean amplitude.

Table A.1 Percent difference of second-mode amplitudes against the mean amplitude computed at 0° AoA. $Re = 3.65{\times}10^6$/ft. All data from PCB sensors.

Ray [deg]	Amplitude [P'/P_{mean}]	Difference from Mean [%]
+90	.004	42.9
+60	.005	28.6
+30	.008	14.3
-30	.014	100.0
-60	.006	14.3
-90	.005	28.6

B. Roughness Measurements

Profilometer measurements were averaged from 10 profiles taken in random areas of each surface. The Torlon insert height was measured from the highest point near the lip of a dimple and the lowest point within the dimple.

Table B.1 Roughness measurements of cone surface and discrete roughness elements.

Entry [−]	Surface [−]	RMS [mil]	Height [mil]
All	aluminum	0.05	-
All	step from upstream edge of insert	-	0.30
All	step from downstream edge of insert	-	-0.15
2	TSP	0.05	-
3	TSP	0.07	-
4	TSP	0.05	-
4	E4 roughness strip/ring	2.04	-
5	TSP	0.05	-
5	E5-NP1	1.06	-
5	E5-NP2	1.96	-
6	TSP	0.10	-
6	Torlon insert	-	-4.94

C. Tunnel Conditions for All Runs

Conditions presented are the values where the data was processed. The sensor ray is the line of sensors on the same ray. Both Kulite Arrays are located on this line. The sensor ray is typically the center of the TSP images referenced from the windward ray at 0°.

Table C.1 Run Schedule for Entry 1.

Run [−]	P_o [psia]	T_o [°F]	T_w [°F]	Tunnel Noise [−]	AoA [deg]	Sensor Ray [deg]
1	81.6	299.2	71.8	Quiet	0	0
2	114.9	283.5	77.3	Quiet	0	0
3	117.4	301.3	83.3	Noisy	0	0
4	102.3	294.0	89.8	Quiet	0	0
5	138.1	302.6	72.1	Quiet	0	0
6	131.0	303.1	79.5	Noisy	0	0
7	155.8	297.7	85.7	Quiet	0	0
8	145.7	313.3	79.8	Noisy	0	0
9	117.7	308.4	89.4	Noisy	0	0
10	121.3	304.4	73.5	Quiet	2	90
11	117.6	301.9	84.2	Noisy	2	90
12	157.3	297.9	84.0	Quiet	2	90
13	144.5	299.8	88.7	Noisy	2	90
14	138.2	293.6	95.3	Quiet	2	90
15	131.1	298.3	96.2	Noisy	2	90
16	156.0	306.1	79.2	Quiet	2	180
17	146.4	305.6	86.2	Noisy	2	180
18	140.7	296.2	90.1	Quiet	2	180
19	133.7	299.0	82.5	Noisy	2	180
20	133.3	298.1	80.1	Noisy	2	180
21	121.8	291.1	80.5	Quiet	2	180
22	118.6	296.8	80.8	Noisy	2	180
23	158.9	293.5	94.7	Quiet	2	120
24	148.2	298.0	93.9	Noisy	2	120

Table C.2 Run Schedule for Entry 2.

Run [−]	P_o [psia]	T_o [°F]	T_w [°F]	Tunnel Noise [−]	AoA [deg]	Sensor Ray [deg]
1	122.1	308.5	58.6	Quiet	0	0
2	140.4	302.1	70.0	Quiet	0	0
3	157.3	300.5	72.1	Quiet	0	0
4	157.5	295.7	83.7	Quiet	2	0
5	140.1	291.7	90.4	Quiet	2	0
6	119.9	290.8	93.0	Quiet	2	0
7	123.5	306.1	89.3	Quiet	2	10
8	139.9	288.9	92.8	Quiet	2	10
9	155.2	288.4	94.1	Quiet	2	10
10	158.1	307.6	80.2	Quiet	2	30
11	140.3	300.0	86.6	Quiet	2	30
12	127.2	295.4	90.5	Quiet	2	30
13	121.0	294.9	84.6	Quiet	2	90
14	140.3	308.9	78.3	Quiet	2	90
15	158.0	301.9	85.1	Quiet	2	90
16	158.0	300.1	85.3	Quiet	2	180
17	139.6	295.1	91.3	Quiet	2	180
18	122.8	292.1	94.0	Quiet	2	180
19	121.5	289.5	92.5	Quiet	4	90
20	140.3	290.7	94.2	Quiet	4	90
21	157.6	288.7	96.6	Quiet	4	90
22	158.2	308.3	79.5	Quiet	4	120
23	141.3	300.2	85.7	Quiet	4	120
24	120.8	297.0	90.1	Quiet	4	120
25	157.2	297.2	89.4	Quiet	4	120

Table C.3 Run Schedule for Entry 2 continued.

Run [−]	P_o [psia]	T_o [°F]	T_w [°F]	Tunnel Noise [−]	AoA [deg]	Sensor Ray [deg]
26	156.9	294.0	91.7	Quiet	4	120
27	156.8	289.8	97.1	Quiet	4	120
28	158.2	289.1	92.2	Quiet	4	130

Table C.4 Run Schedule for Entry 3.

Run [−]	P_o [psia]	T_o [°F]	T_w [°F]	Tunnel Noise [−]	AoA [deg]	Sensor Ray [deg]
1	109.5	300.6	73.5	Quiet	0	0
2	137.6	295.5	79.5	Quiet	0	0
3	149.2	280.7	83.2	Quiet	0	0
4	157.4	279.2	91.8	Quiet	4	90
5	139.6	281.8	94.9	Quiet	4	90
6	119.3	301.4	77.7	Quiet	4	90
7	114.7	301.2	83.4	Noisy	4	90
8	83.1	294.9	82.4	Quiet	4	90
9	79.2	297.7	87.3	Noisy	4	90
10	83.2	297.1	91.1	Noisy	4	90
11	83.5	292.2	85.8	Quiet	4	105
12	79.0	295.1	89.1	Noisy	4	105
13	120.2	289.4	93.6	Quiet	4	105
14	139.2	289.3	94.0	Quiet	4	105
15	157.7	289.6	94.6	Quiet	4	105
16	156.1	302.6	78.2	Quiet	4	120
17	139.0	295.6	84.8	Quiet	4	120
18	120.1	291.8	89.1	Quiet	4	120
19	83.9	288.6	92.1	Quiet	4	120
20	79.1	293.1	93.5	Noisy	4	120

Table C.5 Run Schedule for Entry 4.

Run [−]	P_o [psia]	T_o [°F]	T_w [°F]	Tunnel Noise [−]	AoA [deg]	Sensor Ray [deg]
1	156.8	301.7	74.6	Quiet	4	90
2	139.9	297.7	82.3	Quiet	4	90
3	118.8	295.7	86.8	Quiet	4	90
4	83.6	303.5	82.7	Quiet	4	90
5	79.4	303.7	85.8	Noisy	4	90
6	83.8	294.4	89.9	Quiet	4	90
7	157.3	294.1	89.1	Quiet	4	90
8	83.8	289.6	92.1	Quiet	4	90
9	83.4	305.2	91.8	Quiet	4	90
10	83.9	306.0	75.5	Quiet	4	60
11	138.9	302.3	80.7	Quiet	4	60
12	157.6	300.4	82.6	Quiet	4	60
13	79.4	300.9	88.2	Noisy	4	60
14	121.1	295.2	86.7	Quiet	4	60
15	84.1	292.7	89.3	Quiet	4	60
16	157.6	291.8	88.3	Quiet	4	60
17	79.4	295.8	91.3	Noisy	4	60
18	157.5	305.4	75.5	Quiet	4	60
19	120.6	303.1	95.4	Quiet	4	60
20	79.6	303.7	86.5	Noisy	4	60
21	157.3	299.3	90.8	Quiet	4	60
22	139.1	300.2	74.7	Quiet	4	60
23	157.2	299.6	79.9	Quiet	4	90
24	157.3	304.8	75.7	Quiet	4	90
25	139.0	298.1	81.0	Quiet	4	90

Table C.6 Run Schedule for Entry 4 continued.

Run [−]	P_o [psia]	T_o [°F]	T_w [°F]	Tunnel Noise [−]	AoA [deg]	Sensor Ray [deg]
26	157.1	304.2	72.1	Quiet	4	90
27	139.1	301.3	77.3	Quiet	4	90
28	119.4	296.8	82.2	Quiet	4	90
29	157.1	302.1	76.8	Quiet	4	90

Table C.7 Run Schedule for Entry 5.

Run [–]	P_o [psia]	T_o [°F]	T_w [°F]	Tunnel Noise [–]	AoA [deg]	Sensor Ray [deg]
1	157.6	300.3	90.4	Quiet	4	90
2	139.7	300.3	90.6	Quiet	4	90
3	158.0	301.5	86.5	Quiet	4	120
4	158.2	301.2	87.9	Quiet	4	120
5	140.0	302.3	90.3	Quiet	4	120
6	158.0	299.4	95.8	Quiet	4	120
7	157.9	311.8	79.5	Quiet	4	120
8	139.4	303.7	87.2	Quiet	4	120
9	157.8	302.1	91.8	Quiet	4	120
10	150.5	315.5	93.0	Quiet	4	120
11	158.1	301.9	89.5	Quiet	4	90
12	139.7	297.8	94.1	Quiet	4	90
13	158.0	295.6	96.3	Quiet	4	90
14	139.6	294.1	97.6	Quiet	4	90
15	158.0	307.7	78.3	Quiet	4	90
16	139.5	302.5	86.7	Quiet	4	90
17	157.9	304.6	87.8	Quiet	4	90
18	139.5	298.2	92.2	Quiet	4	90
19	157.9	298.3	91.8	Quiet	4	120
20	139.7	298.3	93.1	Quiet	4	120
21	157.8	297.8	97.0	Quiet	4	120
22	150.5	310.5	98.7	Quiet	4	120
23	157.7	311.7	79.5	Quiet	4	120
24	139.6	304.8	87.3	Quiet	4	120
25	157.8	302.2	92.3	Quiet	4	120

Table C.8 Run Schedule for Entry 5 continued.

Run [−]	P_o [psia]	T_o [°F]	T_w [°F]	Tunnel Noise [−]	AoA [deg]	Sensor Ray [deg]
26	139.6	299.3	94.7	Quiet	4	120
27	157.9	314.3	78.9	Quiet	4	90
28	139.6	306.0	86.6	Quiet	4	90
29	158.0	302.3	90.6	Quiet	4	90
30	139.4	305.1	89.7	Quiet	4	90

Table C.9 Run Schedule for Entry 6.

Run [−]	P_o [psia]	T_o [°F]	T_w [°F]	Tunnel Noise [−]	AoA [deg]	Sensor Ray [deg]
1	150.4	277.8	77.5	Quiet	4	90
2	136.8	290.0	85.0	Quiet	4	90
3	149.6	286.9	82.4	Quiet	4	90
4	156.8	306.2	85.0	Quiet	4	120
5	138.7	301.7	90.9	Quiet	4	120
6	156.8	299.2	93.4	Quiet	4	120
7	170.8	316.9	86.4	Quiet	4	60
8	156.3	296.9	88.7	Quiet	4	60
9	155.4	303.4	84.2	Quiet	4	0
10	137.6	303.8	86.4	Quiet	4	0
11	155.8	299.9	89.2	Quiet	4	0
12	155.7	300.4	79.8	Quiet	2	90
13	157.2	300.8	86.5	Quiet	2	90
14	157.1	309.2	86.5	Quiet	2	90
15	156.9	304.9	92.1	Quiet	2	90
16	139.0	303.5	94.3	Quiet	2	90
17	156.8	309.3	90.3	Quiet	2	120
18	156.2	301.8	78.4	Quiet	2	120
19	138.6	301.3	85.2	Quiet	2	120
20	156.1	304.1	84.7	Quiet	2	60
21	153.4	306.1	82.0	Quiet	2	60
22	152.7	300.8	76.6	Quiet	2	0
23	135.8	298.4	84.9	Quiet	2	0
24	153.8	297.4	87.8	Quiet	2	0
25	157.1	304.8	76.0	Quiet	0	0

Table C.10 Run Schedule for Entry 6 continued.

Run [−]	P_o [psia]	T_o [°F]	T_w [°F]	Tunnel Noise [−]	AoA [deg]	Sensor Ray [deg]
26	139.2	304.1	82.8	Quiet	0	0
27	157.6	303.9	86.0	Quiet	0	0
28	157.5	305.1	87.1	Quiet	0	0
29	139.1	303.8	90.7	Quiet	0	0
30	157.4	300.7	92.2	Quiet	0	0
31	157.2	313.1	86.7	Quiet	3	90
32	139.1	306.5	92.0	Quiet	3	90
33	153.0	294.5	95.7	Quiet	3	90
34	158.5	310.2	82.4	Quiet	3	90
35	157.4	302.0	89.5	Quiet	3	90
36	157.2	301.2	94.5	Quiet	3	90
37	157.0	297.7	98.3	Quiet	3	90
38	142.1	299.3	99.3	Quiet	3	90
39	157.0	308.1	91.1	Quiet	3	120
40	139.1	304.2	94.9	Quiet	3	120
41	157.3	306.8	94.5	Quiet	3	120
42	157.3	315.0	82.9	Quiet	3	135
43	143.6	327.6	84.4	Quiet	3	135
44	157.4	312.3	89.8	Quiet	3	135
45	157.6	303.6	80.1	Quiet	3	60
46	157.3	300.3	88.3	Quiet	3	60
47	157.5	309.3	86.2	Quiet	3	0
48	139.2	304.1	87.5	Quiet	3	0
49	157.3	305.7	92.3	Quiet	3	0

D. Theoretical Heat Transfer Calculation

```
function [x,qw,St,Stanton_Param] = Theoretical_HT(Tref, p0, T0, Mach)

% Note:
% param1=ue^2/Hs
% param2=he/Hs
% beta=pressure gradient parameter
% Prw=Prandtl number at wall


% Test conditions for Run 6 at Purdue tunnel
T0_inf=T0; %  Freestream total temperature, K
p0_inf=p0*6894.757; % Freestream total pressure, Pa
Tw = Tref; % Wall temperature as measured with a thermocouple, K


% estimate the parameters
[ps,Ts,rhos,Ms,p_inf,T_inf,rho_inf]=...
    Taylor_Maccoll(T0_inf,p0_inf,Mach);

pe=ps;
Te=Ts;
rhoe=rhos;
Me=Ms;

gamma=1.4;
R=287; % J/kg-K

[mu k cp Pr rho]=air_properties(Te,pe);
```

```
% mu (microPa-sec), k (mW/m-K)
vis_e=mu*10^(-6); % kg/m-K
k_e=k/1000;       % W/m-K
cp_e=cp;          % J/kg-K

[mu k cp Pr rho]=air_properties(Tw,pe);
% mu (microPa-sec), k (mW/m-K)
vis_w=mu*10^(-6); % kg/m-K
k_w=k/1000;       % W/m-K
cp_w=cp;          % J/kg-K

[mu k cp Pr rho]=air_properties(T_inf,p_inf);
% mu (microPa-sec), k (mW/m-K)
vis_inf=mu*10^(-6); % kg/m-K
k_inf=k/1000;       % W/m-K
cp_inf=cp;          % J/kg-K

a=(gamma*R*Te)^0.5;
ue=a*Me;

haw=cp_e*Te+0.4*ue^2;
hw=cp_w*Tw;

a_inf=(gamma*R*T_inf)^0.5;
u_inf=a_inf*Mach;
Re_inf=rho_inf*u_inf*0.4/vis_inf;

rho_w=pe/(R*Tw);


Prw=cp_w*vis_w/k_w;
Hs=cp_e*Te+ue^2/2;
param1=ue^2/Hs;
param2=cp_e*Te/Hs;

```

```matlab
gw=cp_w*Tw/Hs;
beta=0;


f20g10=[0.33208*2^0.5;0.02]; % initial estimates
f2g1 = fminsearch('similarity_solution_fun',f20g10,[],...
    param1,param2,beta,gw,Prw,Tw,Hs,cp_w,ue);

f20=f2g1(1);
g10=f2g1(2);

x=[0.000:0.005:0.4]; % m
qw=Hs*(vis_w*rho_w*ue)^0.5*g10*x.^(-0.5)/(Prw*(2/3)^0.5);




Stanton_Param = 1/(rhoe*ue*(haw-hw));
St=qw*Stanton_Param;
```

```matlab
function [res]=similarity_solution_fun(x,...
    param1,param2,beta,gw,Prw,Tw,Hs,cp_w,ue)



% param1=ue^2/Hs
% param2=he/Hs
% beta=pressure gradient parameter
% Prw=Prandtl number at wall



f(1)=0;
f1(1)=0;
```

```
%f2(1)=0.33208*2^0.5;
f2(1)=x(1);

g(1)=gw;
%g1(1)=0.08;
g1(1)=x(2);
T(1)=Tw;
eta(1)=0;

h=0.002;
N=3000;

for n=1:N
    k0=h*f1(n);
    k1=h*(f1(n)+0.5*k0);
    k2=h*(f1(n)+0.5*k1);
    k3=h*(f1(n)+k2);
    f(n+1)=f(n)+(k0+2*k1+2*k2+k3)/6;

    m0=h*f2(n);
    m1=h*(f2(n)+0.5*m0);
    m2=h*(f2(n)+0.5*m1);
    m3=h*(f2(n)+m2);
    f1(n+1)=f1(n)+(m0+2*m1+2*m2+m3)/6;

    a0=h*g1(n);
    a1=h*(g1(n)+0.5*a0);
    a2=h*(g1(n)+0.5*a1);
    a3=h*(g1(n)+a2);
    g(n+1)=g(n)+(a0+2*a1+2*a2+a3)/6;

    n0=h*F(f(n),f1(n),f2(n),g(n),g1(n),...
        gw,param1,param2,beta,T(n),n);
    b0=h*G(f(n),f1(n),f2(n),g(n),g1(n),...
        gw,param1,param2,beta,Prw,T(n),n);
```

```
    n1=h*F(f(n)+0.5*k0,f1(n)+0.5*m0,...
        f2(n)+0.5*n0,g(n)+0.5*a0,g1(n)+0.5*b0,...
        gw,param1,param2,beta,T(n),n);
    b1=h*G(f(n)+0.5*k0,f1(n)+0.5*m0,...
        f2(n)+0.5*n0,g(n)+0.5*a0,g1(n)+0.5*b0,...
        gw,param1,param2,beta,Prw,T(n),n);
    n2=h*F(f(n)+0.5*k1,f1(n)+0.5*m1,...
        f2(n)+0.5*n1,g(n)+0.5*a1,g1(n)+0.5*b1,...
        gw,param1,param2,beta,T(n),n);
    b2=h*G(f(n)+0.5*k1,f1(n)+0.5*m1,...
        f2(n)+0.5*n1,g(n)+0.5*a1,g1(n)+0.5*b1,...
        gw,param1,param2,beta,Prw,T(n),n);
    n3=h*F(f(n)+k2,f1(n)+m2,f2(n)+n2,...
        g(n)+a2,g1(n)+b2,gw,param1,param2,beta,T(n),n);
    b3=h*G(f(n)+k2,f1(n)+m2,f2(n)+n2,...
        g(n)+a2,g1(n)+b2,gw,param1,param2,beta,Prw,T(n),n);
    f2(n+1)=f2(n)+(n0+2*n1+2*n2+n3)/6;
    g1(n+1)=g1(n)+(b0+2*b1+2*b2+b3)/6;

    T(n+1)=(Hs/cp_w)*(g(n+1)-0.5*(ue/Hs)*f1(n+1)^2);

    eta(n+1)=h*n;
end

res=abs(f1(N)-1)+abs(g(N)-1);
```